Diss. ETH No. 22973

LASER ABLATION COUPLED WITH ACCELERATOR MASS SPECTROMETRY FOR ONLINE RADIOCARBON ANALYSIS

A thesis submitted to attain the degree of

Doctor of Sciences of ETH Zurich

(Dr. sc. ETH Zurich)

presented by

CAROLINE WELTE

Dipl.-Phys. Ruprecht-Karls-Universität Heidelberg

born on 06.10.1983

citizen of the Federal Republic of Germany

accepted on the recommendation of

Prof. Dr. Detlef Günther, examiner

Prof. Dr. Hans-Arno Synal, co-examiner

Prof. Dr. Aeschbach, co-examiner

2015

Contents

Abstract

Carbonate records such as speleothems and corals are of great interest to paleoclimate research and related fields. Radiocarbon (^{14}C) in carbonate records is an important tracer, that provides insight into a vast variety of research areas such as carbon (C) soil dynamics from stalagmite records, bomb peak dating of young speleothems and reconstruction of water mass distributions in the ocean using corals. Either application requires access to the ^{14}C signature along the growth axis of the carbonate sample at high spatial resolution. A novel setup for online-^{14}C analysis was developed, combining the rapid sampling capabilities at high spatial resolution of Laser Ablation (LA) with the exceptional sensitivity of Accelerator Mass Spectrometry (AMS). LA is a powerful sampling technique that allows the removal of small quantities of material from a solid sample and subsequent online analysis. By focusing a UV laser onto carbonate samples, carbon dioxide (CO_2) is generated and can directly be introduced into the gas ion source of an AMS. The presented technique (LA-AMS) allows overcoming the time-consuming sampling and potentially contamination-prone chemical treatment required for conventional ^{14}C analysis of carbonate samples by AMS.

The efficiency of CO_2 conversion of three different laser ablation systems on carbonates was investigated using an inductively coupled plasma mass spectrometer (ICP-MS). An ArF excimer laser ($\lambda = 193\,nm$) showed a significantly higher conversion efficiency than two Nd:YAG lasers ($\lambda = 213\,nm$ and $266\,nm$). Based on these results, an ArF excimer laser was employed for the LA-AMS setup. An LA-cell consisting of two compartments - the cell head and the sample box - has been developed. This specific design leads to short measurement times and also reduces cross-contamination, while large samples of dimensions up to 150 x 25 x 15 mm^3 fit in the cell. Samples are moved relative to the laser beam by a positioning system at high spatial resolution. The effective volume of the cell head is approximately 0.6 mL resulting in a relatively short response time (time constant: 6 s) and the design aims for minimized particle deposition on the cell window and walls. The setup comprises a zoom lens and a camera for simultaneous observation of the sample and the ablation process and a designated software enabling different sampling strategies. Exchangeable inserts can be placed between the ablation region and the sample surface. The insert geometry influences the gas flow dynamics of the produced CO_2 into the ion source. Several inserts were tested and the optimum model combining a simple design with highest CO_2 transport rates was used for the subsequent experiments.
Significantly higher carrier gas flow rates on the order of 1.5 mL He/min in comparison to the commonly applied 0.1 mL He/min were necessary to reach optimum C mass flow

rates around 3 μg/min. Ion currents obtained for different sample materials were as high as 20 μA and the overall efficiency of the technique, i.e. the number of C ion reaching the detector compared to the ablated amount, was determined to be on the order of 5 ‰.
The initial characterization of this sampling technique has been carried out with pressed carbonate powder reference materials and marble. A low radiocarbon background of 0.011 ± 0.002 F^{14}C (fraction modern) was observed for ^{14}C-free marble, which allows to measure samples as old as 40,000 years. The ^{14}C content of different standard and reference materials were reproduced well within uncertainties of severl percent. Carry-over was studied using reference materials as well as a stalagmite sample with a growth stop of more than 300,000 years. The growth stop was used to test a deconvolution model simulating the mixing in and the washout from the LA-cell. Three scanning strategies that aim for differences with regard to analysis time, spatial resolution and measurement precision were investigated and compared. Depending on the measurement mode applied, a precision on the order of 1 - 5 % and a spatial resolution down to 100 μm can be obtained. Several centimeters of a sample can be scanned within one hour. The normalization procedure for analyzed samples was compared using conventional gas standards (OxII) and an LA-AMS standard (CSTD). Both standards yield comparable results, however, further studies are necesssary.
Prominent ^{14}C features such as the ^{14}C bomb imprint were resolved in two stalagmite samples and in a coral specimen. A stalagmite from a high alpine cave, where host rock dissolution occurs due to the oxidation of sulfides, was analyzed. Exceptional fluctuations in the ^{14}C signal were observed in this sample for the first time. Two pearl oyster sections showed modern ^{14}C levels, while a sample of the shell species Arctica islandica was found to have been alive at pre-bomb time. In a fish ear sample providing very little sample material on the order of 40 μg/min per subsample for analysis the ^{14}C bomb peak could be resolved.
LA-AMS allows acquiring highly spatially resolved radiocarbon records at a far higher rate than with any other method currently available.

Zusammenfassung

Karbonatische Klimaarchive, wie z.B. Stalagmiten und Korallen, sind für die Paläoklimaforschung von grosser Bedeutung. Das ^{14}C-Signal in Karbonaten ist Gegenstand zahlreicher Forschungsgebiete und liefert beispielsweise Erkenntnisse über die Bodendynamik von Kohlenstoff (C) anhand von Stalagmiten oder erlaubt Rückschlüsse über die Wassermassenverteilung in den Ozeanen mittels Korallen. Für diese Anwendung ist das Erfassen der Radiokohlenstoff (^{14}C) Signatur entlang der Wachstumsachse der Karbonatprobe mit hoher Ortsauflösung nötig, was normalerweise ein aufwendiger Prozess ist.
Im Rahmen dieser Arbeit wurde ein neuartiges Laserablationssystem für online ^{14}C - Messungen entwickelt (LA-AMS). Es vereint die kurzen Analysezeiten und die hohe Ortsauflösung von Laser Ablation (LA) mit der enormen Sensitivität von Beschleuniger-Massenspektrometerie (AMS). Mittels eines fokussierten und gepulsten Laserstrahls können kleinste Probenmengen von einem Festkörper abgetragen und analysiert werden. Dies ist ein zeitsparendes Probengewinnungsverfahren, wobei eine hohe Ortsauflösung erreicht werden kann. Bei dem Laserabtrag von Karbonaten entsteht ein hoher Anteil von CO_2. Dieses CO_2 kann direkt in die Gasionenquelle eines AMS geleitet werden, um eine ^{14}C - Analyse durchzuführen. Der für die konventionelle ^{14}C Messung nötige, zeitintensive und kontaminationsanfällige Zwischenschritt der Graphitisierung, entfällt dabei.

Die CO_2-Umwandlungseffizienz von drei LA-Systemen auf Karbonatproben wurde mittels Massenspektrometrie mit induktiv gekoppeltem Plasma (ICP-MS) bestimmt. Dabei zeigte ein ArF Excimer Laser ($\lambda = 193\,\text{nm}$) eine signifikant höhere Umwandlungseffizienz, als zwei Nd:YAG Laser ($\lambda = 213\,\text{nm}$ und $266\,\text{nm}$). Auf diesen Ergebnissen basierend, wurde ein ArF Excimer Laser (Ex5) für das LA-AMS System ausgewählt. Eine Ablationszelle bestehend aus zwei Kammern - dem Zellkopf und der Probenkammer - wurde entwickelt. Dieses Design ermöglicht kurze Analysezeiten, wobei Proben bis zu einer Grösse von 150 x 25 x 15 mm^3 in der Ablationszelle platziert werden können. Mittels Schrittmotoren mit hoher örtlicher Auflösung wird die Probe relativ zu dem Laserstrahl bewegt. Das effektive Ablationsvolumen im Zellkopf beträgt nur 0.6 mL und erlaubt somit eine vergleichsweise kurze Auswaschzeit (Zeitkonstante: 6 s). Durch das Design wird die Ablagerung von Partikeln auf dem Fenster und den Zellwänden minimiert. Eine speziell entwickelte Software ermöglicht verschiedene Probenahmestrategien und eine Kamera mit Zoomobjektiv erlaubt die Beobachtung der Probe simultan zum Ablationsprozess. Austauschbare Einsätze werden zwischen dem Zellkopf und der Probe platziert. Das Design des Einsatzes beeinflusst die Transportrate des laser-produzierten CO_2 in die Ionenquelle. Verschiedene Einsätze wurden entwickelt und ein Einsatz mit hoher CO_2 Transporteffizienz und vergleichsweise

einfacher Geometrie wurde für die nachfolgenden Experimente verwendet.
Für alle getesteten Probenmaterialien wurden vergleichbare Ionenströme von bis zu 20 μA bei einem C-Massenfluss von 3μg/min erzielt, was mit Signalintensitäten von konventionellen Gasmessungen vergleichbar ist. Allerdings waren hierfür deutlich höhere Trägergas Flussraten von etwa 1.5 mL He/min, im Vergleich zu den normalerweise verwendeten 0.1 mL He/min, nötig. Die Gesamteffizienz des Systems, also die Anzahl der C Ionen, die den Detektor erreichen, verglichen mit der ablatierten Menge, liegt bei 5 ‰.
Eine genaue Charakterisierung des LA-AMS Aufbaus war zentraler Bestandteil der Arbeit und wurde an Marmor und Referenzmaterialien aus gepresstem Karbonatpulver durchgeführt. Das ^{14}C-freie Marmor wurde als Blindprobe verwendet und ergab ein F^{14}C (fraction modern) von 0.011 $\pm$ 0.002. Dies erlaubt die Analyse von Proben die älter als 35'000 Jahre sind. Der ^{14}C-Gehalt verschiedener Referenz- und Standardmaterialien konnte innerhalb der Unsicherheiten reproduziert werden. Verschleppungseffekte wurden anhand von Referenzmaterialien und mittels eines Stalagmiten, der einen Wachstumsstop (Hiatus) von mehr als 300'000 Jahren aufweist, untersucht. Anhand des Hiatus wurde die Gasmischung in und das Auswaschen aus der Zelle modelliert. Drei Beprobungsstrategien wurden entwickelt und ermöglichen es die Analysezeit, Ortsauflösung und Messpräzision an die jeweilige Anwendung anzupassen. Ein schneller Überblick über das ^{14}C Signal in einer Probe kann durch das abrastern mehrerer Zentimeter innerhalb einer Stunde erfasst werden. Je nach Modus wird dabei eine Präzision zwischen 1 % und 5 % und eine Ortsauflösung von bis zu 100 μm erreicht. Das für die Auswertung der Daten nötige Normalisierungsverfahren wurde mit konventionellen Gasstandard (OxII) und einem speziellen LA-AMS Standard (CSTD) durchgeführt. Beide Standards lieferten vergleichbare Resultate, aber weitere Studien diesbezüglich sind nötig.
Markante ^{14}C Signaturen, wie z.B. die ^{14}C-Anomalie in den 1950er und 1960er Jahren verursacht durch die Kernwaffentests, konnten in zwei Stalagmiten und in einer Koralle mittels LA-AMS reproduziert werden. Ein Stalagmit aus einer hochalpinen Höhle, in der die Karbonatlösung aufgrund von der Oxidation von Sulfiden stattfindet, wurde analysiert. Dabei wurden ugewöhnlich schnelle und sehr stark ausgeprägte Schwankungen in dem ^{14}C Signal gefunden. Zwei Teilstücke einer Schwarzlippigen Perlenauster wiesen einen modernen ^{14}C Gehalt auf, wohingegen bei einer Muschel der Art Arctica islandica nachgewiesen werden konnte, dass diese vor den Nuklearwaffentests gelebt hatte. In einer Otolith Probe mit sehr wenig Material pro Teilprobe ($\sim$40 μg) wurde die ^{14}C Bomben Anomalie aufgelöst werden.
LA-AMS ermöglicht es somit ^{14}C-Datensätze mit hoher Ortsauflösung deutlich schneller als mit jeder anderen derzeit verfügbaren Methode zu erfassen.

1 Introduction

Since its first employment by J. R. Arnold and W. F. Libby in 1949 (Libby et al., 1949), radiocarbon (^{14}C) dating has emerged and today is applied in a great variety of areas. The most popular examples can be found in archeology, e.g. the Santorini eruption (Friedrich et al., 2006) and the 'ice man' Ötzi (Bonani et al., 1994), but also in disciplines such as oceanography and paleoclimatology, ^{14}Cplays an important role: it is used to track changes in ocean circulation and carbon cycles (Robinson et al., 2005; Druffel et al., 2007) or to gain insights into carbon soil cycling (Trumbore, 2009; Rudzka-Phillips et al., 2013). Another field of application is the reconstruction of past solar activity (Bard et al., 2000; Beer et al., 2002; Usoskin et al., 2009). Recently, ^{14}Cwas used in biomedical applications, for instance by Schulze-König et al. (2010b), who investigated ethanol oxidation in humans.

1.1 Radiocarbon

Carbon has three naturally occurring isotopes: ^{12}C and ^{13}C are stable, whereas ^{14}C is radioactive, with a half life of 5700 +/- 30 yrs (Kutschera, 2013). However, the previously found, so called Libby half-life of 5568 $\pm$ 30 yrs (Libby, 1952) has been used until today to prevent confusion of ^{14}Cages calculated with different half-lives (Olsson, 1968). ^{14}C is a beta emitter and decays to ^{14}N, an electron and an electron-antineutrino. In the earth's atmosphere ^{14}Cis produced by nuclear interactions of secondary cosmic ray particles with atoms (Figure 1.1). The cosmic radiation consists of a solar component - which contributes the largest number of particles reaching the earth's atmosphere - and of an extra solar component - which includes the particles with the highest energies (1-10 GeV) (Finkel and Suter, 1993). This extra solar component, which originates most likely from super novae explosions, forms a cascade of secondary particles (Masarik and Beer, 1999), among them neutrons that subsequently produce ^{14}C mainly through reactions between neutrons and nitrogen (^{14}N), according to:

$$^{14}N + n \rightarrow ^{14}C + p \tag{1.1}$$

(Libby, 1946; Lal and Peters, 1967), where n denotes neutrons and p protons. The ^{14}C production has a latitudinal dependence, as the earth's magnetic field shields the cosmic ray particles most effectively at the equator and less toward the polar regions. Therefore, cosmogenic nuclide production is highest at the poles and lowest at the equator. The strength of the geomagnetic field varies over time, which leads to a time dependent

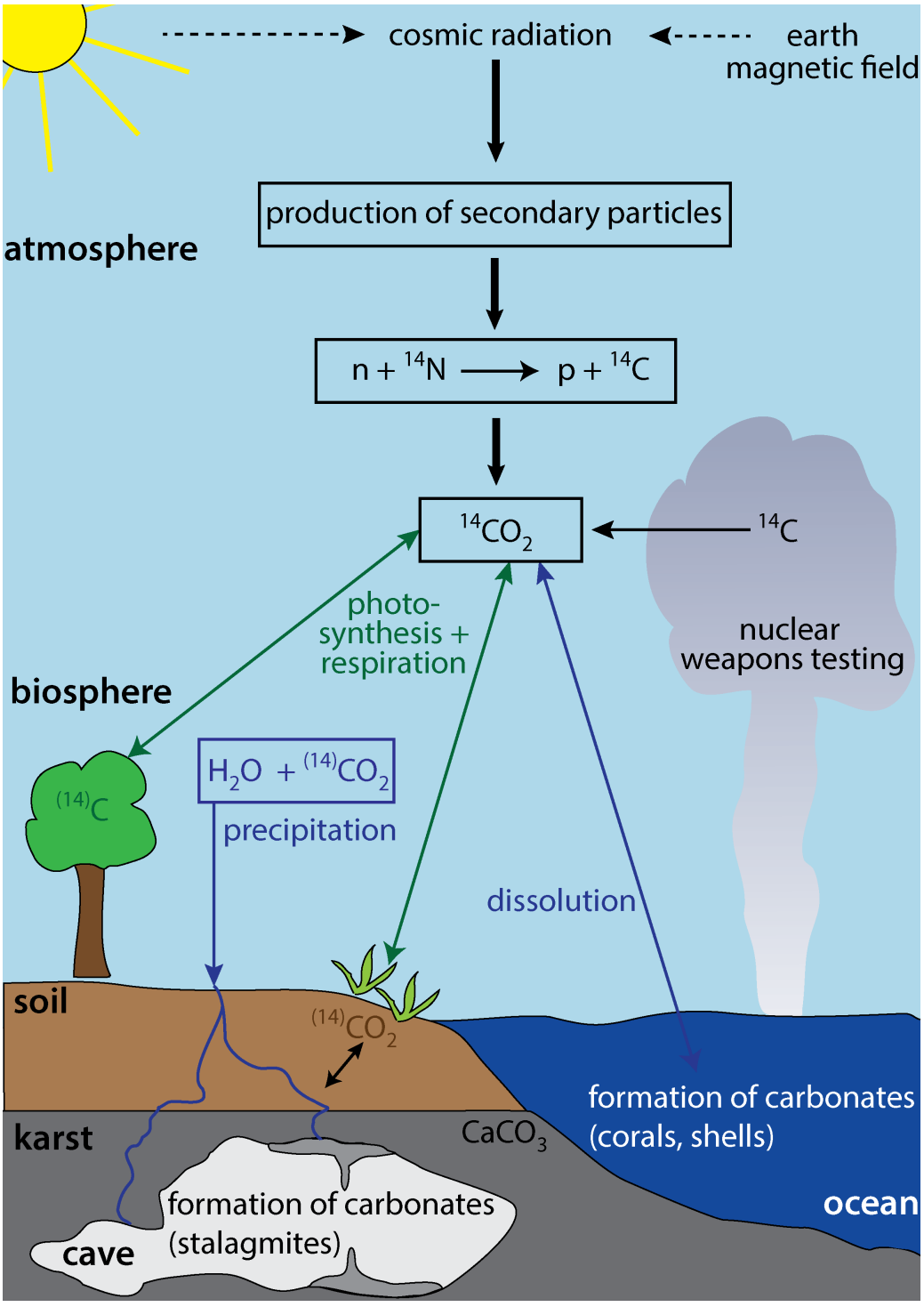

Figure 1.1: Simplified scheme of ^{14}C in the carbon cycle. ^{14}C is produced in the atmosphere by collisions of cosmic ray produced neutrons with residual N atoms and quickly forms CO_2. The CO_2 enters the biosphere via photosynthesis and the ocean by dissolution.

production rate with variations at time scales in the order of millennia. Furthermore, the production depends at a much shorter time-scale (decadal to centennial) on the solar activity: if the sun is in an active phase, a strong solar wind is generated and fewer cosmic ray particles reach the earth, which reduces the production of radio nuclides (Bard, 1998). The latest estimation of the global average production rate for cosmogenic ^{14}C yields 20500 atoms $m^{-2}s^{-1}$ (Masarik and Beer, 2009). After its production, the ^{14}C is eventually transformed into $^{14}CO_2$ in the atmosphere (Pandow et al., 1960; Crutzen, 1997), where it is well mixed and becomes part of the global carbon cycle, by entering different carbon reservoirs, i.e. the biosphere, geosphere and hydrosphere. In the biosphere the $^{14}CO_2$ is taken up by plants from the atmosphere by photosynthesis and is then transferred to plant-eating animals and to humans (Craig, 1957; Oeschger et al., 1975). As soon as an organism dies, its ^{14}C uptake stops, and the ^{14}C clock begins to run. The number of ^{14}C declines according to the radioactive decay law:

$$N(t) = N_0 e^{-\lambda \cdot t} \tag{1.2}$$

with N_0 = initial number of ^{14}C atoms, N(t) = number of ^{14}C atoms at t, $\lambda = \ln 2/T_{1/2}$ decay constant and the half life $T_{1/2}$. ^{14}C dating can be applied to samples as old as 45 000 - 50 000 years.

In the 1950s and 1960s worldwide nuclear weapons testing resulted in a large flux of thermal neutrons that reacted with ^{14}N of the atmosphere to form ^{14}C. The result was a doubling of the $^{14}C/^{12}C$ compared to pre-bomb levels reaching a maximum in 1963 (referred to as the 'bomb spike', 'bomb pulse' or 'bomb peak'), which is shown in Figure 1.2. The ^{14}C levels have decreased since then due to mixing with large carbon reservoirs such as the ocean and the biosphere. This anthropogenic ^{14}C signal has proven to be a useful tracer for studying the carbon cycle (Richter et al., 1999; Levin and Hesshaimer, 2000; McNichol and Aluwihare, 2007). The bomb peak has been applied to many other research fields including forensic studies (Zoppi et al., 2004; Alkass et al., 2010; Buchholz and Spalding, 2010) and paleo-climate research (Fohlmeister et al., 2012; Rudzka-Phillips et al., 2013; Sundqvist et al., 2013).

1.2 ^{14}C in carbonates

Natural carbonates are formed either by living organisms such as corals, foraminifera and shells, or by precipitation from a super-saturated solution, like speleothems. The isotopic C signature of the surrounding reservoir is saved within the growth layers of the carbonate record. This signature is not reflecting the atmospheric ratio, as the carbon undergoes fractionation processes prior to its incorporation into the carbonate. Direct ^{14}C dating therefore has so far only played a minor role (Broecker et al., 1960), because the carbonates

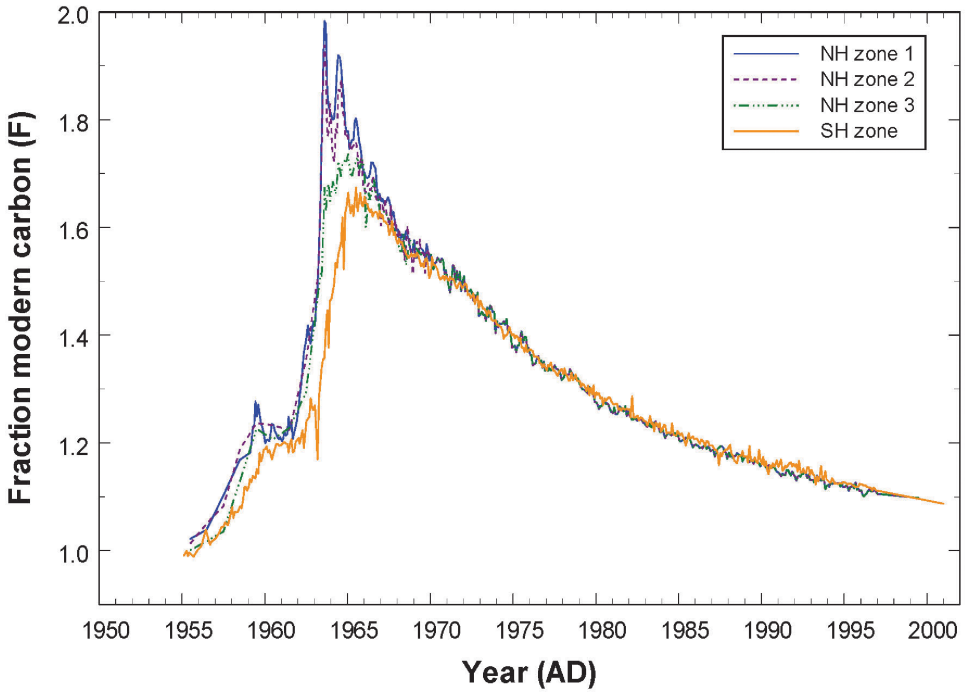

Figure 1.2: Atmospheric ^{14}C content caused by nucelar weapon tests during the 1950s and 1960s ((Hua and Barbetti, 2004)). The concentration in the Northern Hemisphere (NH) was almost doubled.

have an apparent ^{14}C age that can differ substantially from the true age, i.e. the year in which the carbonate was formed.

(i) **Corals**
Marine biogenic carbonates reflect a ^{14}C-signature that depends on the mixing history of the water mass the organism lives in. The spatial distribution of corals is not limited to shallow and warm tropical waters, but they can also be found at all latitudes and depths of the ocean. Deep-sea corals are widespread in all major ocean basins and can be found at depth of more than 6000 m (Freiwald, 2002). Their growth rates lie between less than 0.1 and up to 5 mm/yr (Adkins et al., 2004), and they can live up to thousands of years (Roark et al., 2009). In the marine environment of a coral, the reservoir age at a certain water depth is related to the ventilation age of the prevailing water mass. Their importance to research lies in the fact that not only the isotopic composition of the surrounding seawater is incorporated into the coral's skeleton during its growth, but in addition the aragonite skeleton can be accurately dated via U/Th-disequilibrium dating (Adkins et al., 1998). Therefore, from the combined U/Th-age and ^{14}C-age in deep-sea corals, the water mass ventilation age at the time of the coral growth can be determined (Adkins et al., 1998; Mangini et al., 1998). Only few studies (Schröder-Ritzrau et al., 2003; Frank et al., 2004; Burke et al., 2010) present U/Th- and ^{14}C-data from deep water corals, providing

new insights into the relationship between oceanic circulation changes and climatic fluctuations. The reason for this is that the sample preparation for both measurement techniques is rather time consuming and costly.

(ii) **Terrestrial carbonates**
Terrestrial inorganic carbonates, e.g. speleothems, are formed in limestone caves. As rainwater seeps through the soil, it takes up CO_2 which is produced by plant roots and microbial decomposition of organic matter. The additional CO_2 acidifies the water and causes limestone dissolution as the water travels through the karst. Because the CO_2 partial pressure in the cave is much lower than in the water, the carbon dioxide degasses from the drip water causing the deposition of $CaCO_3$ in the cave. Since speleothems grow continuously over thousands of years in sheltered cave environments, they are regarded as valuable climate archives. They provide exceptionally accurate U/Th-chronologies (Richards and Dorale, 2003; Henderson, 2006; Scholz and Hoffmann, 2008) and contain a large number of proxies, e.g. their stable carbon and oxygen isotope signal as well as various trace elements as magnesium or strontium (Fairchild and Treble, 2009). Speleothems can be found in most parts of the world, which allows the investigation of spatial variability of climate changes. Typical growth rates vary by two orders of magnitude, ranging from below 0.01 mm/yr up to more than 1 mm/yr. Growth rates are mainly influenced by temperature and the Ca-ion concentration in the drip water (Fleitmann et al., 2003; Genty et al., 2003). Trace element- and isotope-analyses in stalagmites have been investigated previously by Laser Ablation - Inductively Coupled Plasma Mass Spectrometry (LA-ICPMS) (McDermott et al., 2001; Baldini et al., 2008; Fricker et al., 2011). High spatial resolution analyses of stable isotopes of approximately 0.3 mm by micro-milling have also been conducted (Spötl and Mattey, 2006). The combination of U/Th-ages and ^{14}C has been applied to speleothems, e.g. by Genty and Massault (1999); Beck et al. (2001). Nevertheless, as in the case of marine carbonates, further studies have been hampered by the elaborate and expensive measurement techniques.
A combination of Th/U dating with ^{14}C-measurements at highest possible spatial resolution provided by a laser ablation or micro milling has not been presented yet.

1.3 ^{14}C-measurement techniques

Traditionally, ^{14}C measurements were performed by decay counting, until accelerator mass spectrometry (AMS), which allows the direct counting of ^{14}C-atoms, emerged in 1977. Even though detection rates in decay counting are much lower than for AMS, it is still used today, if sufficiently large sample sizes are available. The advantages of decay counting techniques are a simpler and less costly setup (Finkel and Suter, 1993). Recently, a new spectroscopic measurement technique for ^{14}C (Saturated-absorption cavity ring-down

spectroscopy) has been introduced, which is not ready, yet, for routine operation.

1.3.1 Decay counting

The first ^{14}C measurements were conducted via decay counting, allowing to determine the activity of a sample instead of directly measuring the number of ^{14}C-atoms. Libby (1955) used a Geiger-Müller detector for solid samples, but he faced the problem of a relatively large background caused by natural radioactivity and cosmic rays. Even though Libby was able to reduce the background significantly, a real improvement of the sensitivity was only made when proportional counters with gaseous samples were used instead of Geiger-Müller detectors (Brannon et al., 1955; Fergusson, 1955; Olsson, 1957; Broecker et al., 1959; Oeschger, 1963; Suess, 1965; Tans et al., 1982). Another technique also developed in the 1950s is measuring the ^{14}C-decay by liquid scintillation counters (Reynolds et al., 1950; Arnold, 1954). The stability and sensitivity of this method is comparable to proportional gas counters. Nevertheless, both techniques require relatively large samples in the gram-range of carbon and long measurement times. The ^{14}C measurement techniques listed above are reviewed in detail in Povinec et al. (2009).

1.3.2 Accelerator mass spectrometry

The idea of directly counting the number of ^{14}C-atoms in a sample emerged simultaneously with the development of the ^{14}C method in the 1950s. The mass spectrometric analysis of ^{14}C was hindered by its interfering isobar ^{14}N as well as by molecular background caused by ^{13}CH and $^{12}CH_2$ that exceed the abundance of ^{14}C by several orders of magnitude. Purser et al. (1977) and Nelson et al. (1977) introduced the first AMS-systems in the 1970s and the subsequent AMS facilities were set up in nuclear physics laboratories with cyclotrons (Muller, 1977) and high voltage tandem accelerators (Bennett et al., 1977; Nelson et al., 1977; Purser et al., 1977). Cyclotrons allowed mass analysis by producing positive ions of high charge state, which lead to molecule dissociation. Isobars were separated from the rare nuclide in the detector, because the energy loss depends on the atomic number. Tandem accelerators made use of the development of the Cs sputter ion source (Chapman, 1972), where negative C ions are formed but the formation of negative ^{14}N-ions is suppressed (Purser et al., 1977). The interfering molecules are destroyed in the acceleration unit, where high charge states are yielded by the stripping process. Tandem accelerators showed to be more suitable for the detection of ^{14}C and other radionuclides than cyclotrons and soon dedicated AMS facilities with terminal voltages of several MV were installed. Standard AMS machines focus on the detection of ^{14}C, but often are also employed for the analysis of other radionuclides, such as ^{10}Be, ^{26}Al and ^{129}I (Raisbeck et al., 1983, 1984; Elmore and Phillips, 1987; Vockenhuber et al., 2003; Steier et al., 2004; Kutschera, 2005). An important but unintentional step toward smaller AMS facilities was

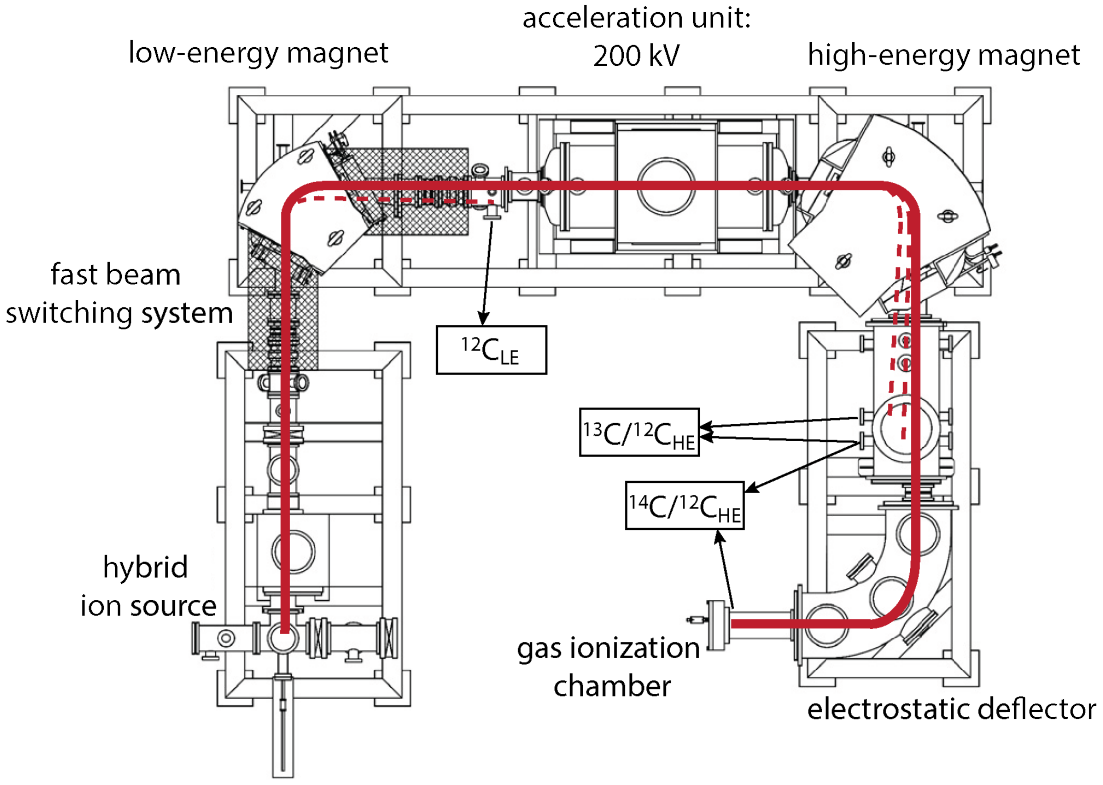

Figure 1.3: Layout of the MICADAS system (adapted from Synal et al. (2007)).

achieved by Lee et al. (1984), who studied the fundamental processes of the molecular background on ^{14}C, showing that the $^{12}CH_2^{2+}$ molecule could be effectively eliminated. More than ten years later (Suter et al., 1997) used terminal voltages of less than 1 MV at the PSI/ETH AMS facilty in Zürich in 1997 and showed that this was sufficient for the destruction of molecules in the 1^+ and 2^+ charge state by multiple ion collisions. The foundation for AMS systems operating at terminal voltages of less than 0.5 MV was laid. The Tandy-AMS (Jacob, 2001; Stocker et al., 2005; Mueller et al., 2008; Lachner et al., 2013; Christl et al., 2013) working at 0.5 MV is still in use at the Laboratory of Ion Physics (LIP) at ETH Zurich and is mainly employed for the measurement of actinides, ^{129}I and ^{10}Be. The next step toward table-top AMS was also reached at the LIP by introducing the MIniCArbonDAtingSystem (MICADAS) (Synal et al., 2007; Wacker et al., 2010), which is a table-top AMS with a footprint of 2.5 x 3 m^2 operating at a terminal voltage of 200 kV (Synal et al., 2004). The latest development is the myCADAS (Synal et al., 2013), an AMS-facility that operates without an acceleration unit.

MICADAS AMS system

The general working principle of AMS system will be explained in the following section on the basis of the MICADAS, which is exclusively used for the measurement of ^{14}C. AMS is not an absolute method, but yields the ratio of the rare to the abundant isotope and the method is based on connecting a series of filters in order to suppress interfering molecules and isobars of the rare isotope. In the case of the MICADAS system (Figure 1.3) these filters are the ion source, the accelerator unit, the sector field magnets, the electro-static analyzer (ESA) and the detector. The ESA and magnets make use of the fact, that particles of charge q moving at a velocity $\vec{v}$ in the presence of a magnetic ($\vec{B}$) or electric ($\vec{\mathcal{E}}$) field experience the Lorentz force guiding them according to the following equation of motion:

$$m \cdot \vec{a} = q\ [\vec{\mathcal{E}} + (\vec{v} \times \vec{B})] \tag{1.3}$$

where m denotes the mass of the particle and $\vec{a}$ its acceleration. The filters of an AMS will be discussed in the following section in the order that the ions pass through them in the MICADAS:

(i) **Cs sputter source:**
The negative ion formation of the isobar ^{14}N is suppressed. Therefore, the negative ion source can be used as a first filter of an AMS instrument. The MICADAS is equipped with a hybrid ion source that can accept graphite as well as gaseous CO_2 samples. The ion source is at a potential of -30 kV with an additional sample potential of -10 kV and several lenses for focusing purposes, as shown in Figure 1.4 a. In the Cs reservoir, elemental Cs is heated and transferred through a tube to the ionizer. Here the Cs atoms are thermally ionized, and the Cs^+ ions are accelerated and focused through the immersion lens onto the target (cathode) where the negative ion formation of the C, referred to as Cs sputtering, takes place. Cs is used because high ionization yields were found (Ishikawa, 2004). The C^--ions are focused and extracted by the extraction lens reaching an energy of 40 keV. The negative ion yield with this setup is on the order of 20 %.

Gas ion source
In comparison to graphite analysis, smaller sample sizes are necessary and the chemical preparation is shorter. First attempts to introduce CO_2-gas into the ion source of an AMS were done by Middleton (1978) as well as Heinemeier and Andersen (1983). Bronk Ramsey and Hedges (1997) demonstrated the potential of a hybrid ion source, which allows to make use of the advantages of both techniques. Further developments have led to the ability of direct and precise $^{14}C/^{12}C$ measurements of CO_2 with a gas ion source at the LIP, Zurich (Ruff et al., 2007; Ruff, 2008; Ruff et al., 2010a; Fahrni et al., 2013). The shape and material of the cathode (sputter target) is of great importance for the efficiency of the sputtering process. In the

case of gas ion source AMS it consists of a titanium insert and an aluminum cap (Figure 1.4 b and c). The CO_2 enters the aluminum cap through an orifice on the side and is transferred along the titanium insert to the upper part of the cathode, where a second hole in the aluminum cap is placed. The titanium binds the CO_2 very efficiently keeping it in position for the sputtering process. Further information on the optimized gas ion source as well as on different target materials can be found in Fahrni et al. (2013).

(ii) **Low energy mass spectrometer:**
The ions leave the ion source and subsequently enter the low energy (LE) magnet where they experience a magnetic field that acts as a pure mass filter because they have the same energy given by the product of their charge (-1) and the potential of the ion source (-40 kV):

$$m \cdot \vec{a} = q\ (\vec{v} \times \vec{B}) \tag{1.4}$$

Using the expression for the centrifugal force the following expression for the radius r_B of the ions passing through the magnet can be derived:

$$r_B \cdot B = \frac{mv}{q} = \frac{p}{q} \tag{1.5}$$

where p denotes the momentum of the particle. After the magnet, a Faraday cup is positioned in the focal plane of the LE magnet with an offset to the primary trajectory of the mass 14 ions to measure the ^{12}C-current on the low energy side. In combination with the current measured in a second Faraday cup after the accelerator, the transmission through the accelerator is monitored. The low energy spectrometer is equipped with a fast beam pulsing system allowing the different carbon isotopes to enter the accelerator in short pulses of the following pattern: 50 μs for ^{12}C, 40 ms for ^{14}C, 500 μs for ^{13}C, 40 ms for ^{14}C and so on.

(iii) **Acceleration unit:**
The accelerator unit, at a potential of 200 kV and equipped with a gas-stripper, forms the next filter. The ions are accelerated toward the vacuum insulated high voltage platform were they enter a gas stripper filled with N_2. Multiple ion collisions (i) lead to molecule dissociation and (ii) cause that (C^-) ions change their charge state from negative to positive. The charge state with the highest negative ion yield is selected, in the case of C this is for the 1^+ charge state, and the now positively charged ions traverse the same potential and enter the high energy spectrometer where ^{14}C-ions.

(iv) **High energy mass spectrometer:**
The stripping process results in an energy spread of the ions and, in addition, fragments from broken-up molecules contribute to the beam. Therefore, a two-filter systems is used on the high energy side consisting of a magnet and an electrostatic

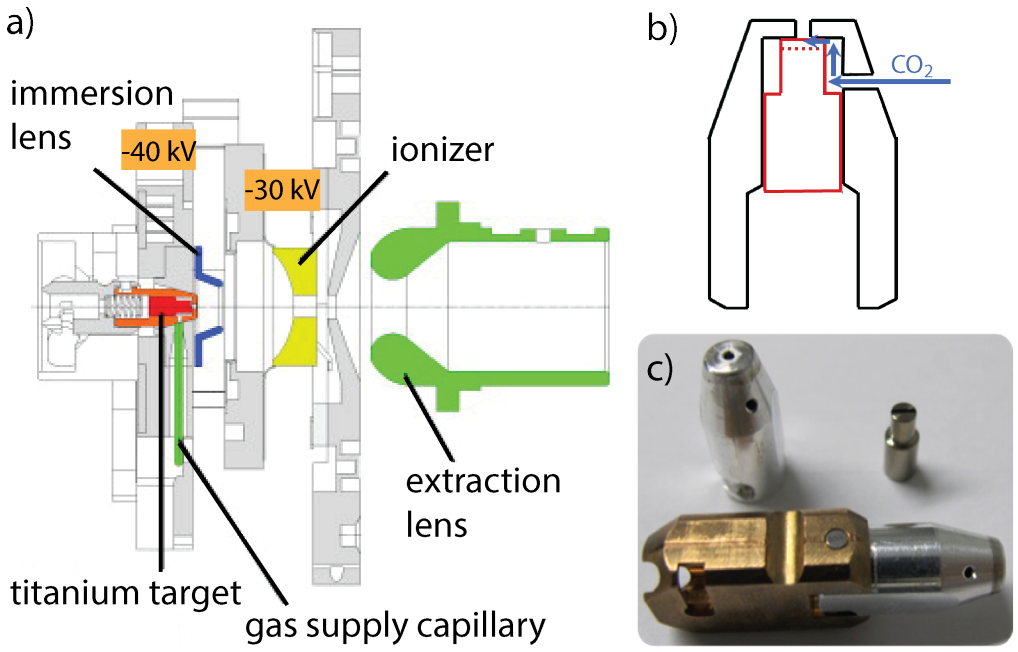

Figure 1.4: (a) Overview of the gas ion source of the MICADAS. (b) Schematic of the cathode consisting of the titanium inlet (red) and the aluminum cap (black). Also shown is the flow of CO_2 through the orifice on the side of the aluminum cap to the top of the cathode. (c) Picture of the aluminum cap, titanium inlet and complete target.

analyzer (ESA) that act together as an achromatic m/q filter. The 90° magnet acts as a p/q filter. In the case of the MICADAS, the 1^+ charge state is selected. After the magnet, two Faraday cups for the detection of the ^{13}C- and ^{12}C-current are placed. Another Faraday cup is installed to detect ^{13}C ions that result from broken up $^{13}CH^-$ molecules and can be used for background corrections. The 90° ESA is located after the HE-magnet and is used to focus ions of equal energy. It consists of two curved and parallel plates of equal and opposite potential that create a homogeneous radial electric field between the plates. Equation 1.3 can be rewritten:

$$m \cdot \vec{a} = q\vec{\mathcal{E}} \tag{1.6}$$

Denoting the distance between the plates with d and the potential difference with ΔV and inserting the centripetal force, yields the following equation:

$$\frac{mv^2}{r_E} = q\vec{\mathcal{E}} \quad \Leftrightarrow \quad r_E = \frac{2Ed}{q\Delta V} \tag{1.7}$$

where ε denotes the energy of the ions.

(v) **Gas ionization chamber:**
The last filter of an AMS is the detector (Suter et al., 2007), in the case of the MICADAS a gas ionization chamber filled with isobutane to a pressure of 20 mbar for the detection of the ^{14}C ions (Mueller et al., 2015). Isobutane has the advantage of a high ionization efficiency, i.e. fairly low energies are necessary to create an electron-ion pair and it furthermore has a high stopping power.

1.3.3 Saturated-absorption cavity ring-down spectroscopy

The latest development in ^{14}C measurements techniques was achieved by Galli et al. (2011), who measured ^{14}C-concentrations far below the natural abundance at a $^{14}C/^{12}C$ of 4.3×10^{-14} using saturated-absorption cavity ring-down spectroscopy (SCAR). The advantages of this table-top setup are compactness and low cost. Furthermore, the samples are not consumed during measurement. Measurement precisions on the order of 3 - 4 % were reached with measurement times of 1 hour, while conventional AMS-measurement techniques allow to achieve precision of less than 0.5 %. The required sample size is on the order of 50 mg, which is 50 times higher than for measurements by AMS and the background level is more than 4 times higher. Due to these drawbacks, the optical ^{14}C detection by SCAR is at this stage a promising technique mainly for applications where high precision is not required, such as in the biomedical field (Synal and Wacker, 2010).

1.4 ^{14}C data-evaluation

^{14}C-analysis requires the measurement of a standard and a blank (^{14}C-free) besides the sample itself (compare Figure 1.5). Normally, also a reference material is measured to ensure a sufficient quality of the measurement. At the MICADAS system, the data evaluation is automatically done using the BATS-software (Wacker et al., 2010). First, a background correction is applied in order to account for $^{13}C^{+}$ from broken up ^{13}CH reaching the detector. Second, the blank ratio is subtracted from all samples and standards. Carbon isotopes undergo fractionation processes on their way through the carbon cycle, during chemical treatment in the laboratory and during the AMS measurement due to mass dependent processes, which leads to an enrichment or depletion of certain isotopes.

To account for this effect and to allow a comparison of ^{14}C-ages of different materials, an isotope fractionation correction is applied when evaluating ^{14}C-data. The relationship between the fractionation of ^{14}C is approximately given by the square of the fractionation occurring to ^{13}C (Stuiver and Robinson, 1974). Therefore, the $^{13}C/^{12}C$-ratio is simultaneously measured to the $^{14}C/^{12}C$-ratio. Typically, the δ-notation is used when talking about stable C-isotope ratios which expresses the deviation of the $^{13}C/^{12}C$-ratio of a given sample to a standard:

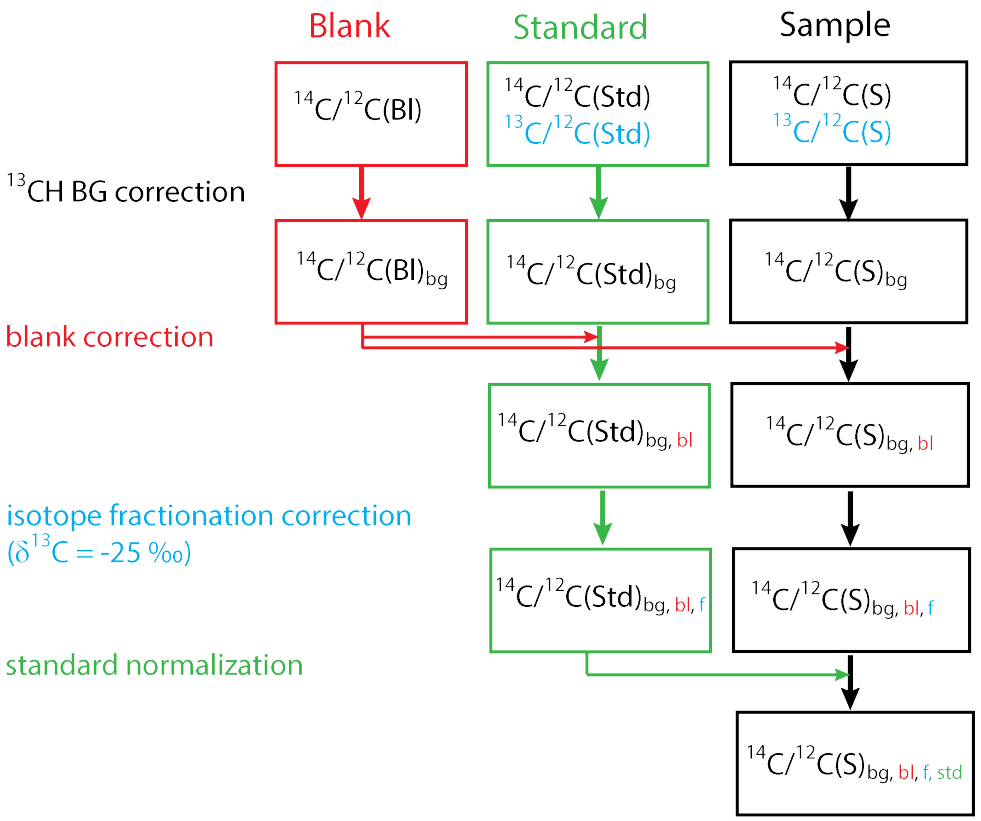

Figure 1.5: Overview of the data evaluation at the MICADAS using the BATS-software. The abbreviations are: BG = background, bl = blank, f = mass dependent fractionation, std = standard.

$$\delta^{13}C = \left(\frac{^{13}C/^{12}C_{sample}}{^{13}C/^{12}C_{standard}} - 1\right) \cdot 1000\,‰ \tag{1.8}$$

where carbonate material originating from a marine fossil from a Belemnite collected from the Cretaceous Pee Dee Formation in South Carolina, USA, called PDB, with a $^{13}C/^{12}C$ -ratio of 0.01124 is used as a standard material (Craig, 1957; Keith and Weber, 1964). ^{14}C-ages are by convention reported referring to a $\delta^{13}C$ of -25 ‰, as this value can be found in typical mid-latitude trees and plants.

The measured and $\delta^{13}C$ -corrected ^{14}C $/^{12}C$ -ratio is then reported as fraction of a modern ^{14}C standard denoted as $F^{14}C$ (fraction modern), which represents the activity ratio of the sample relative to a modern reference material (Edwards et al., 2003; Reimer et al., 2004). This reference value is defined as 95 % of the NIST Oxalic Acid I (OxI) in 1950, normalized to a $\delta^{13}C$ of -19 ‰relative to PDB and has a $F^{14}C$ of 1. The actual ^{14}C concentration of this standard corresponds to the ^{14}C content of wood from 1890 which is then decay corrected for 1950 to exclude the alteration of the ^{14}C $/^{12}C$ due to burning of

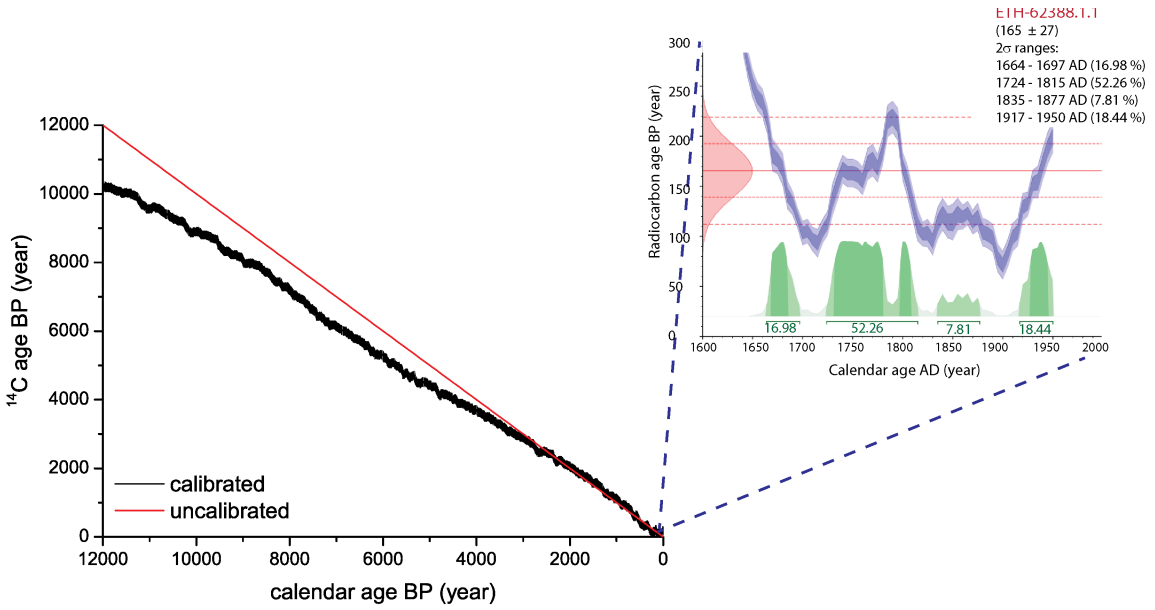

Figure 1.6: ^{14}C calibration curve (Reimer et al., 2013). If the ^{14}C-concentration was constant in the past, the calibrated age would be equal to the ^{14}C age (red line). Since this is not the case, a calibration curve is used to convert the measured ^{14}C age into a calendar age (black curve). In the inset a measured ^{14}C age with uncertainties (red) is calibrated (calibration curve = purple). Due to fluctuations in the atmospheric ^{14}C concentration in the past, ambiguities in the calendar age (green) can occur (note that the x-axis of the inset is converted to age AD).

^{14}C-depleted fossil fuel since the onset of industrialization in the late 19^{th} century known as the Suess-effect. Since the OxI standard is no longer available, other standards are in use today, such as the NIST OxII (SRM 4990 C) standard. All calculations can be found in Wacker et al. (2010).

The conventional ^{14}C-age is reported as years before present (BP) and according to Stuiver and Polach (1977) it is calculated using the following equation:

$$t = -8033\,yrs \cdot \ ln(F^{14}C) \tag{1.9}$$

where 8033 yrs denotes the lifetime of ^{14}C, which is calculated from:

$$\tau = \frac{T_{1/2}}{ln(2)} \tag{1.10}$$

Here, $T_{1/2}$ is the half-life of ^{14}C. The conventional ^{14}C age is independent of the year of measurement, as the measured activity ratio (sample vs. standard) stays constant over time. One assumption that Libby made when he introduced the ^{14}C dating method in the 1950s is that the atmospheric ^{14}C content is constant over time at a level of about 1.2 parts

per trillion relative to ^{12}C. But soon it became clear, that atmospheric ^{14}C production varied with time. Measured $^{14}C/^{12}C$ ratios do not reveal the actual age of an object, but have to be corrected by means of the ^{14}C calibration curve (Figure 1.6). The ages and concentrations are independently verified through other methods, for example tree-ring based dendrochronology or U-series dated corals (Reimer et al., 2004; Hughen et al., 2004; Fairbanks et al., 2005; Reimer et al., 2009, 2013). Due to the thorough mixing of ^{14}C in the atmosphere, a local dependence of the ^{14}C-content does not have to be considered (Lerman et al., 1970). The calendar age is reported as years before present (BP). The calibration curve reflects not only the constant decrease of ^{14}C in the atmosphere within the last few thousand years due to a weaker exchange rate between the atmosphere and other CO_2-reservoirs during the last ice age, but also displays the much faster changes in the $^{14}C/^{12}C$-ratio due to solar activity or climate variations. Therefore, the correlation between ^{14}C age and calendar age can be ambiguous, as shown in the inset of Figure 1.6.

1.5 Sample preparation for AMS analysis

Most samples analyzed with AMS are converted into graphite, as high negative ion currents of 40 to 60 μA and ionization efficiencies up to 10 % (Southon and Santos, 2007; Schulze-König et al., 2010a) can be achieved. Even though fully automated graphitization systems exist (Wacker et al., 2010), the process of sample preparation - especially for environmental samples like speleothems or corals - is time consuming and elaborate (Schleicher et al., 1998); typically only about 8 samples per day can be produced. Furthermore, relatively large samples in the range of 100 μg C are needed, since with smaller sample sizes the problem of contamination gets more pronounced (Jenk et al., 2007). Nevertheless, as shown by Santos et al. (2007) and Drosg et al. (2007) it is possible to graphitize samples of only a few micrograms of carbon, but this can hardly comply with the rising demand for ultra-small samples, e.g. in environmental and biomedical sciences. Another approach to measuring such small sample sizes is the use of a gas ion source. Besides it's ability to measure about ten times smaller samples than for solid samples of 1 to 50 μg (Ruff et al., 2010a; Fahrni et al., 2013), a gas ion source has the advantage of reducing sample preparation as only one combustion step is needed, reducing the overall analysis time. In addition, direct coupling for online analysis is possible, i.e. via an elemental analyzer (Uhl et al., 2004; Ruff et al., 2010b) or an aerosol filter analyzer (Perron et al., 2010). Drawbacks of the direct gas injection into a negative ion source are that ^{14}C gas measurements produce lower ion currents and have lower ionization efficiencies and, hence, very long measurement times are needed to reach a precision of 5 ‰ as required for ^{14}C dating. Nevertheless, great improvements have been made recently by Fahrni et al. (2013) showing that ion yields of 8 % and negative ion currents up to 20 μA can be reached with the gas ion source at the LIP ETH Zurich, making the dating of gaseous samples with a content as low as 50 μg C at a precision 5 ‰ possible.

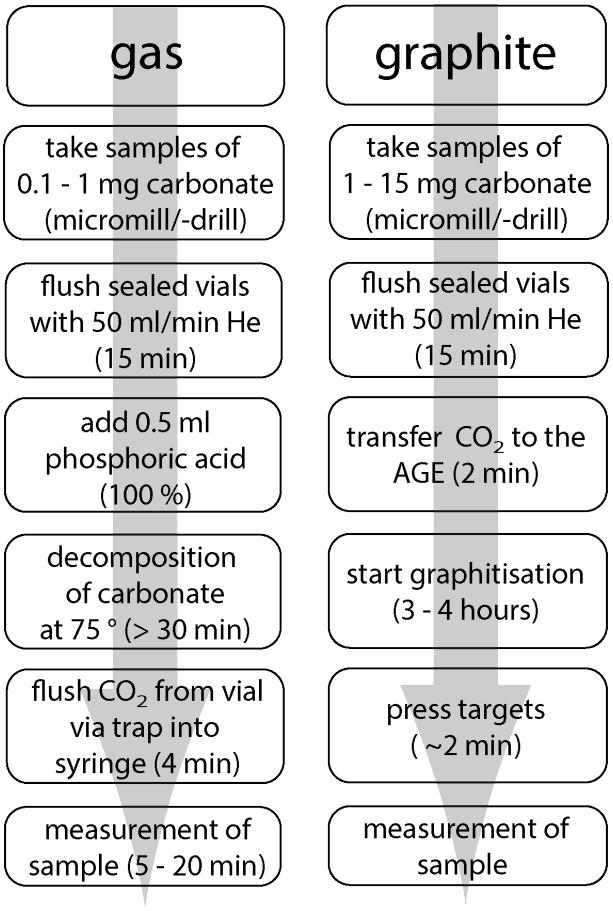

Figure 1.7: Overview of the sample preparation for conventional ^{14}C AMS measurements.

1.6 Laser Ablation

With the introduction of the laser in 1960 (Maiman, 1960) many applications emerged in a veriety of fields ranging from medical (Anderson and Parrish, 1983) and thin-film deposition (Inam et al., 1988; Witanachchi et al., 1989; Mao et al., 1990) to analytical sciences (Honig and Woolston, 1963; Darke et al., 1989; Thompson et al., 1981). By focusing a high-energy laser pulse on the surface of condensed matter, a small quantity of material is removed. Today, different analytical methods make use of this so-called laser ablation (LA) as a sampling tool. Localized chemical analysis at high spatial resolutions of 1 - 100 μm with little to no sample preparation is possible. Commonly used techniques include Laser Induced Breakdown Spectroscopy (LIBS) (Miziolek, 2006) and Matrix-Assisted Laser Desorption Ionization mass spectrometry (MALDI) (Karas et al., 1991). Another widely applied technique for sensitive trace-element and isotope-ratio analysis is Laser Ablation Inductively Coupled Plasma Mass Spectrometry (LA-ICPMS) (Gray, 1985; Russo et al., 2002; Günther and Hattendorf, 2005). In principle, this setup requires a pulsed laser source,

beam delivery optics to focus the laser on the surface of a sample that is hosted in an air tight ablation cell. The ablated material, which ideally has an elemental composition identical to that of the original sample, is transported through an aerosol transport line to an ICP ion source where particles are vaporized, atomized and ionized. These ions are then introduced into the mass spectrometer through a pressure reducing interface and subsequently separated according to their mass to charge ratio. There is a great variety of mass spectrometers coupled to an ICP ion source. Most commonly used are quadrupoles and sector field, but time of flight (TOF) instruments and multi-collectors (MC) are also in use.

For a long time LA-ICPMS was not accepted as a standard method for the analysis of solid materials because quantification was found to be difficult. Errors are caused by the LA process itself, aerosol formation and transport, as well as the vaporization, atomization and ionization processes in the ICP. The non-stoichiometric effects called elemental fractionation are a major problem when applying LA-ICPMS (Kuhn and Günther, 2003; Kroslakova and Günther, 2007). This leads to the need of matrix-matched external calibration standards for quantification. However, standard materials rarely match the matrix of the samples of interest. The main difference between laser systems used for LA with regard to the ablation behavior are the wavelength, output energy and pulse duration. Furthermore, the carrier gas and the LA-cell play an important role for the analysis technique. Numerous studies comparing laser wavelengths (Motelica-Heino et al., 2001; Hattendorf et al., 2003), pulse duration (Poitrasson et al., 2003; Koch et al., 2004; Gonzalez et al., 2006), type and flow rate of the carrier gas (Horn and Günther, 2003; Wang et al., 2006) and the LA cell design (Pisonero et al., 2006a; Bleiner and Bogaerts, 2007) have been carried out since the first time LA was applied. Other factors include the price, robustness and maintenance of the laser system.

1.6.1 Lasers types applied in laser ablation

The most common laser sources for LA-ICPMS are Nd:YAG lasers because they are reliable, robust, easy to use and relatively inexpensive lasers (Jackson, 2001). The fundamental wavelength is in the infrared spectral range at 1064 nm, which is not suited for many LA sampling applications, as it is poorly absorbed by many materials. Unwanted thermal effects, i.e. melting, boiling and evaporation, predominate. The particle size distribution (PSD) of the generated aerosol depends also on the wavelength (and on the sample material) and that the abundance of large particles, formed from splahsed droplets increases for longer wavelengths (Guillong et al., 2003). This enhances the noise in the transient signals and promotes chemical fractionation as particles with diameters larger than 0.15 μm are difficult to transport and less likely to vaporize completely in the ICP (Guillong and Günther, 2002). As a consequence, lasers emitting in the ultraviolet spectral range are preferred when coupled with an ICPMS. Therefore, most often the 4^{th} and 5^{th} harmonic

output at wavelengths of 266 nm and 213 nm, respectively, are used (Günther and Heinrich, 1999; Günther et al., 2000; Jeffries et al., 1998; Liu et al., 2000), even though this 'gain' in having shorter wavelengths goes together with a loss in energy. The active medium of these solid state lasers consists of an yttrium aluminum garnet rod doped with Nd^{3+} ions at a concentration of 1 % (Silfvast, 1995). The pumping is achieved optically by flash lamps or LEDs and the pulsing is attained by a Q-switch yielding pulse durations between 5 and 10 ns at Full Width Half Maximum (FWHM). The output frequency of flash lamp-pumped Nd:YAG lasers reaches up to 20 Hz. Laser systems with both, Gaussian and flat top beam profiles are available. In the case of Nd:YAG lasers, usually unstable resonators create a pseudo homogeneous beam profile. Even though quadrupled and quintupled Nd:Yag laser ablation systems can improve laser ablation substantially in comparison to IR laser sources, elemental fractionation and matrix-dependency remain a problem.

Laser systems emitting in the vacuum (V)-UV spectral range below 200 nm have been shown to significantly suppress the formation of micrometer-sized particles for non-metallic materials (Guillong et al., 2003). Commonly used VUV-lasers for LA-ICPMS are ArF excimer lasers operating at 193 nm with typical pulse durations between 10 and 40 ns. Excimer lasers refer not only to EXCited dIMERs but to any laser media that reach a population inversion by using a bound excited state and a transition to the dissociative ground state. This can be achieved by an electrical discharge producing very high electron densities of up to $10^{15}\,cm^{-3}$ (Basting and Marowsky, 2005) which leads to a population of the upper laser level in the same order of magnitude. The energy level diagram is shown in Figure 1.8. Electrons produced during the discharge react with the gas atoms and molecules and, after a sequence of collisions the excited (ArF)* molecules, are formed either through an ionic or neutral channel. Some of these reactions require the presence of an impact partner. The active medium of excimer lasers, therefore, consists not only of argon und fluorine gas but also of helium and neon as a buffer gas. The high voltage that is required to produce such gas discharges is realized through a storage capacitor and a thyratron switch (von Bergmann et al., 2005).

The main advantage of ArF-excimer lasers is their short wavelength, which leads to strong absorption by most materials. By focusing the beam, high pulse energy densities can be obtained. Due to their poor spatial coherence, interferences are minimized, which reduces problems in the optical handling and imaging of the laser beam. Generally, excimer lasers have a Gaussian beam profile in one direction, while the other direction is a flat top. With a special lens array (Günther et al., 1997) a flat top in both directions can be realized. Disadvantages of ArF laser include their much higher beam divergence when compared to Nd:YAG lasers, their low efficiency and moderate pulse-to-pulse stability. Frequent maintenance in the form of gas fillings of the cavity, in order to maintain maximum output energy, is required, which is accompanied by high operating costs. ArF excimer lasers have been successfully applied in numerous studies (Günther et al., 1998; Koch et al., 2002; Liu et al., 2002).

More recently, femtosecond lasers have been used with LA-ICPMS. When analyzing

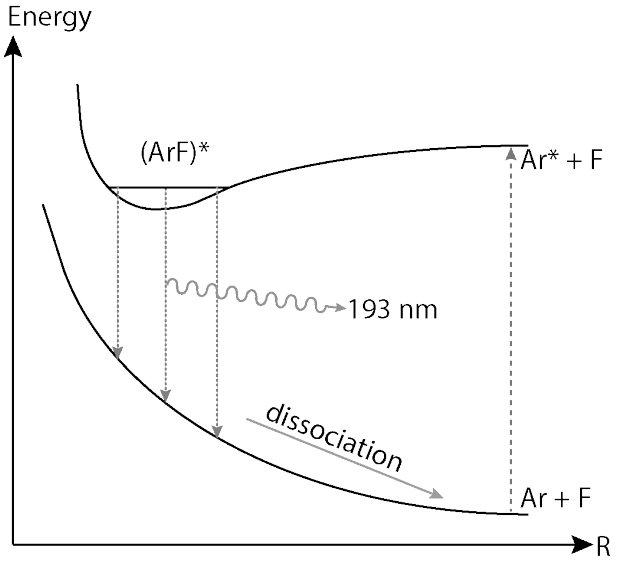

Figure 1.8: Energy level diagram of an ArF excimer laser (adapted from Demtröder (2007))

.

metals and semiconductors, the ultra-short laser pulses are much better suited because the formation of a heat-affected zone (i) and plasma shielding (ii) are avoided (Koch and Günther, 2011). (i) The heat-affected zone is formed as a result of the heat diffusion out of the irradiated volume into the target, which leads to material re-distribution during the ablation process and can cause intensive fractionation (Le Harzic et al., 2002). By making the laser pulse duration shorter than the time it takes to transfer the absorbed pulse energy from the electrons to the lattice (thermal relaxation time, electron-phonon-coupling), the energy transfer can be suppressed. Typical thermal relaxation times in metal are on the order of a few hundred femtoseconds (Rethfeld et al., 2004). (ii) The plasma shielding is the interaction between the incident laser beam and the vapor/ plasma plume above the ablation spot. If the laser intensity is sufficiently high to form a plasma, the plume strongly absorbs laser light and shields the target from the incident beam (Bäuerle, 2000). This process is negligible for ultrashort laser pulses. Therefore, when applying fs-LA, the phase transition from solid to gaseous or to superheated liquid is completed before the onset of energy diffusion within the lattice or absorption of the incident laser beam by ejected material. The analytical performance of LA systems is mainly determined through the stoichiometry of the laser-generated aerosol. Fs-LA has the potential to eliminate fractionation effects as well as matrix dependence. It furthermore improves the spatial resolution as the craters have well defined edges (Hergenröder et al., 2006). Most commonly Ti:Sapphire Lasers are used to generate ultrashort laser pulses between 5 fs and a few hundred ps. The wavelength of these solid state lasers can be tuned from 670 to 1080 nm. Furthermore, higher harmonics can be used to create ultra-short UV laser pulses.

Table 1.1: Overview of laser systems

wavelength [nm]	Laser medium	Laser type	pulse energy [mJ]	pulse duration
1064	Nd:YAG	solid state	100 - 2000	5 - 10 ns
$\sim$ 800*	Ti:Sapphire	solid state	2.8	$<$ 150 fs
266	Nd:YAG	solid state	1 - 100	5 - 10 ns
$\sim$ 265*	Ti:Sapphire	solid state	0.23	$<$ 150 fs
213	Nd:YAG	solid state	0.1 - 20	5 - 10 ns
$\sim$ 200*	Ti:Sapphire	solid state	$<$ 0.05	$<$ 150 fs
193	ArF	gas excimer	5 - 200	3 - 15 ns

* from Koch et al., 2006

1.6.2 The ablation process

On a first glance LA can be understood as the rapid boiling of material on the surface of a piece of condensed matter. But the fundamental physical processes that laser ablation is based on are complex, ranging from electronic excitation and subsequent conversion into thermal, chemical and mechanical energy and finally resulting in the rapid removal of material from the surface of a solid target. The ablation mechanism is not entirely understood even today, as the details depend on many factors including the type of target material (metal, dielectric, organic material), laser parameters like the wavelength (VIS, UV, VUV), pulse duration (ns, ps, fs), fluence (0.5 - 20 J/cm^2) and intensity, and also on the ablation environment (ambient pressure and gas composition). In the following, for simplification the LA process is briefly described using the example of fs laser pulses interacting with solid states as the stages can be treated as decoupled. A comprehensive description also applicable to ps- and ns-LA can for instance be found in Chichkov et al. (1996).

The ablation process (depicted in Figure 1.9) begins with the absorption of incident photons by free or bound electrons of the solid sample. On a picosecond time-scale, the energy of the electrons is transferred to the lattice by collisions of the electrons with phonons, and the lattice is heated. Electrons are ejected and collide with the ambient gas atoms which results in a plasma formation above the sample surface after ns. Material is ejected from the ablation site by evaporation and explosive boiling and finally, the target re-solidifies.

Material ejection and plasma formation

Depending on the laser fluence and on the laser pulse duration delivered to the sample, melting, vaporization, normal boiling or even explosive boiling may occur, which results in the ejection of mass:

(i) Vaporization (evaporation and sublimation) describes the transition from a solid or

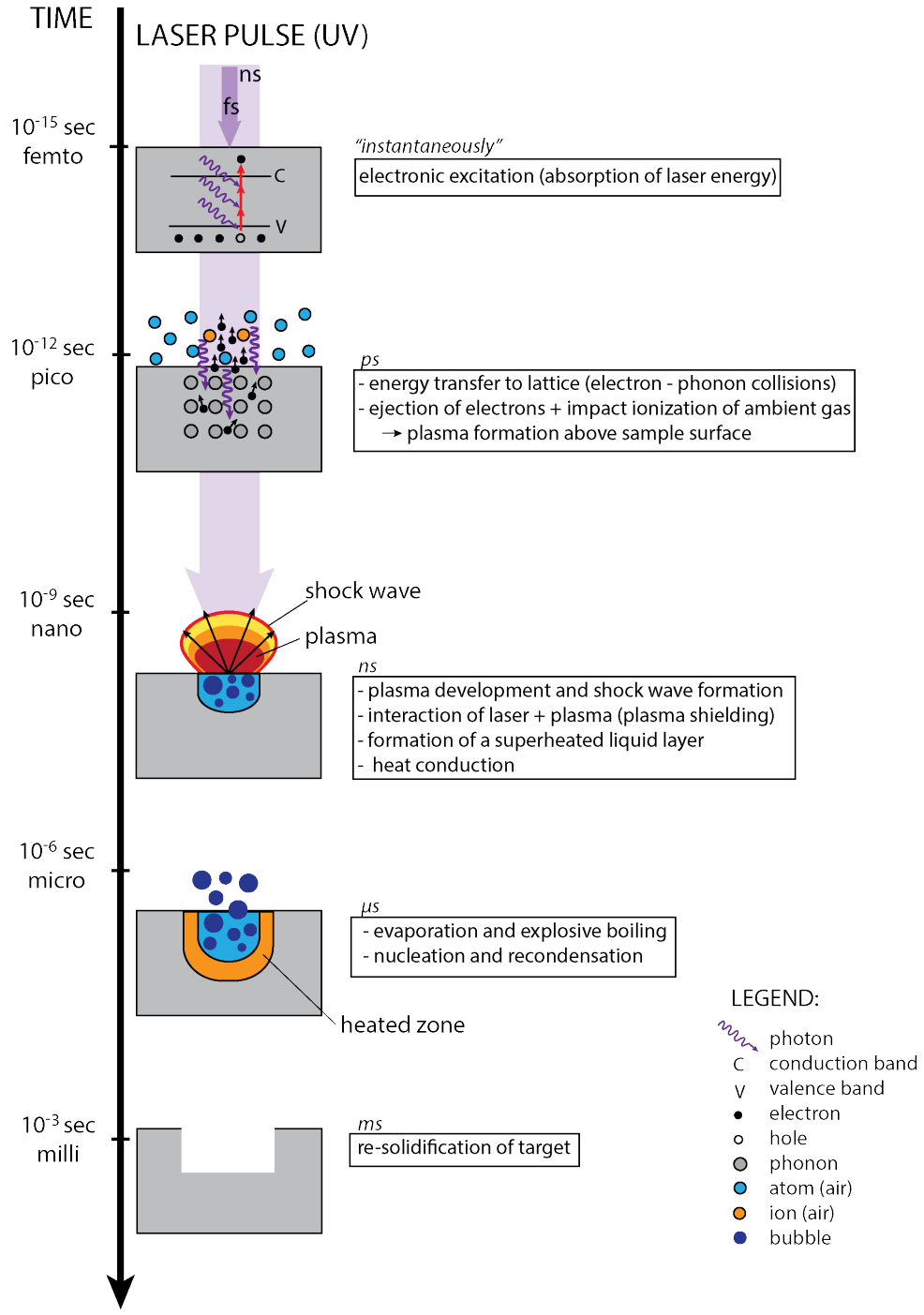

Figure 1.9: Chronology and stages of the ablation process. The duration of a fs and a ns laser pulse are indicated by the violet arrows. Decoupled stages- as shown in the figure - correspond to LA with fs lasers. Details can be found in the text. Ideas for this figure were taken from Mao (2005).

liquid to vapor by the emission of atoms or molecules from the outer surface through electron-phonon-coupling. This process will not occur for very short time-scales, i.e. if the laser pulse duration $\tau_L < 1\,\text{ns}$ and for longer pulse durations only if the temperature exceeds the material's boiling temperature T_b.
(ii) Normal boiling is defined through the formation of vapor bubbles when the material is heated, which diffuse and if $T > T_b$ (material's boiling point) escape from the liquid. Bubbles may form at the outer surface of liquid, in the bulk of the liquid or in the underlying or enclosing solid surface. In all three cases the bubbles are hindered by obstacles either in the process of bubble formation or bubble diffusion. Therefore, normal boiling is negligible if $\tau_L < 100\,\text{ns}$.
(iii) The third and most efficient sputtering process for thermal laser ablation is the explosive boiling (Miotello and Kelly, 1999). If the temperature is close to the thermodynamic critical temperature T_{tc}, superheating occurs, i.e. liquid droplets and vapor coexist. This leads to a phase explosion by homogeneous nucleation meaning that the hot region near the surface breaks down in a very short time into vapor plus equilibrium liquid droplets. The total flux of ejected particles can change dramatically when the laser fluence is increased sufficiently to induce explosive boiling.

The laser material interaction will cause a dense plume (plasma) to appear above the sample surface, which consists of clusters of the ablated material, molecules, atoms, electrons and ions that form due to collisions between electrons and the atoms/molecules of the gas-phase (Bäuerle, 2000, p. 207). Long lasting laser pulses - as in the case of ns lasers - will efficiently be absorbed especially by the free electrons through inverse bremsstrahlung (Bäuerle, 2000, p. 209) where photons are absorbed by free electrons in the presence of an atom or ion. On the one hand the plasma shields the target from further direct ablation, but on the other hand it transfers energy to the sample. Consequently, melting and further vaporization enhance the thermal processes on the sample surface and at the same time reduce the efficiency of the laser sampling. The plasma expands while in the case of ns-LA the laser pulse is still present.

Adiabatic plume expansion and recondensation

As soon as the laser pulse terminates, no more energy is transferred to the plume. In vacuum conditions and at very early stages, the expansion can be considered to be an adiabatic process, meaning that no thermal energy is exchanged with the surrounding. Initially, the expansion of the plume is primarily driven by the plasma pressure gradients (Hughes, 1975), but an additional driving force is likely to result from the Coulomb repulsion between the ions if there is a significant loss of electrons (Phipps and Dreyfus, 1993; Dreyfus, 1991). Most of the energy of the plume is present in the form of ionized and excited species or thermal energy and is transferred into kinetic energy of the particles within the first few hundred μm of the plume expansion (Haught and Polk, 1970; Puell, 1970) reaching velocities between 10 and 20 km/s (see Schou et al. (2007)).

If the ablation takes place in the presence of a gas at an ambient pressure of p_g>0.1 mbar, the interaction of the expanding plume with the surrounding gas needs to be considered. This interaction is a complex gas dynamic process including the deceleration of the plume while it compresses and thereby heats up the ambient gas. The expansion stops when the internal pressure of the plume has reached the background pressure. This is typically the case after a few μs (Amoruso et al., 2006). The plume deceleration results in the formation of an external shock wave. While the plasma itself is slowed down, the shock wave expands and its density, temperature and pressure decrease. Eventually it is transformed into a sound wave. The plume itself also gets compressed at its outer edges when interacting with the ambient gas, which can lead to the formation of an inner shock wave travelling back towards the target, where it is reflected and causes a mixing of the plume. While the plume expands, the degree of ionization rapidly decreases mainly by electron-ion-recombination until the plasma becomes collision less after several mm to cm depending on the ambient pressure. The lower the pressure, the larger is the stopping distance and the further the plume expands (Cristoforetti et al., 2004; Iida, 1990).

While the plume is expanding, pressure and temperature drop, resulting in a super saturation of the gas species. Molecular clusters start to form in an increased number and grow until they reach a critical size and become stable. Subsequently, atoms from the plume condense on the nuclei, forming particles up to 1 nm. Nucleation and condensation eventually result in the formation of particles between 50 and 250 nm (Guillong et al., 2003; Koch et al., 2004). Secondary pathways, such as coagulation and agglomeration, form particle sizes between 100 - 1000 nm (Jaworski et al., 2002). Smaller particle sizes can be achieved through less melting, higher energy deposited per volume and a smaller heat affected zone (Russo et al., 2013) which can be achieved through shorter wavelengths and pulse durations. Furthermore, a smaller particle size distributions (Russo et al., 2004) and less re-deposition on the target (Hirata and Miyazaki, 2007) was observed when ablating in a low pressure environment.

1.6.3 LA-cells

For analysis using LA, the sample has to be placed in an ablation cell, where the gas-aerosol is mixture is produced and confined. The shape and size of the LA-cell can influence the aerosol transport from the ablation site to the ion source of the mass spectrometer. Typically, circular ablation cells with inner volumes at the order of 60 mL are applied, where a pressurized inlet for carrier gas (helium or argon) is used to transport the aerosol through the outlet into the MS (Hattendorf, 2002). Many other designs have been developed (Leach and Hieftje, 2002; Pisonero et al., 2006b; Gurevich and Hergenroeder, 2007) mostly reaching for high aerosol extraction efficiencies and fast washout times, i.e. signal drop over time. Short washout times make the overall analysis faster and increase the signal-to-noise ratio. Shortest washout times of LA-cells are at the order of a few milliseconds (Tanner and Günther, 2006) to 30 milliseconds (Wang et al., 2013) at the cost of sample size. Potential

samples for analysis using the LA-AMS setup are carbonate records, such as stalagmites or corals which can be large samples. Each time the record is cut into smaller pieces, valuable information is lost. Therefore, besides the need of a small volume, the capability of hosting large samples is a desirable characteristic for the LA-AMS cell. Fricker et al. (2011) presented a LA-cell that combines relatively short washout times at the order of a few seconds while accepting large samples, by designing a restricted effective volume for the aerosol expansion.

1.7 Motivation and aim of the present work

LA-based sampling in combination with gas ion source AMS provides a unique flexibility for rapid and high spatially resolved ^{14}Canalyses in carbonate records. The requirements of an AMS with a negative ion source using a Cs primary beam for sputtering are very specific and differ from other mass spectrometric techniques. In particular the gas ion source used in the MICADAS system requires a continuous and stable supply of CO_2 over a relatively long time of 10-15 minutes. Additionally, the carbonates have to be converted into CO_2, requiring a sufficiently high yield in order to reach the optimum C-flow on the order of 3 μg/min (Fahrni et al., 2013). Operation of the gas ion source requires the absence of larger quantities of oxygen and nitrogen in the gas stream to ensure stable operation of the titanium sputter targets. The gas flow rates typically used for gas measurements are on the order of 0.1 mL/min, which is much lower than gas flow rates of 1.0 L/min applied for LA coupled with ICPMS.

1.7.1 Previous work and proof of principle

The use of LA with AMS for ^{14}C analysis has been reported once (Rosenheim et al., 2008). In this pilot study, CO_2 was produced using a commercial 213 nm LA system, flushed onto a CO_2-trap, graphitized and subsequently measured as a conventional solid AMS target. Efficiency tests were performed by comparing the mass of the ablated material with the amount of CO_2 generated yielding a maximum efficiency of 30 % at a laser fluence of 20 - 25 J/cm^2 using a pulse frequency of 20 Hz. The rates of CO_2 generation were very small - on the order of 1 μg/min - which lead to long sampling times. Fractionation tests were performed by comparing the δ^{13}C and Δ^{14}C gained from laser-generated CO_2 and conventional acid-generated CO_2 from the same sample. It was concluded that fractionation was not a concern, unlike for stable isotope determinations of C and O of carbonates sampled by laser ablation (Sharp, 1992; Cerling and Sharp, 1996). Although this study demonstrated the principal applicability of LA sampling for ^{14}C analyses of carbonates, the suggested method could not benefit from the latest developments on online injection of CO_2 into an AMS gas ion source.

Therefore, a proof of principle experiment was conducted at the Laboratory of Ion Beam Physics (LIP), where a commercial 213 nm LA system was coupled with the gas ion source of the MICADAS (Wacker et al., 2013). The sample was placed in an airtight cell and set to a pressure of 200 mbar He. The laser was operated at an output energy of 2.7 mJ/pulse at 20 Hz and set to a spot size of 150 μm. Two stalagmites were analyzed. One was considered a ^{14}C-blank and showed a contamination of approximately 5 % of a modern sample, probably caused by air leaks into the ablation cell; the other had a known ^{14}C age which could be reproduced within one standard deviation. The CO_2-yield was estimated to be on the order of 70 % which is higher than observed in the study by Rosenheim et al. (2008). The C production rate was 1.5 μg/min, which is, however, significantly lower than the optimum conditions at the MICADAS gas ion source. For this experiment, the laser was operated at its maximum output energy and frequency. Therefore, the routine analysis of carbonate records by LA requires a more powerful laser system to meet the optimum conditions of the MICADAS. Furthermore, a designated cell that has the ability to hold large samples, ensures efficient transport of the generated CO_2 and minimizes cross-contamination is desirable.

1.7.2 The potential of LA-AMS for carbonate records

A dedicated LA-AMS system for the online analysis of ^{14}C in carbonates has a great potential for many applications; the most prominent candidates are speleothems and corals, but generally other solid and carbon-containing materials could also be analyzed. There are numerous possible applications benefiting from such a setup:

(i) In the case of young (< 200 - 300 years) speleothems, U/Th-ages are often insufficiently precise due to low Th-concentrations. Alternatively, ^{14}C from the nuclear weapons testing in the 1950s and 1960s if present in the record can be used to establish a chronology (Hodge et al., 2011; Hua et al., 2012) for the younger part of the speleothem. (ii) ^{14}C can be used as a geochemical tracer for carbon soil dynamics helping to gain a deeper understanding of the complex processes that carbon undergoes in the soil (Genty et al., 1998; Genty and Massault, 1999; Fohlmeister et al., 2011; Rudzka-Phillips et al., 2013). The C found in stalagmites has two main sources (see Section 1.2) and undergoes numerous processes changing its relative isotopic composition before it is incorporated into the speleothem. One source of C in stalagmites is the CO_2 in the soil air, which determines the C composition in the seepage water. The second source is formed by the (^{14}C-devoid) host rock carbonates that are dissolved when in contact with the acidic soil water. The so-called dead carbon fraction (dcf) is a proxy for infiltration, overlaying vegetation and weathering (Griffiths et al., 2012; Genty et al., 2001; Fohlmeister et al., 2011), which are all controlled by climate. Models of isotopic exchange in karst aquifers consider in general two limiting cases of carbonate dissolution that occur under open and closed conditions (Hendy, 1970; Wigley, 1975; McDermott, 2004). There is evidence for a correlation between the amount of precipitation and the ^{14}C concentration in stalagmites, and it has been

suggested that during dryer periods the isotope exchange between soil water and soil air is more pronounced, i.e. more open conditions, and vice versa (Fohlmeister et al., 2010). The highly resolved investigation of the impact of the amount of precipitation on the ^{14}C activity in a stalagmite seems a promising tool to get new information on the CO_2 gas exchange system in the overlying soil. (iii) Furthermore, high resolution ^{14}C-records of cold water corals could be of interest for the tracing of water masses. A homogeneous mixing of ^{14}C in the deep ocean is not possible because of its relatively short half-life compared to oceanic mixing times. Therefore ^{14}C recorded in deep water corals can be used as a tracer to detect broad redistributions of water masses for instance a stop or a slowing down of North Atlantic deep water production (Frank et al., 2004). A spatially high-resolution LA-AMS can be used to investigate reservoir ages by performing measurements on corals with distinct growth layers. One requirement for this method is that at least one accurately measured age point is known, for example by Th/U-dating, in order to assign an absolute age to the annual growth layers. (iv) The ^{14}C-bomb peak can be used to determine the entry of bomb-^{14}C into the ocean by spatially high-resolution ^{14}Cmeasurements on very young corals. Frank et al. (2004) already found evidence for a bomb-^{14}C entry in deep sea corals. LA-AMS applied to young corals growing at different depths would allow to determine oceanic mixing rates.

1.7.3 This work

The scope of this work covers different steps that allow the coupling of LA with AMS. These are (i) the investigation and optimization of the CO_2-production efficiency for LA sampling of different laser systems, (ii) design and construction of a dedicated LA-cell with short response times while accepting large samples, (iii) the optimization and characterization of the new LA-AMS system and finally (iv) the application of the new LA-AMS combination for ^{14}C measurements of real carbonates like speleothems and corals.

2 Fundamental experiments

In the following chapter, studies on fundamental aspects, important for the coupling of LA with AMS, are presented. Properties of LA applied to carbonate samples, including the CO_2 conversion rate and the ablation threshold as well as operation of the AMS gas ion source at high carrier gas flow rates, are addressed.

2.1 CO_2 conversion efficiencies of different laser sources

During LA, material from the sample surface is removed and a mixture of a gas phase and particles is formed. The composition of the material removed by the laser is influenced by the sample's matrix, laser parameters such as the wavelength and the laser energy and by the ambient pressure in which the LA process takes place. Frick and Guenther (2012) found that when carbon containing matrices are ablated, the ratio of the gas phase compared to the particle phase is smaller for oxygen-free matrices, such as diamond and graphite. In contrast, the ratio of gas to particles was highest for organic samples that contain a large amount of oxygen. In the case of carbonates, the CO_2-conversion efficiency, i.e. the proportion of removed material forming the gas phase compared to the total ablated material, has been shown to range from 30 % Rosenheim et al. (2008) to 50 % Wacker et al. (2013). For online-^{14}Cmeasurements using LA-AMS a long capillary is connected between the ablation spot and the ion source and consequently particles need to be filtered out to avoid clogging. So far, only the gas phase of the laser-produced aerosol contributes to the ^{14}C-analysis and, therefore, an important step towards coupling LA with AMS is to employ a laser system with a sufficiently high (i) CO_2 production rate and (ii) CO_2-conversion efficiency. (i) The CO_2-production rate is a measure for the amount of CO_2 formed without considering the amount of sample material necessary for the production of the gas. (ii) The CO_2 conversion efficiency is of greater importance for LA-AMS measurements, as it directly compares the amount of CO_2 produced to the total ablated sample material. In the following experiment both quantities are determined for different laser sources.

2.1.1 Experimental setup

Three commonly used laser systems for LA-ICPMS were compared with respect to their CO_2production rate and conversion efficiency in this experiment: an ArF excimer laser (GeolasC, $\lambda = 193$ nm, Microlas GmbH, Göttingen, Germany), a Nd:YAG laser (LSX213,

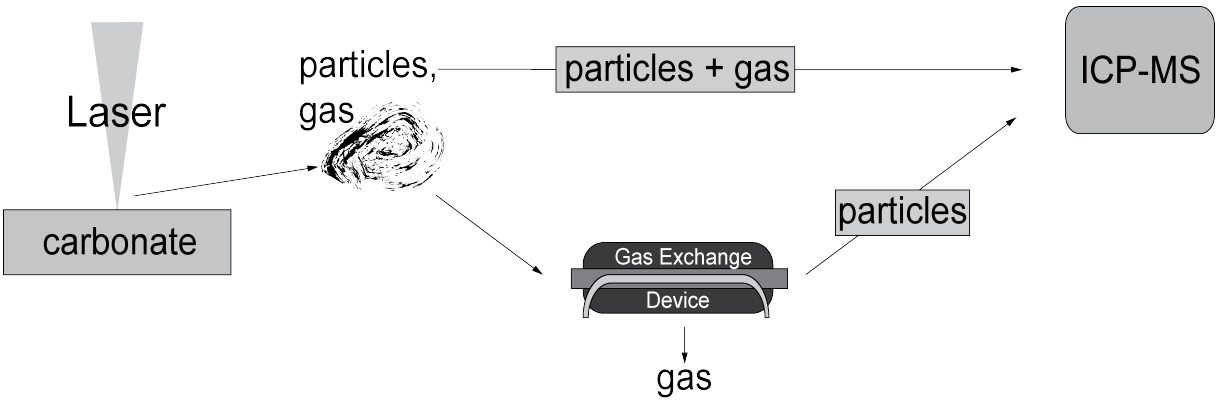

Figure 2.1: Experimental setup for determining the CO_2-production efficiencies of different laser sources. The ablated sample is either guided through the GED where the gas component is replaced with argon or it is directly transported to the ion source of the ICPMS.

5ω, $\lambda = 213\,\text{nm}$, CETAC Technologies, Omaha, USA) and a Nd:YAG laser (LSX500, 4ω, $\lambda = 266\,\text{nm}$, CETAC Technologies, Omaha, USA) were successively coupled to an ICPMS (Elan 6100 quadrupole MS) and for each laser system, first the entire laser-produced aerosol and second, only the particle phase was analyzed. The initially produced gas phase was exchanged by guiding the mixture of gas and particles in He at a flow rate of 1 L/min through a gas exchange device (GED) (Kovacs et al., 2010; Nishiguchi et al., 2008) placed between the LA-cell and the ICPMS. The GED consists of a porous tube which is used to transport the laser-aerosol while an Ar counter-flow of $4\,\text{L}\,\text{min}^{-1}$ at the outside is applied. Due to the partial pressure difference between the regions, the CO_2 is removed from the aerosol flow, while the laser-produced particles enter the ion source in a pure Ar atmosphere. An overview of the experimental setup is shown in Figure 2.1. For all measurements a thin section of a natural stalagmite was ablated.

In order to keep the plasma conditions equal for both cases (with and without GED) the gas flow rates of He and Ar were adjusted for each measurement. For measurements without GED, the nebulizer gas flow of the ICPMS was set to $0.8\,\text{L}\,\text{min}^{-1}$ and the He carrier gas flow rate to 1 L/min. Since with GED the gas is replaced with Ar at a flow rate of 0.32 $\text{L}\,\text{min}^{-1}$ (verified with a mass flow meter), the nebulizer gas flow was reduced to 0.48 L/min and an additional He-flow of 1 L/min was introduced into the plasma downstream of the GED. All instrumental parameters are listed in Table 2.1.

Prior to analysis the ICP operating conditions were optimized with regard to maximum signal to background ratio and minimum oxidation rates in order to reduce spectral interferences and maximize sensitivity. The transient signals for ^{12}C, ^{13}C, ^{42}Ca, ^{44}Ca were collected with a dwell time of 10 ms. For calibration a 5 % CO_2 in He 5.0 mixture (Messer Schweiz AG) at a flow rate of 0.6 mL/min was introduced together with He at a flow rate of 1 L/min in the ICPMS.

Table 2.1: Instrument settings

ICPMS	**without GED**	**with GED**
instrument	ELAN 6100 DRC+	
carrier gas flow	1 L/min He	1 L/min He replaced by 0.3 L/min Ar
nebulizer gas flow	0.8 L/min Ar	0.5 L/min Ar
additonal gas flow	none	1 L/min He
RF Power	1400 W	
lens setting	autolens calibrated	
detector mode	dual	
dwell time	10 ms	

LA			
laser systems	**Cetac LSX-500, Nd:YAG**	**Cetac LSX-213, Nd:YAG**	**Geolas C, ArF excimer**
wavelength (nm)	266	213	193
pulse duration (ns)	5	5	15
repetition rate (Hz)	10	10	10
spot size (μm)	150	100	90 and 120
fluence (J/cm^2)	4.2	3.3 - 19.1	7.1 - 22.5
lateral velocity (μm/s)	20	20	20

Calibration gas	
gas type	5 % CO_2 in He 5.0, Messer Schweiz AG
gas flow rate (mL/min)	0.6

2.1.2 Results and discussion

The CO_2 production rates, i.e. the CO_2 volume produced per unit time and unit area, for the three laser systems is calculated according to the following procedure: the average intensity in counts per second (cps) of the transient signal for each isotope was calculated and background corrected. In order to account for the loss of particles (CaO and $CaCO_3$) via sedimentation in the GED, a correction factor Q_{corr} was calculated. As Ca is only present in the solid phase, it is assumed that the sensitivity of the Ca-isotopes with and without GED is the same.

$$Q_{corr} = I_{42Ca,GED}/I_{42Ca} \tag{2.1}$$

where $I_{42Ca,GED}$ and I_{42Ca} denote the signal intensities for ^{42}Ca with and without GED, respectively. On average this factor was 78 % ± 5 %, except for one measurement day with the LSX213, where a value of 32 % ± 1 % was found. The correction factor was applied to the carbon signal of measurements with GED, which was then subtracted from the ^{12}C intensity of measurements without GED yielding the difference in carbon signal intensity Δ^{12}C.

$$\Delta^{12}C = I_{12C} - I_{12C,GED} \cdot Q_{corr} \tag{2.2}$$

From the signal intensity I_{CO2} of the CO_2 calibration gas and its known volume flow $F(CO_2)$ into the ICP a calibration factor $E(CO_2)$ for the LA measurements can be assessed:

$$E(CO_2) = \frac{I(CO_2)}{F(CO_2)} \tag{2.3}$$

This can be used to calculate CO_2 production rate for the LA-measurements by using the following equation:

$$Production_{CO_2} = \frac{\Delta^{12}C}{E(CO_2)} \tag{2.4}$$

Finally, the production rate is converted from a volume into a mass. The CO_2 production rates calculated for different laser fluences range from 0.6 to 1.1× 10^{-7} μg/(pulse · μm^2) and are depicted in Figure 2.2 (a). A dependence on the laser fluence and on the wavelength can be seen. For higher fluences more CO_2 per unit time is produced. Furthermore, shorter wavelengths results in a higher CO_2 production rate. The error bars result from error propagation and are based on the standard deviation of the collected signal and of the background.

The CO_2 conversion efficiency, which describes the proportion of gas formed relative to the

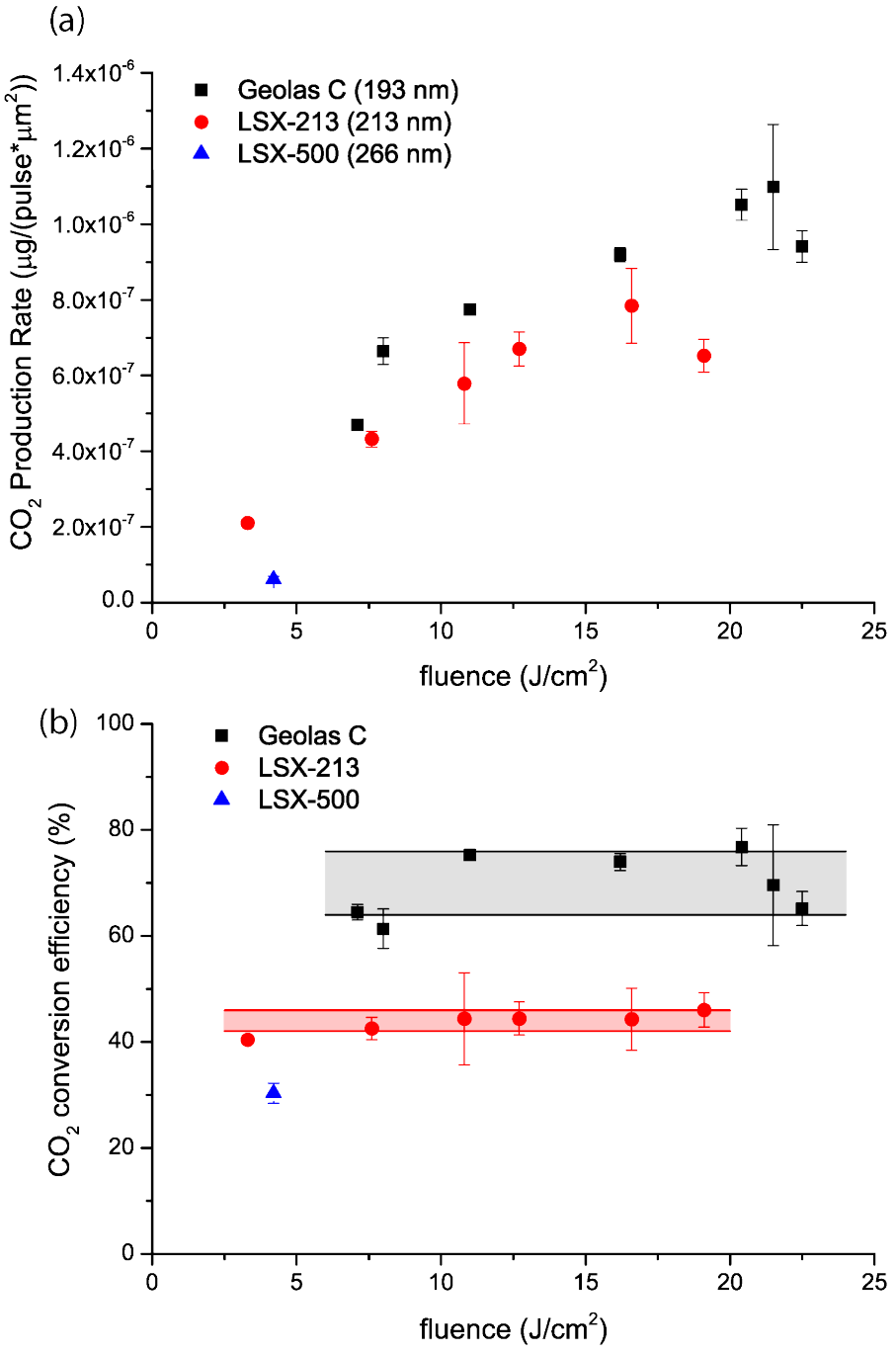

Figure 2.2: (a) CO_2 production rates for three laser systems at different fluences. Geolas C and LSX 213 exhibit a similar trend. Only one data point is available for LSX500 at its maximum energy. The CO_2-production rate increases with shorter wavelength. (b) CO_2-production efficiencies for the three laser systems at different laser fluences. The solid horizontal lines represent one standard deviation. The CO_2 production efficiency depends rather on the fluence than on the wavelength.

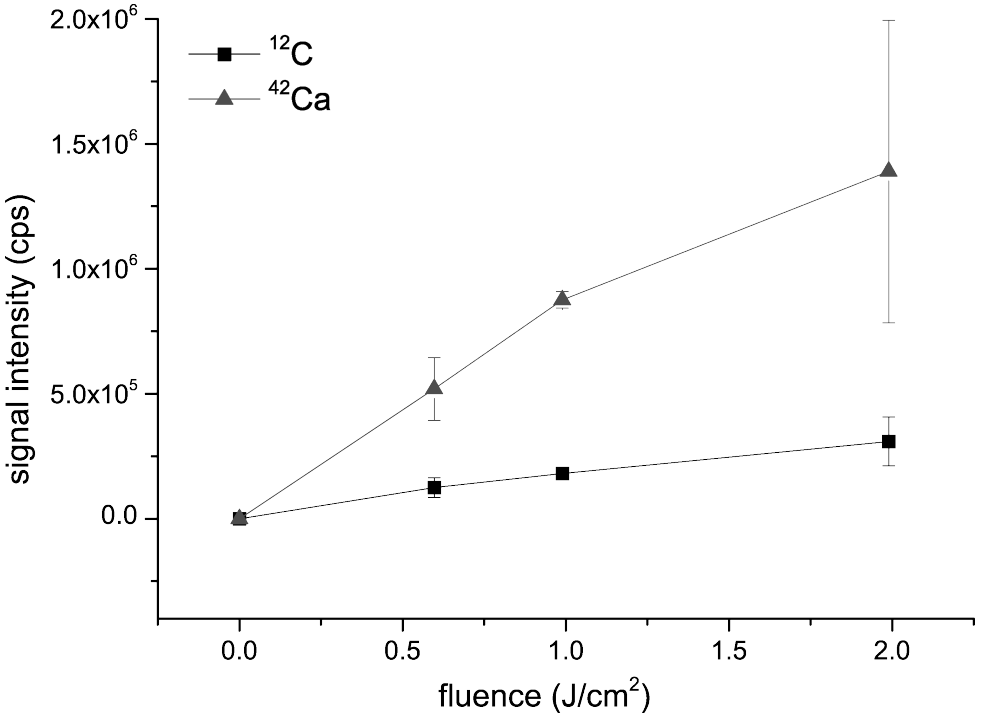

Figure 2.3: Dependence of the signal intensity on the laser fluence for a wavelength of 193 nm.

total amount of material removed, is calculated. The C signal representing the gas phase (Δ^{12}C) is divided by the C signal corresponding to the mixture of solid and gas phase. The results for the different fluences are summarized in Figure 2.2 (b) where no fluence dependency can be observed. The average and standard deviation of the different fluences for each laser is taken (compare colored boxes in Figure 2.2 (b)). A trend can be seen for the different lasers, showing that the conversion efficiency for shorter wavelengths with (70 $\pm$ 6) % at 193 nm is about 1.5 times higher than for 213 nm with(44 $\pm$ 2) % and about twice as high as for 266 nm with 30.3 %. No uncertainty for the LSX500 is given, since this experiment was only conducted for one fluence. For the calculations above it was assumed that CaO and $CaCO_3$ sediment in a comparable way in the GED. This is most likely not the case and, therefore, it needs to be considered that the results presented in this section are correct in a relative perception, but the absolute values need to be confirmed by another method. An over estimation of the sedimentation rate results in an under estimated CO_2 production rate and conversion efficiency and vice versa. Nevertheless, it can be concluded that shorter wavelengths result in higher CO_2-production rates and conversion efficiencies, making the ArF excimer laser best suited for the coupling of LA with AMS.

2.2 Ablation threshold for carbonates

For a certain fluence, referred to as 'threshold fluence', the onset of ablation can be observed, i.e. irreversible damage occurs to the sample and bulk material is removed. In order to investigate the ablation threshold of an ArF excimer laser operating at 193 nm (GeolasQ) for a carbonate sample, an experiment was performed where the laser frequency and spot size were kept constant, while the laser fluence was varied. A dense piece of natural $CaCO_3$ (stalagmite) placed in a regular round ablation cell (Hattendorf, 2002), which was connected to an Elan 6100 ICP-Q-MS. The carrier gas was set to 1 l/min of He, a spot size of 90 μm diameter and a frequency of 10 Hz were selected. The laser fluence was varied from 0.6 to 2 J/cm^2 and the transient signal of ^{12}C, ^{13}C, ^{42}Ca, ^{44}Ca was collected by the ICPMS for 60 sec for each fluence and two replicates were performed for each setting. For each isotope the average of the transient signal was taken and background corrected and the results for ^{12}C and ^{42}Ca are shown in Figure 2.3, where the error bars correspond to the standard deviation of the two replicates. It can be seen that material is ablated from the carbonate samples even when using fluences below 1 J/cm^2.

2.3 C-flow calibration at the MICADAS

Fahrni et al. (2013) showed that the C^--current obtained during gas measurements at the MICADAS is very sensitive to the C flow rate and the Cs temperature. For conventional gas measurements a capillary with an inner diameter (I.D.) of 60 μm and a length of 100 cm is used to restrict the gas flow rate to approximately 110 μL/min. The LA-AMS setup was designed in a way that gas flow rates are at least a factor of two higher, in order to ensure reasonable washout times of the LA-AMS cell. Therefore, the behavior of the ion source for these high gas flow rates was investigated using the well characterized gas interface system (GIS) (Ruff et al., 2007; Fahrni et al., 2013) that is employed for conventional gas measurements at the MICADAS AMS system. A capillary with measures intended for the LA-AMS setup (I.D. = 150 μm, length = 100 cm) was connected between the GIS and the ion source. The experimental setup is depicted in Figure 2.4 (a) (adapted from Ruff et al. (2007)). A mixture of 5 % CO_2 in helium (Messer Schweiz AG, Lenzburg, Switzerland) was diluted with helium to concentrations between 0.5 and 5 vol% in the syringe. The mixtures were measured at three different gas flow rates (0.2, 0.4 and 0.6 mL/min).
The signal was collected for 3 to 5 minutes for each concentration and flow rate and the mean $^{12}C_{HE}$-current, which is approximately a factor of 2.5 lower than the true ion source output, was calculated. Up to five replicates were performed for each pair of settings and the mean as well as the corresponding standard deviation were derived and are depicted in Figure 2.4 (b). For each gas flow rate the ion current as a function of the C mass flow is shown. The behavior previously observed by Fahrni et al. (2013) is also reflected in this data set: starting with low C flow rates, a positive correlation between C flow and ion

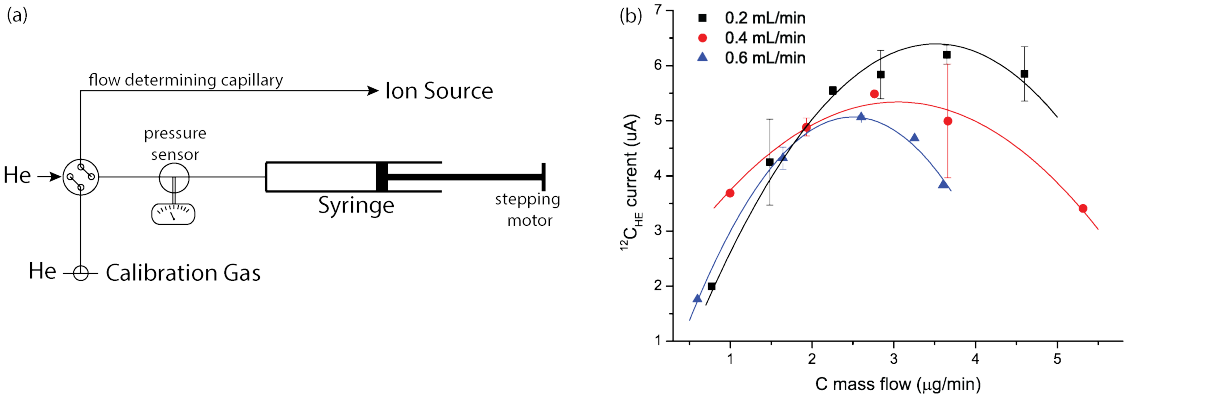

Figure 2.4: (a) Setup of the gas interface system in combination with the LA-AMS capillary. The desired CO_2 concentration is mixed in the syringe to a certain pressure and this mixture is then introduced into the ion source via the LA-AMS capillary that defines the gas flow rate for a given pressure. The pressure in the syringe is maintained by a stepping motor decreasing the syringe's volume.

current is observed, until a maximum is reached. If the C flow is further increased, the ion current drops. The maximum ion current is known to shift towards higher C-flow rates and to reach higher values with increasing Cs intensity (Fahrni et al., 2013). Nevertheless, in this experiment higher gas flow rates result in lower maximum ion currents than lower gas flow rates. Furthermore, for higher gas flow rates the maximum C ion current is reached for lower C mass flow rates and a drop in the maximum current is observed.
The experiment was repeated and the same behavior was observed. Possible reasons for the reduced sputtering efficiency when applying higher helium gas flow rates could be that this increased flow rate results in a cooling of the titanium target. Furthermore, the mean free path of the CO_2 is shortened and, consequently, fewer CO_2 molecules reach the titanium surface. The higher gas flow rates result in a decrease of the vacuum in the ion source, which possibly leads to (i) a neutralization of produced negative ions and (ii) in the cooling of the ionizer.

2.4 Summary

Three commonly in LA-ICPMS employed laser sources were compared with regard to their CO_2 conversion efficiencies and CO_2 production rates. Both quantities were highest for an ArF excimer laser, making this the most suitable source for LA-AMS, where only the gas fraction can be sputtered. The threshold fluence of the ArF excimer laser on carbonate samples was found to be below $1\,J/cm^2$, which implies to select the laser energy on the sample surface and the laser spot size used in LA-AMS accordingly.

The gas ion source of the MICADAS AMS system commonly accepts gas flow rates on the order of 0.1 mL/min. It was shown, that flow rates up to 0.6 mL/min yield LE ion currents of more than 16 μA, which is sufficient for ^{14}C analysis at the expense of efficiency.

3 Instrumental setup*

A mixture of a particulate and a gas phase is formed when ablating $CaCO_3$. The respective amounts of these phases depend on several parameters like the laser wavelength and energy as well as the ambient pressure in the LA-cell. Once the CO_2 gas phase is produced by LA, it needs to be transferred into the gas ion source of the AMS as rapidly as possible. To ensure optimal operation of the gas ion source it needs to be fed with a certain C-flow rate, i.e. an optimum concentration of CO_2 in He and gas flow rate. These parameters, in turn, depend on the pressure in the LA-cell and on the laser fluence but also on the dimensions of the transfer capillary. The optimization of a dedicated LA-AMS system is therefore a multi-parameter design process. In this section, the general requirements and the design considerations of the LA-AMS setup are presented, separated into its main parts:

i The laser system with its optics and the sample observation unit,

ii the LA-cell that houses the sample and where the CO_2 is produced,

iii the gas handling system that is used to transport the CO_2 into the ion source and

iv the AMS with its gas ion source where the CO_2 is converted to negative C ions.

3.1 Laser system and sample observation

ArF excimer lasers operate at a short wavelength (193 nm) and the beam is absorbed within a comparably thin layer on the target surface, making them ideal candidates for LA-sampling. In the previous chapter it has been shown, that excimer lasers have the highest CO_2conversion efficiency compared to other laser sources commonly employed in LA-sampling. Therefore, an excimer laser (Ex5, Argon Fluoride 193 nm, GAM LASER, Orlando, USA) with a maximum output energy of 12 mJ per pulse and an average power of 2.4 W at 250 Hz is selected for the LA-AMS setup. The gas mixture used to operate the laser consists of 15 ppm mol xenon, 0.13 % mol fluorine, 3.1 % mol argon and neon as a carrier gas. The repetition rate ranges from 20 to 250 Hz and the beam size is 3 x 6 mm^2. In order to keep the setup compact, a trolley was designed where the laser is placed below the optical setup as shown in Figure 3.1. Right after the laser output an aperture is placed for the regulation of the spot size, which is followed by a periscope that consists of two 45° dielectric mirrors guiding the beam to the upper part of the trolley and rotating it through 45°.

*Parts of this chapter are submitted to publication (Welte et al., submitted)

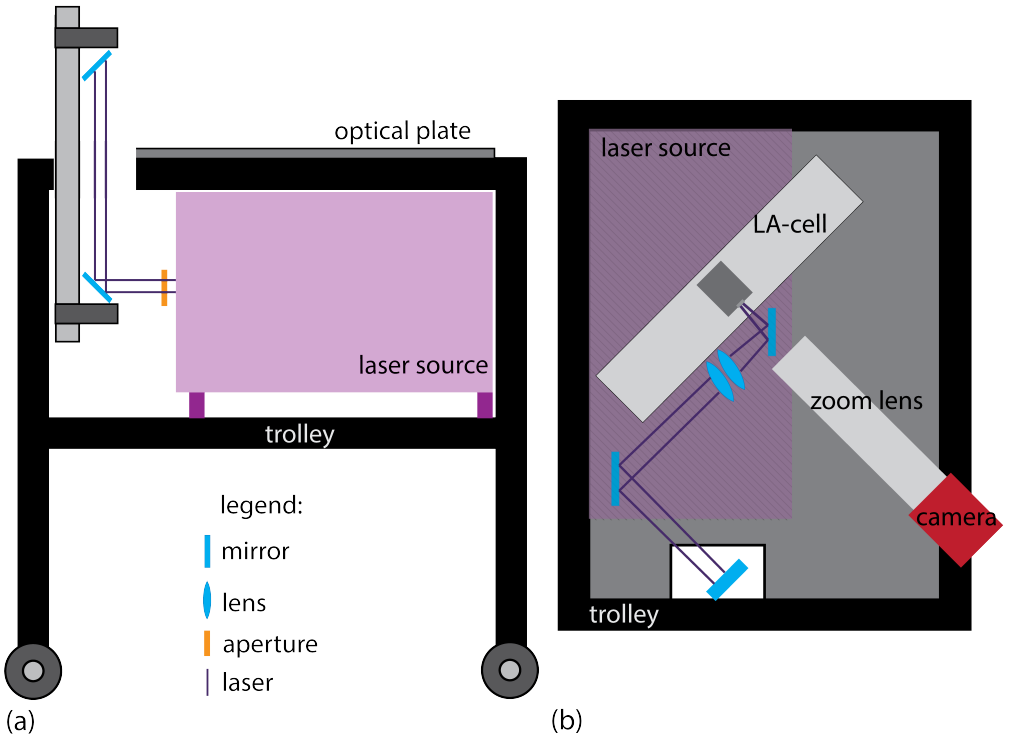

Figure 3.1: Setup of the laser and the optics on the trolley. (a) The laser is placed below an optical breadboard and the beam is guided via a periscope to the upper deck. A PC and the ArF gas cylinder are placed on the other half of the trolley (not shown). (b) Two additional mirrors are used to guide the beam to the sample and to focus it using an objective lens.

A third mirror reflects the beam towards a lens, which is mounted on a translation stage with an increment width of 0.03 mm (0.24 mm per turn) and a maximum range of 12 mm. For the initial setup a UV fused silica plano-convex lens with a focal length of 75 mm for visible light was used. A steering mirror is placed behind the lens reflecting the beam at an angle of incidence of 45° down into the cell, rotating the beam through another 45° back in order to produce craters on the sample that are parallel to the growth layers. The laser beam path after the last mirror coincides with the axis of the observation, which consists of a monochrome CCD camera AVT MANTA G-125B with a 1/3' sensor and 3.75 μm pixel size and a zoom lens OPTO TUBUS Z-1,0/146 with a working distance of 15 mm and a magnification of 0.72x to 4.23x. The illumination is supplied by an in-house fabricated ring-illumination, consisting of 16 white LEDs with a luminous intensity of 18 cd and an angle of radiation of 22°. Routine operation of the LA-AMS unit revealed, that the illumination was better when only the top three LEDs were used. A linear polarizer with N-BK7 protective windows suitable for 400-700 nm is placed between the zoom lens and the illumination to prevent interferences on the observation from reflections.

The optical setup allows the observation of low-contrast samples placed under the cell

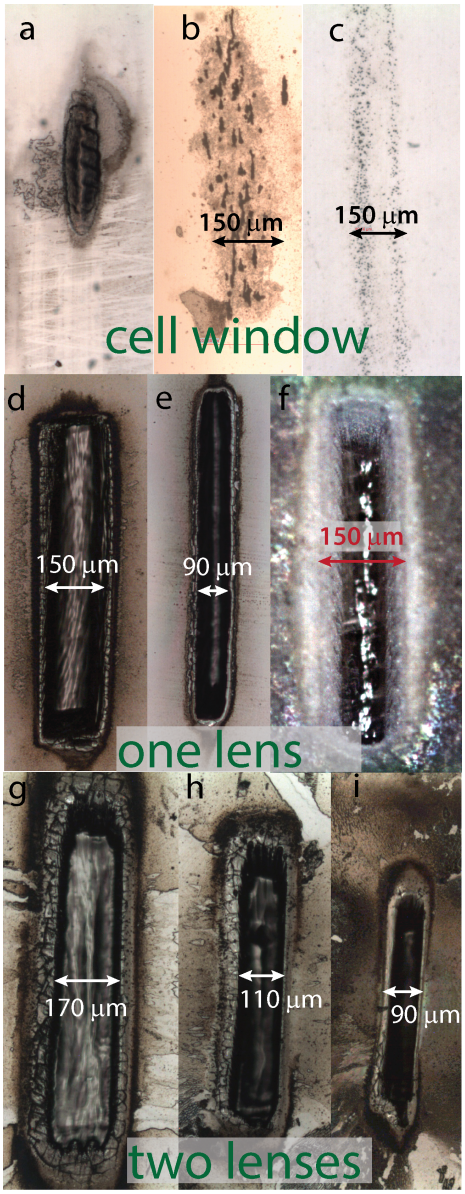

Figure 3.2: Upper row: (a) and (b) damaged cell window for a focal length of 100 mm and 75 mm, respectively. (c) Particle deposits on the cell window (f = 75 mm). Middle row: craters in a microscope slide for a focal length of 75 mm (d) without aperture, (e) with aperture, (f) without aperture in a carbonate sample. Lower row: craters in a microscope slide for a focal length of 5.5 mm. The lens is closest to the sample in (g) and furthest away in (i)(increment for lens ∼0.3 mm).

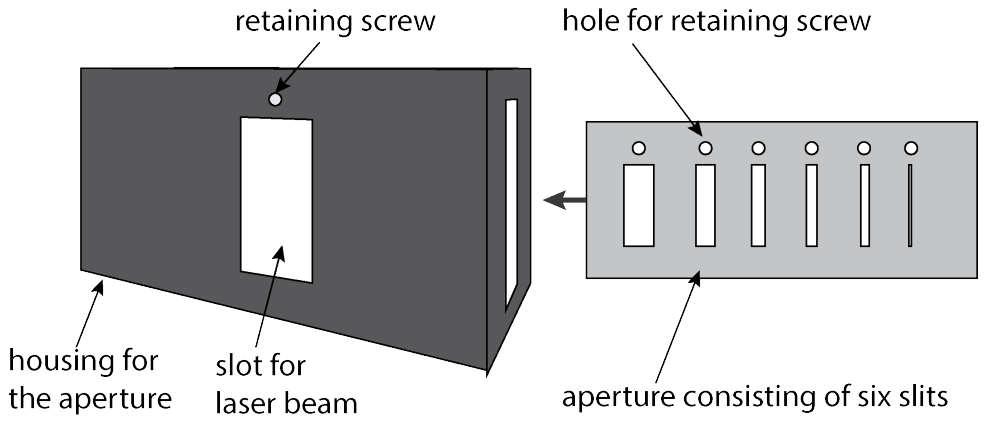

Figure 3.3: Scheme of the apertures and of the aperture holder used for the LA-AMS setup. Six slits of different thickness are manufactured in the aperture plate and the selected slit is fixed relative to the laser beam by the retaining screw.

'head' with a volume of only ∼600 μL (see next section). The focal distance of the lens is chosen such, that the distance between the lens and the sample is large enough to place the last mirror in-between them, but at the same time short enough to avoid the fluence on the cell window to reach the ablation threshold. Therefore, initial tests with a lens of a focal distance of f = 100 mm were conducted and showed, that for low fluences on the order of 0.2 J/cm^2 on the sample surface already ablation of the cell window ocurred after 2500 laser pulses (Figure 3.2 (a)). When using a lens with f = 75 mm, slight traces of ablation on the window were visible at energy densities of 0.5 J/cm^2 (Figure 3.2 (b)). Furthermore, in Figure 3.2 (c) the particle deposition on the inner side of the cell window after 140 000 laser pulses using f = 75 mm is depicted. The particles have sizes of several μm, which is in accordance with the largest particles generally found from laser ablation.

Craters produced with one lens (f = 75 mm) after 100 laser pulses in microscope slides used as samples are shown in Figure 3.2 (d) - (f). In all three pictures, the focus is positioned on the sample surface. In picture (d) no aperture is used yielding a rectangular crater of 150 μm x 800 μm, while in Figure (e) a slit aperture (width = 1 mm) was placed right after the laser output yielding crater dimensions of 90 μm x 800 μm. Craters in a stalagmite sample are shown in part (f), where no aperture was used. For the final LA-AMS setup, the focal length of the lens was further reduced in order to increase the window's lifetime. An objective lens for UV-radiation with a total focal length of 55 mm was used, which further reduced the fluence on the window. The objective lens consists of two lenses, both made of uncoated fused silica: a convex lens with a focal length of 40 mm (VIS) and a concave lens with a focal length of -100 mm (VIS). They were placed in series in a lens tube with a retaining ring of 1.7 mm width between them. The lens system was moved in 0.3 mm steps and for each step 100 laser pulses were fired on a microscope slide. Pictures of the corresponding craters are depicted in Figure 3.2 (g) - (i). Starting on the left (g) the lens system is the closest to the sample (the focus being 'below' the sample's surface)

and with each picture to the right, the lens is moved further away from the sample. The craters get smaller as the focus moves towards the sample surface with the focus meeting the sample surface in (h), where the pit shows the best-defined outline measuring 110 x 680 μm. Moving the lens-system further away results in deformed and smaller craters, which can be explained by spherical aberration. All pictures were taken using a microscope (Olympus BX-51, Olympus Schweiz AG, Volketswil, Switzerland). Lenses with shorter focal lengths generally result in larger image aberrations. This is due the smaller curvature radius, which requires thicker lenses and, furthermore, the effect of spherical aberration is increased. When lens doublets instead of lens singlets are used, the effect is even amplified. Therefore, the crater shape for the lens doublet (Figure 3.2 (i)) is not as well defined as for the longer focal distance (Figure 3.2 (d)) used before.

Three apertures made from thin stainless steel plates of 0.5 mm thickness each with six slits of equal height (6, 4 and 2 mm) but different width (3, 2.5, 2, 1.5, 1 and 0.5 mm) allow to adjust the crater size. The aperture and housing are depicted in Figure 3.3 and the slit sizes with the corresponding crater sizes are listed in Table 3.1.

3.2 LA-cell development

The LA-cell is constructed as a compound system that consists of two parts: the 'ablation head' where the aerosol expansion takes place and the 'sample box' where large samples with dimensions of up to 150 × 25 × 15 mm^3 can be placed. An important aspect of the LA-cell is its influence on the effect of cross-contamination between two subsequently measured samples. In the small volume of the cell head, the particles ejected from the sample deposit on the cell walls and window. After some time the particles can get remobilized and fall back onto the sample where they mix with the currently analyzed sample or exchange reactions between the deposits and the produced CO_2 result in cross contamination.

3.2.1 Design and construction of the top part

First design

The principle of the cell head is depicted in Figure 3.4 (a). The inner volume is kept small with approximately 600 μL to ensure rapid gas exchange. Possible cross contamination by particles formed during previous laser pulses is minimized by placing the sample surface vertical so that aerosol particles preferably settle in the lower part of the ablation head, where re-mobilization by subsequent laser pulses is minimized (compare Figure 2). Similarly, particle deposition on the cell window is reduced by placing the perpendicular to the sample surface out of the direction of aerosol expansion. The stopping distance for

Table 3.1: Aperture measures and corresponding crater sizes

without aperture				
measures of laser beam		measures of crater		
length [mm]	width [mm]	length [μm]	width [μm]	area [μm^2]
6	3	705	121	85300
aperture 1				
measures of slit		measures of crater		
length [mm]	width [mm]	length [μm]	width [μm]	area [μm^2]
6	3	650	110	72000
6	2.5	610	110	67000
6	2	600	100	60000
6	1.5	560	80	45000
6	1	550	70	39000
6	0.5	570	50	29000
aperture 2				
measures of slit		measures of crater		
length [mm]	width [mm]	length [μm]	width [μm]	area [μm^2]
4	3	390	110	43000
4	2.5	390	100	39000
4	2	380	100	38000
4	1.5	380	80	30000
4	1	370	60	22000
4	0.5	360	40	14400
aperture 3				
measures of slit		measures of crater		
length [mm]	width [mm]	length [μm]	width [μm]	area [μm^2]
2	3	220	110	24000
2	2.5	210	100	21000
2	2	200	90	18000
2	1.5	200	70	14000
2	1	200	50	10000
2	0.5	180	40	7000

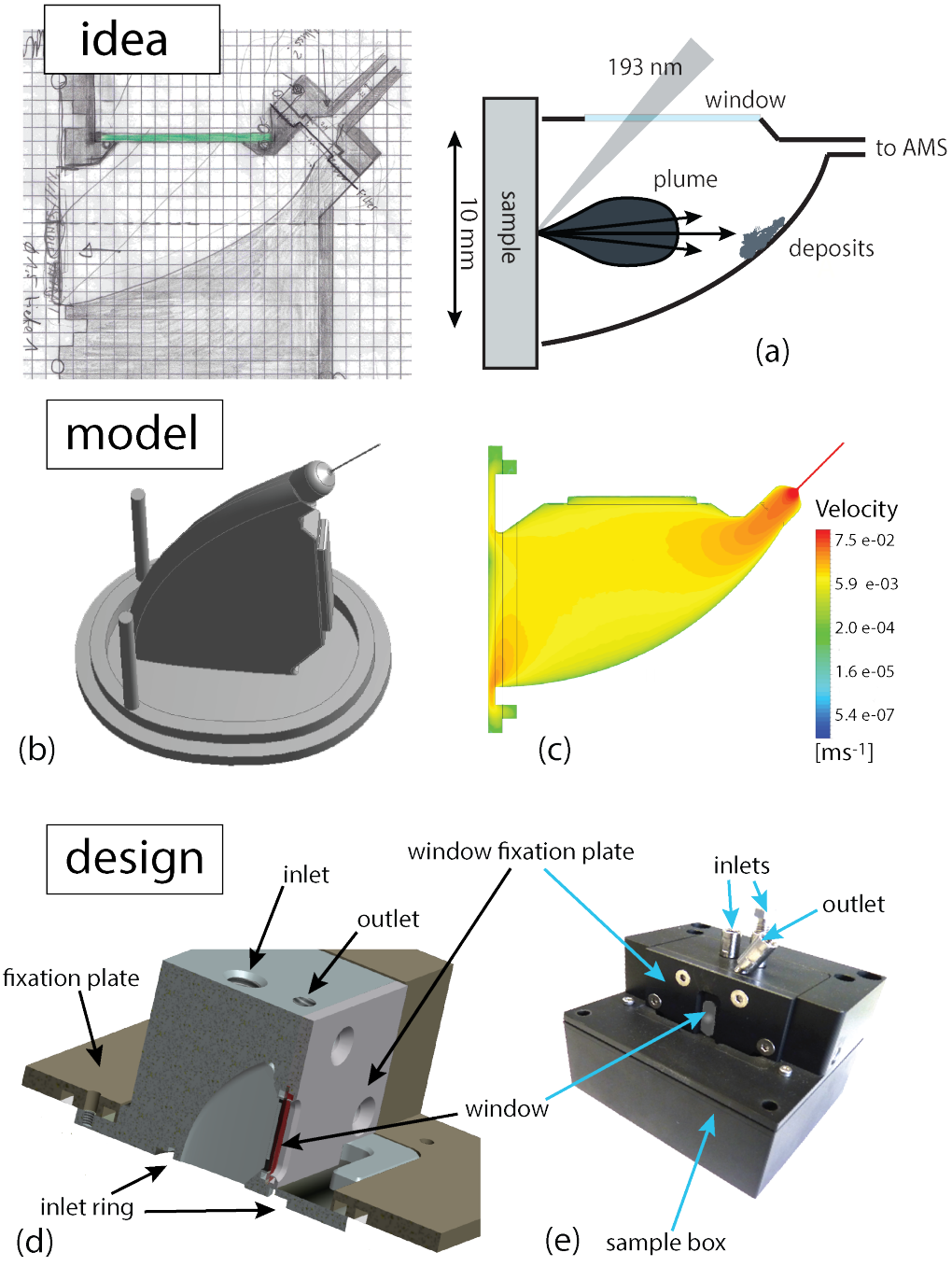

Figure 3.4: (a) Principle idea of the cell head: constraining the laser produced area in a defined volume, inhibiting deposits to fall onto the sample and placing the window out of the primary direction of particle expansion. (b) Inner cell volume desigend with ANSYS for modeling the gas flow dynamics and (c) velocity pattern within the cell head derived from computational fluid dynamics. (d) Cross-section of the the cell head and (e) picture of the cell head with a simple sample box.

the expanding particles was estimated from the ambient pressure and the laser energy (compare Bäuerle (2000)) yielding 2.5 mm for 1 bar and a laser energy of 0.5 mJ on the sample, therefore, ensuring that most particles will be stopped before reaching the window.

In Figure 3.4 (b) a scheme of the inner volume of the initial cell head ('version 1') is shown. A ring-system around the actual cell volume guides the gas from two inlets and supports gas flow into the cell from all sides. The inlets are placed towards the backside to provoke a flow towards the outlet, which is located at the opposite side of the cell. The gas flow dynamics in the inner volume of the cell head were modelled with computational fluid dynamics using the program ANSYS Academic Research, Release 12.1, CFX, ANSYS, Inc., 2009. First, the geometry was created where inlet and outlet areas with diameters of 0.5 mm and 0.22 mm, respectively, were defined. The flow of the incoming gas (helium) was set to 200 μL/min and a mesh consisting of 560,000 nodes and 3,000,000 elements was calculated. The resulting velocity pattern can be seen in Figure 3.4 (c). There are no areas within the cell that exhibit much smaller velocities than in the fast flowing regions, which indicates a quick gas exchange and confirms the suitability of this design for the LA-AMS setup.
A 3D scheme of the cell's cross-section is shown in Figure 3.4 (d). The cell is made from aluminum and anodized to minimize light reflections and thus improve sample observation. In order to reduce absorption and distortion of the laser beam, the window has a thickness of 0.5 mm. Window materials tested were CaF_2 and fused silica, both with 45° antireflection coating for 193 nm on both sides. The CaF_2 window only showed a slightly longer lifetime with respect to deterioration by the laser beam. The overall dimensions of the window are 25 x 15 x 0.5 mm (width x height x thickness) while only about 2 mm are used at a time. Therefore, the plate for fixing the window to the cell is constructed in a way that the window can be placed away from center towards both sides allowing to make use of the entire window. In Figure 3.4 (e) a photo of the finished cell top part is shown. For test reasons a preliminary sample box was constructed, which is fixed to the cell head with four screws. With this setup no scanning can be performed and only the about 2 mm wide and 10 mm long sample section accessible through the window can be used for measurements.

A first characterization of the cell head was performed by coupling it to an ICPMS and applying standard ICPMS conditions, i.e. ablation under atmospheric pressure using 6 mm teflon tubing and He carrier-gas flow rates of 1 L/min. The measurement was conducted with the Ex5 ArF-excimer laser (193 nm) and an Elan 6000 quadrupole ICPMS. The instrument was optimized for high signals and low oxide rates ($ThO^+/Th^+ \approx 0.2\,\%$) to ensure a high sensitivity. The ratio of U/Th was optimized to ∼1 to ensure complete vaporization of larger particles. For optimal ion transmission through the ICPMS, an auto lens calibration was performed. By conducting the dual detector calibration, measurement in pulse and analog mode was enabled. A dense piece of a natural carbonate was used as a sample and the isotopes monitored were ^{12}C, ^{13}C, ^{42}Ca and ^{43}Ca. All relevant settings

Table 3.2: Overview of the experimental settings for LA-ICPMS measurements

experiment experiment	**characterization cell head**	**comparison of inlets**	**washout LA-AMS/ conventional cell**
Sample	stalagmite	NIST 610	NIST 610
Isotopes	^{12}C, ^{13}C, ^{42}Ca, ^{43}Ca	^{23}Na, ^{12}C, ^{43}Ca	^{42}Ca
Carrier gas	1 L/min He	1 L/min He	1 L/min He
Nebulizer gas	0.8 L/min	0.6 L/min	0.6 L/min
RF Power	1400 W	1350 W	1350 W
Laser frequency	20 Hz	20 Hz	20/10 Hz
Laser frequency	0.3 - 1.6 J/cm^2	2.5 J/cm^2	2.5 / 13 J/cm^2
Spot size	0.08 mm^2	0.08 mm^2	0.08 / 0.03 mm^2

of the measurement can be seen in Table 3.2. Transient signals were obtained by using a measurement routine of 1 sweep per reading, 1000 readings and a dwell time of 10 ms yielding 1 minute and 5 seconds of measurement. The background signal was collected during the first 20 seconds, followed by lasing for 30 seconds. During the last 10 seconds the signal drop was recorded. This routine was repeated for laser fluence ranging from 0.3 to 1.6 J/cm^2. A typical transient signal can be seen in Figure 3.5 (a) measured at 1.6 J/cm^2.

The mean signal intensity for Ca and C isotopes is plotted against the laser fluence in Figure 3.5 (b). As expected, the mean intensitiy increases for higher fluences. In order to determine the CO_2 conversion efficiency of the Ex5 laser, the same setup, now with a membrane filter (0.4 μm pore size, Millipore, Billerica, MA, USA) connected after the outlet of the ablation cell, was used. Transient signals under equal ICPMS and LA conditions were obtained for different laser energies. In Figure 3.5 (c) the transient signal for the setup with filter is shown and it can be seen that for Ca, which is present exclusively in the solid particle phase of the laser-produced aerosol, signals are suppressed in comparison to Figure 3.5 (a) where no filter is used. In the case of C, signals are less attenuated because a great portion of C is present in the gas phase. The average of the transient C signal for each fluence was calculated and background corrected. By comparing measurements employing a filter with the ones without filter, the CO_2 conversion efficiency was estimated, which was found to be only marginally dependent on laser fluence between 0.5 and 2 J/cm^2. The mean conversion efficiency is 53 % $\pm$ 2 % (Figure 3.5 (d)), which is similar to values observed by Rosenheim et al. (2008) and Wacker et al. (2013), even though much higher fluences were applied. The results obtained with the Geolas C in Section 2.1 are somewhat higher, but in the same range as the values mentioned before. Possibly, the sedimentation rate of particles in the GED has been under estimated, which leads to an over estimation of the CO_2 conversion efficiency.

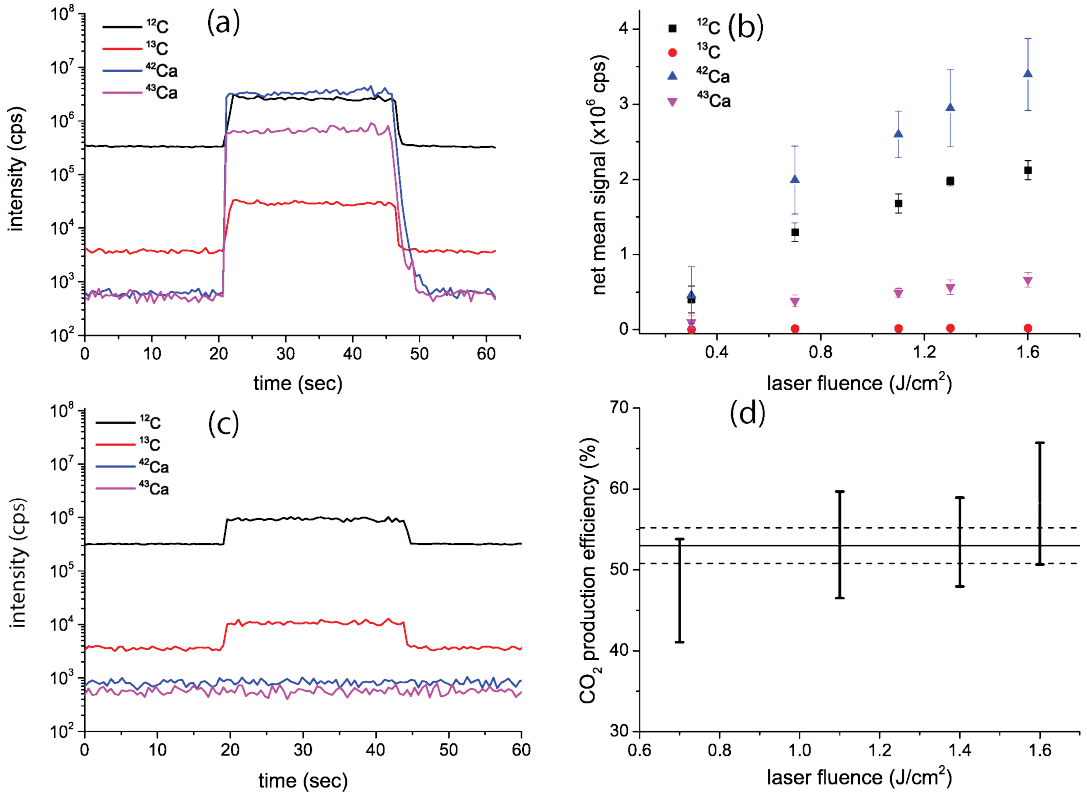

Figure 3.5: (a) Transient signal obtained at a fluence of 1.6 J/cm^2, (b) mean signal intensity plotted against the laser fluence, (c) transient signal obtained for a fluence of 1.6 J/cm^2 with a filter placed between the ablation cell and the ion source, (d) CO_2-production efficiency of the Ex5 laser system as a function of the fluence. The solid line represents the mean value of the four measurements and the dashed lines indicate the standard error.

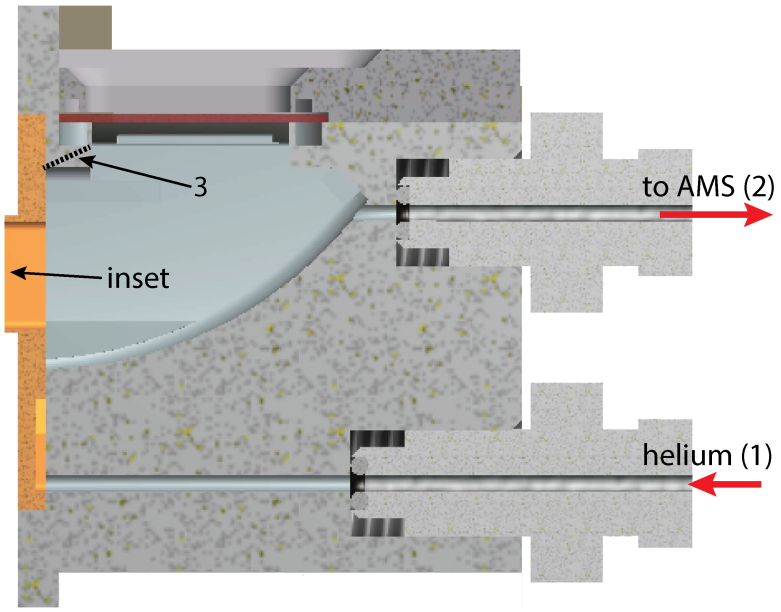

Figure 3.6: The modifications in 'Version 2' of the cell head are: (1) only one helium inlet, (2) modified orientation of the outlet. Support (3) is now straight instead of sloped (black dashed line) in order to construct the cell from one piece. (4) Inserts (orange) can be placed between the sample and the ablation volume.

Second design

First tests that were performed with the LA-AMS setup using 'version 1' of the cell head yielded low ion currents at the order of a few μA, when placing the cell head on a preliminary sample box (compare Figure 3.4 (e)). Most likely this was caused by (i) leakage problems occurring under vacuum at the bonding surface of the cell head and (ii) due to an insufficient CO_2 transport rate from the ablation region into the ion source. A second version of the cell head comprising three major changes was constructed as depicted in Figure 3.6. (a) In order to reduce the air leaks, the modified cell head was built from one part, while the shape of the inner volume was maintained as far as possible. Nevertheless, one simplification, that is expected to have little influence on the gas flow dynamics, was necessary: the support underneath the window had to be straightened as indicated by (3) in Figure 3.6. The dashed line indicates the previous wall. (b) A second change is a gap just above the sample surface that allows to place and exchange inserts as indicated in orange in Figure 3.6. The insert allows to reduce the distance between the cell top part and the sample surface and, hence, to reduce CO_2 losses into the sample chamber (see next section). (c) Furthermore, the two helium inlets were replaced by a single one marked with (1) in Figure 3.6). All experiments below and in the following chapters were conducted using 'version "2' of the cell head.

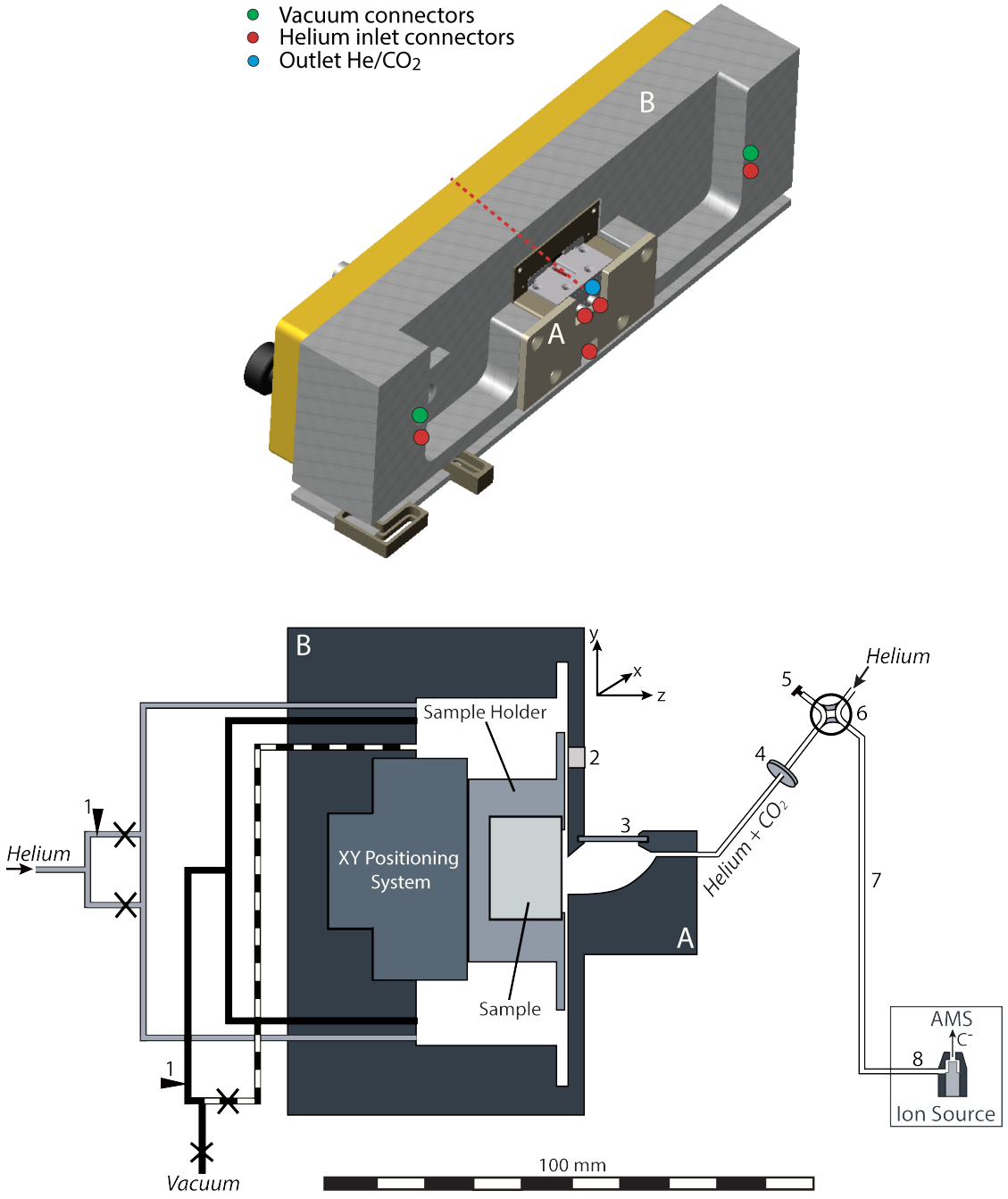

Figure 3.7: Upper part: schematic overview of the complete LA-cell with all connectors (blue, red and green circles). The LA-cell consists of two parts: the 'ablation head' (A) and the 'sample box' (B). The dashed red line indicates the cross-section shown in the lower part: black and dashed lines represent the vacuum system, grey lines the helium connections and white lines the connection between the ablation head and the ion source. Legend: 1. Flow Adjustment, 2. Pressure Sensor, 3. Window, 4. Filter, 5. Cap, 6. Four-Way Valve, 7. LA-AMS Capillary, 8. Capillary in ion source, x Shut-off Valve.

3.2.2 Design of the complete AMS-cell

An overview of the complete LA-cell is depicted in Figure 3.7 where the 'cell head', labelled with (A), is attached to the sample box with four screws and a fixation plate. This allows to easily exchange the cell head and test different designs. The 'sample box' (B) accepts large samples and is equipped with a positioning system that allows to precisely place the sample relative to the laser beam. In addition to the helium connections mounted at the cell 'head' three inlets are installed at the 'sample box' (red circles). Furthermore, two vacuum connections are installed, which are indicated by the green circles. After the cell outlet a combination of two filters (stainless steel replacement frits, Valco, pore size: 0.5 μm, thickness: 0.75 mm and 2 μm, thickness: 1 mm) is inserted to avoid that particulate matter reaches the ion source. After a measurement time of approximately 6 - 8 hours the small filter placed right at the outlet of the LA-cell needs to be exchanged (see Figure 3.8 (a)), because of the reduced conductance of the filter from particles produced during the ablation process. Otherwise, the helium background pressure in the cell has to be increased too much in order to maintain the gas flow rate into the ion source. The second filter placed right before the four way valve is typically exchanged after 24 hours of lasing (compare Figure 3.8 (a)).
To isolate the LA unit and during preconditioning of the AMS gas target, it can be bypassed via the four-way valve. A pressure sensor (Keller, PAA-33X/1bar/80794, 0.001 - 1 bar measurement range) is mounted directly on the cell. For a given CO_2 production rate by LA, the mass transfer from the ablation spot to the ion source is determined by the helium pressure in the LA-cell and the flow resistance of the transfer capillary. The ability of adjusting the pressure inside the LA-cell is crucial for controlling the gas flow rate into the ion source and thus the measurement conditions during LA-AMS. The setup of valves, capillaries and pressure sensor is depicted in Figure 3.7. The black lines represent stainless steel vacuum capillaries with an inner diameter (I.D.) of 2.5 mm. Upstream the pump, the line is split in two, one that is connected to a gas flow controller (Vici, model 100) to adjust a flow rate between 0 - 250 ml/min, and one without flow restriction (dashed line). The gas flow controller allows controlled evacuation and therefore to maintain a specific cell pressure during the measurement. The lines can be individually closed and thus either reduced pumping or no evacuation can be applied during analysis, while full speed pumping is used to flush the cell volume. The helium gas supply (grey lines) is also split into two capillaries, one connected directly to the LA-cell and the other one equipped with a needle valve for adjusting the flow rate into the cell (2-19 ml @ 40 psi N2 inlet, non-lubricated, Vici). After the cell outlet two filters (stainless steel replacement frits, Valco, pore size: 0.5 μm, thickness: 0.75 mm and 2 μm, thickness: 1 mm) are inserted to avoid particulate matter reaching the ion source. To isolate the LA unit and during preconditioning of the AMS gas target, it can be bypassed via the four-way valve. For a given cell pressure, the flow rate into the AMS is determined by the capillary, which is installed between the four-way valve and the ion source ("6" in Figure 3.7).
The cell is designed such, that the front part is permanently fixed to the optical table

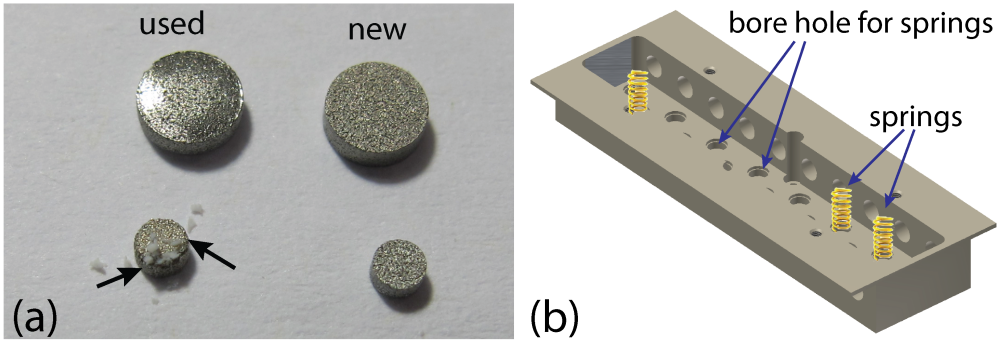

Figure 3.8: (a) Filters before and after usage of approximately 8 hours. Deposits, marked with black arrows, are visible only on the smaller filter. (b) Empty sample holder with three tension springs.

in order to maintain the distance between the lens and the sample. A a second part containing the sample and the positioning system (yellow in Figure 3.7) is designed like a drawer and can be taken out to exchange samples. The sample holder is depicted in Figure 3.8 (b), which accepts samples with maximum dimensions of 150 x 25 x 15 mm^3 (length x width x height).

A set of up to twenty tension springs is mounted in the bottom part of the holder to press the sample specimen against the rim of a 0.5 mm thick steel plate mounted on top. This setup allows an accurate positioning of the sample surface relative to the ablation head. An x-y positioning system (SLC, SmarAct GmbH, Germany) consisting of two linear positioners both equipped with nano-sensors (resolution of approximately 1 nm) and a step width in the sub-nanometer range is placed in the sample box. The linear positioners can reach velocities up to 13 mm/s and have maximum travelling distances of 180 mm and 29 mm. Since the y-positioner is moving vertically, it is equipped with a constant force spring that compensates for a mass of 200 g, which results in an overall allowable load of 550 g for vertical movement. The characteristics of the LA-cell were initially investigated using an ICPMS and the results were compared to data obtained from conventional ablation cells. In the experiments key aspects, such as the cell's washout

time, i.e. how fast the LA produced gas-aerosol mixture is transported into the ion source, were addressed. Furthermore, different He-inlet combinations of the LA-cell were tested. The LA-AMS unit was coupled to an ELAN 6000 Q-ICPMS and the tests were performed using a NIST SRM 610 silicate glass that was placed in the sample holder inside the cell. In order to reduce the distortion of the ICPMS signal due to diffusion processes in the ICP, a stainless steel capillary with an outer diameter of 1.6 mm and an inner diameter of 1 mm was connected to the outlet of the cell and placed into the 6 mm teflon tubing going through the nebulizer into the torch. The carrier gas used was He at a flow rate of 1 liter/min. All settings are summarized in Table 3.2.

The signal rise and washout were compared for two different inlet combinations: first, all inlets were used and second, only the bottom inlets were opened. The results are depicted in Figure 3.9. Part (a) shows the signal rise and drop for ^{23}Na, which was chosen because of its high signal intensity. The blue color represents the signal obtained for the first case (all inlets open), the orange one corresponds to the second case (bottom inlets). In Figure 3.7 (b) the same comparison is made for the mean of the transient signal and for different isotopes as well as for different laser fluences. Each data point was measured three times. No difference can be seen for any isotope between the two inlet combinations.

The washout of the LA-cell was compared to the washout of a common circular LA-cell (Hattendorf, 2002) and the measurement parameters can be found in Table 3.2. The results for ^{42}Ca are summarized in Figure 3.9 (c), where the red curve represents measurements with the conventional LA-cell generated by an ArF excimer laser (GeolasC, 193 nm) and the black curve corresponds to data from the Ex5 and the LA-AMS cell. In both cases the laser was turned off after approximately 100 s of signal collection. The signal of the LA-cell drops from 900,000 cps to 800 cps, i.e. 3 orders of magnitude in 2.5 sec. The signal of the conventional LA-cell drops from 400,000 cps to 800 cps within 30 sec after the laser is switched off. Therefore, the LA-AMS-cell has a washout that is more than 10 times faster than for the conventional cell. This is attributed to the very small ablation volume of 600μL where the laser produced aerosol is confined and which is rapidly washed out when applying a carrier gas flow rate of 1 L/min.

3.3 The MICADAS AMS System

The ultimate measure of the performance of the LA-AMS setup is the C ion current measured with the AMS. Therefore, the characterization of the LA-AMS setup was based on monitoring the ^{12}C ion current ($^{12}C_{LE}$), which is measured right after the LE magnet following the ion source and is an indicator for the overall performance of the ion source and the carbon ion collection efficiency. Before each LA experiment, similar sputtering conditions were established by following a fixed tuning procedure, using the gas interface system (GIS) (Ruff et al., 2007). To ensure proper working conditions of the gas ion source, two to three gas standards (SRMs NIST Ox-I or NIST Ox-II standard) were measured

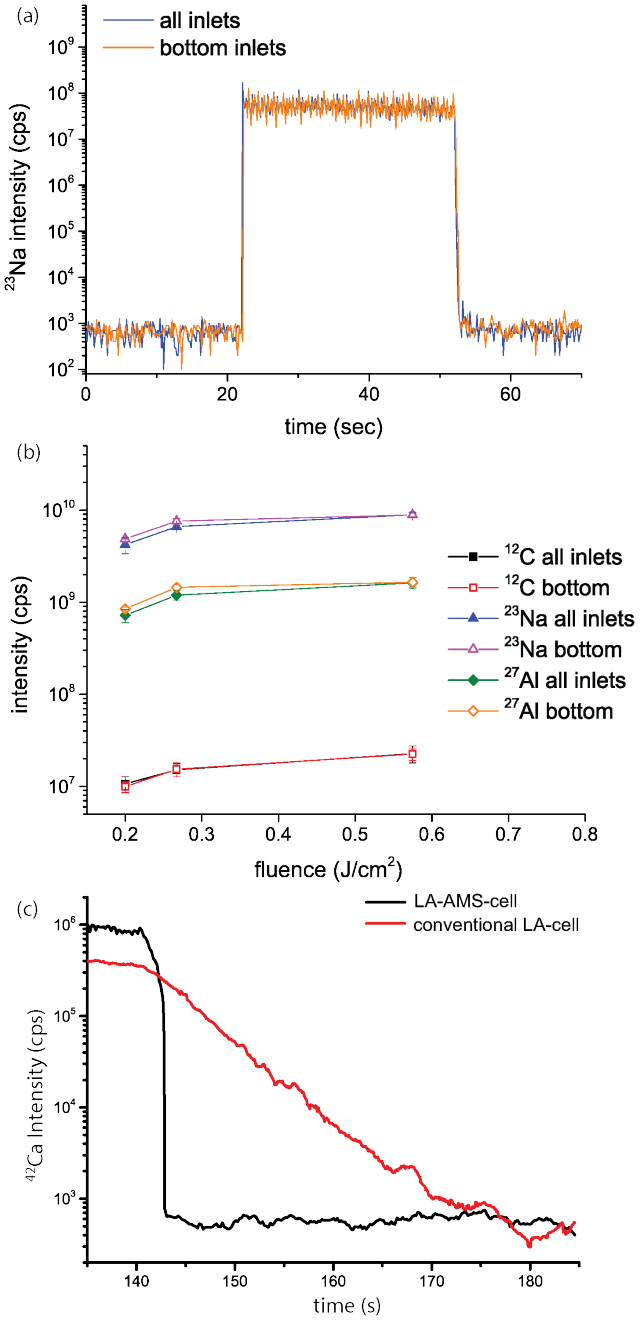

Figure 3.9: Comparison of a different combination of inlets used for the carrier gas. In part (a) signal rise and drop for ^{42}Ca are shown. All settings except of the inlets used were identical. In part (b) the mean values for analogous measurements at different laser energies and for different isotopes are shown. (c) Washout of the AMS cell compared to a conventional LA cell. The washout of the LA cell is at the order of three orders of magnitude in 2.5 s. The LA cell shows a much slower washout at the order of 30 seconds for a similar drop in signal intensity.

before every LA-AMS run. Subsequently, two conventional gas blanks (5 % CO_2 in helium, Messer Schweiz AG, Lenzburg, Switzerland) were analyzed to allow for a correction of the instrumental background. A typical LA-AMS measurement sequence then starts with pre-conditioning of the sputter targets for 30 to 60 sec with the LA-cell bypassed and helium introduced into the ion source to clean the sputter target. Subsequently, the laser is switched on and the produced CO_2 is transported with helium from the LA-cell into the ion source where negative C ions are produced and finally the ^{12}C, ^{13}C and ^{14}C signals are collected. For all measurements the integration time for ^{14}C /^{12}C data was set to 10 seconds. The period of data acquisition is limited by the lifetime of the gas targets, which depends on the Cs-density and the magnitude of the ion current and is in our case typically 10 - 20 minutes.

4 Samples and sample preparation

Laser Ablation - AMS allows to analyze the ^{14}C-content of carbonate samples with very little sample preparation. Here, the few steps necessary before measuring samples with LA-AMS, are described and an overview of the materials and samples used for LA-AMS analysis is given.

4.1 Sample preparation

Currently, for LA-AMS analysis all components (organic and inorganic) present in the sample are ablated and subsequently analyzed. Future tests will show whether the pre-treatment of samples in order to remove the organic components (leaching) should be implemented into the sample preparation procedure. This could be especially of importance for samples with high organic contents, such as corals and shells.
Sample preparation basically involves getting samples into the right dimensions for the sample holder. Prior to analysis, the samples are fixed in the sample holder by placing them on top of up to twenty tension springs and retaining them with the upper steel plate, which is mounted with twelve screws (Figure 4.1). Because plane sample surfaces are necessary for LA, the samples need to be smoothed and - if too large - cut to the dimensions of the sample holder. Several samples can be placed next to each other, but gaps between different pieces need to be avoided in order to create an even surface at the ablation region. For the same reason, samples that are smaller than the sample holder need to be embedded in epoxy resin. The advantages of epoxy are its comparably simple handling and its low cost. The disadvantage is, that epoxy resin is a potential source of contamination with 'dead' (devoid of ^{14}C) C. An overview of the embedding procedure is depicted in the upper part of Figure 4.2. An aluminum mold with inner dimensions of 75 x 25 x 15 mm^3 is lubricated with silicon grease (GE Bayer Silicones, Baysilone-Paste, hochviskos), which allows quick removal of the dried and embedded samples. In order to avoid contamination from the epoxy intruding porous material or covering the sample's surface, the samples are tightly wrapped in polyethylene foil and placed into the mold. The epoxy preparation (Epoxi Fix Kit, Struers) is then poured over the sample and allowed to cure for 24 hours. Finally, the sample is removed from the form, the epoxy is cut into the desired dimensions and the wrapping is taken off using a pair of tweezers. Problems that occurred with this embedding procedure where: (i) the wrapping film could not entirely be removed from the sample (epoxy had penetrated between the wrapping film and the tape). (ii) Especially when embedding long samples (i.e. several cm) it is important that

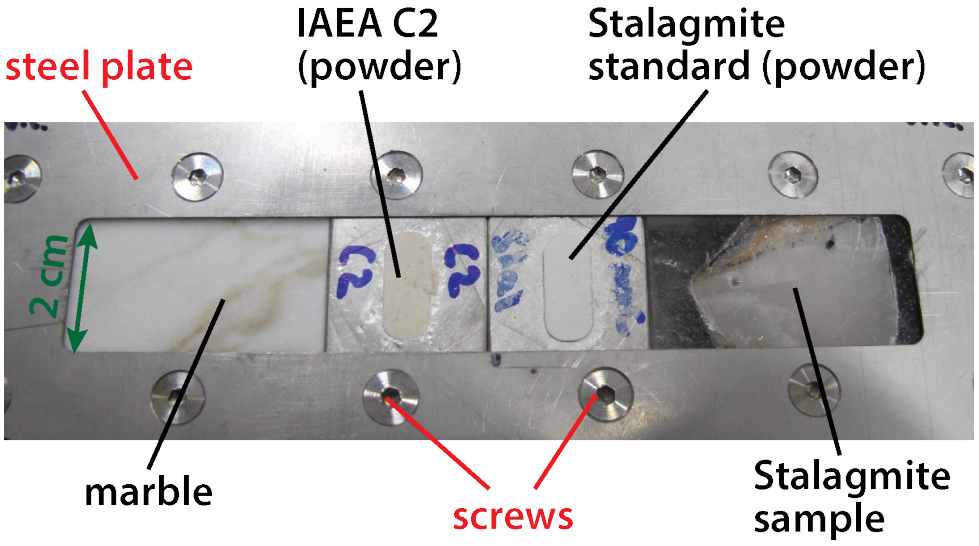

Figure 4.1: Sample holder with the steel plate retaining the samples in the holder fixed by 12 screws. Different sample materials are depicted (from left to right): marble, pressed IAEA C2 powder and pressed in-house stalagmite standard powder, natural stalagmite sample embedded in epoxy.

the epoxy layer is thick enough to cover the backside of the sample. Otherwise the sample can detach from the epoxy or break. If the backside is also needed for analysis, special care needs to be taken when releasing the sample from the mold. Gypsum was tested as another candidate for embedding samples. Since it is C-free, no wrapping film is necessary and the handling and costs are comparable to that of epoxy resin. High molecular ion abundance was observed during the AMS measurement when using gypsum for embedding. This is most likely caused by the crystal water in the material, which is released together with the CO_2. Possibly, the background could be reduced by longer ($> 24\,h$) drying or by using an oven. Standard and reference materials used for LA-AMS are available mainly as powders. Therefore, samples of carbonate powder were pressed using a hydraulic press (Specac, Portmann instruments AG, Biel-Benken, Switzerland) with a pressing force of 15 tons into molds made of stainless steel (width: 5 mm, length: 18.5 mm, depth: 1 mm) and placed in the sample holder for analysis. In Figure 4.1 the sample holder with different samples is shown.

4.2 Calibration standards and reference materials

An overview of the standard materials used for the characterization of the LA-AMS setup and for the analysis of natural samples is given in Table 4.1. For the instrumental characterization, a surface polished, rectangular piece of marble (Natursteine Wüst, Zurich, Switzerland) was fit tightly into the sample holder to ensure comparable gas flow conditions

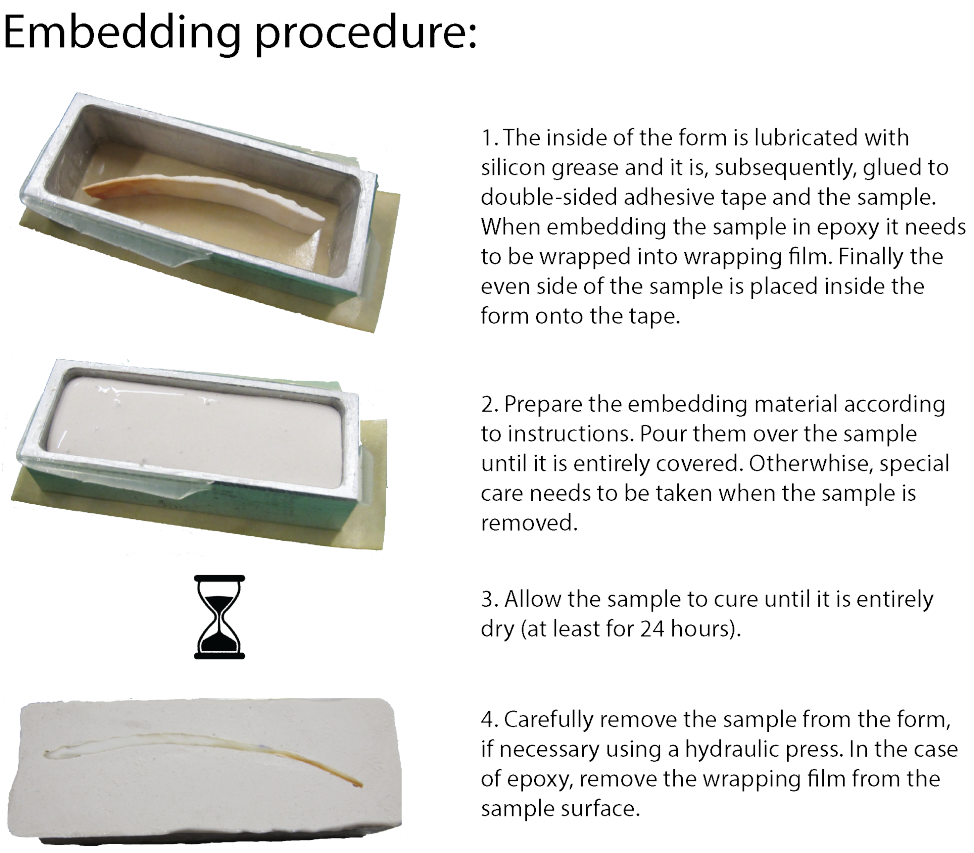

Figure 4.2: Overview of the embedding procedure for LA-AMS samples. After embedding, the samples are cut to the desired size and placed in the sample holder which is shown in the lower part of the Figure. The picture shows a variety of samples: a solid piece of marble, two pressed standards and a natural stalagmite sample embedded in epoxy resin.

at every position on the sample. This sample is considered as ^{14}C blank. A certified carbonate standard material used with LA-AMS is the IAEA C2 powdered Travertine standard with a nominal $F^{14}C$ value of 0.4114 ± 0.0003 (Rozanski et al., 1992). A coral powder standard (CSTD) with a nominal value of 0.9445 ± 0.0018 (n = 262) (Gao et al., 2014) and stalagmite powder are used as standards. The stalagmite standard was produced in-house by powdering a piece of a nearly modern stalagmite in a ceramic mortar and homogenizing it. Five subsamples of the stalagmite powder were analyzed by conventional gas measurements yielding a $F^{14}C$ of 0.871 ± 0.007.

4.3 Natural samples

The following natural samples, including terrestrial as well as marine carbonates, were analyzed by LA-AMS:

(i) **Stalagmite ER-77**
Stalagmite ER-77 is a calcite speleothem from Grotta di Ernesto cave located in Italy, which has been actively growing with a mean growth rate of approximately 120 μm/a until the year of its removal in 1992 (Frisia et al., 2003). Data from conventional measurements are available (Fohlmeister et al., 2011) revealing a bomb peak within the topmost 4 mm.

(ii) **Stalagmite BU-4**
The BU-4 stalagmite was sampled from an active dripping site from Bunker Cave situated in western Germany (Fohlmeister et al., 2012). It consists of calcite and exhibits a much smaller growth rate of 30-50 μm/a in comparison to stalagmite ER-77. ^{14}C measurements have been performed at the MICADAS at ETH Zurich on three conventionally drilled and subsequently graphitized samples (Fohlmeister et al., 2012). For the topmost sample a spatial resolution of about 0.1 mm was achieved, whereas for the other samples the resolution is 1 mm and the measurement precision is on the order of 0.3 %. The signature of the bomb tests was found in this data with a F^{14}C difference of more than 0.1. The section analyzed with LA-AMS had previously been embedded in epoxy resin for trace element analysis.

(iii) **Stalagmite SOP-20**
SOP-20 is a stalagmite sample from Okhotnichya cave situated approximately 7 km from Lake Baikal. It grew actively with near-constant and very low growth rates of

Table 4.1: Overview of the different standard and blank materials used for LA-AMS

Sample label	Type of sample	Material	Certified/ expected F^{14}C
Marble	blank	marble	< 0.001
Blank gas	blank	5 % CO_2 in He	< 0.001
NIST Ox I	reference Standard	oxalic acid	1.0398
NIST Ox II	reference Standard (Stuiver, 1983)	oxalic acid	1.3407 ± 0.0005
IAEA C2	reference standard (Rozanski et al., 1992)	carbonate powder	0.4114 ± 0.0003
CSTD	in-house coral standard (Gao et al., 2014)	carbonate powder	0.9445 ± 0.0018
Stalagmite standard	in-house stalagmite standard *(LIP, ETH Zurich, Switzerland)*	carbonate powder	0.871 ± 0.007

3-15 μm/a over the entire Holocene until it was collected. This has been verified by U-series ages measured along the growth axis of the stalagmite (Vaks et al., 2013). The stalagmite features a hiatus (growth interruption) that separates the Marine Isotope Stage 11 from the Holocene. The hiatus is confirmed by two U-series dates, confining the stop between the end of the marine isotope stage (MIS) 11 (377 $\pm$ 7 ka BP) and the Holocene (8.711 $\pm$ 0.012 ka BP). The three sections of SOP-20 analyzed by AMS were embedded in epoxy resin prior to analysis.

(iv) **Stalagmite SPA-127**
The Spannagel cave (Tirol, Austria) is situated in a high alpine region with sparse vegetation and only a thin layer of soil above the cave (Vollweiler et al., 2006). The stalagmites there grow only partly due to host-rock dissolution from vegetation-derived carbonic acid in the seepage, which normally is the case (Dreybrodt, 1980). It is hypothesized that the oxidation of sulfides contributes considerably to the dissolution of host rock carbonates and, hence, to the growth of stalagmites (Holzkamper et al., 2005). As a consequence, the stable C isotope signal of the Spannagel stalagmites is thought not to primary represent soil processes as common in other cave locations. The SPA-127 is a stalagmite from Spannagel cave that grew in the Holocene between 2500 and 8500 a BP as confirmed by U/Th-ages and the average growth rate is on the order of 25 μm/a (Vollweiler, 2010; Fohlmeister et al., 2013). The unpublished δ^{13}C-record from this stalagmite exhibits exceptionally large and fast variations from 1 to -8 ‰. Even though, there is no final explanation for these variations, it is suspected that they are a consequence of rapid changes between the usual way of carbonate dissolution due to carbonic acid and the unusual sulfide-oxidation process suspected to occur here.

(v) **Coral DR241300**
The calcareous material of bamboo corals is formed axially with growth rates between 7-14 mm/a and radially with growth rates between 0.05 and 0.1 mm/a (Andrews et al., 2009). The skeletons are characterized by alternating calcitic and organic layers which results in a banded structure (Watling et al., 2011; Noe and Dullo, 2006). Conventional graphite measurements on coral DR241300 yielded a value of 0.330 $\pm$ 0.001 (Klaus-Tschira-Archäometrie-Zentrum, Mannheim, Germany) for a sample covering the entire cross-section of the sample.

(vi) **Coral 36252**
Coral 36252 is a bamboo coral from the western North Atlantic, which was collected by dredge in 2002 at 39.883 N, 67.433 W near Bear Seamount at a depth between 1195 and 1402 m (Farmer et al., 2015). The radial growth rate was estimated to be between 50-78 μm of radial growth per year (J. Farmer, personal communication). Conventional radiocarbon measurements have been performed by drilling with a spatial resolution of approximately 1 mm, except for the three topmost samples where the spatial resolution is 0.5 mm. The onset of the bomb peak was found at the outer edge of the coral. The coral sample was embedded in epoxy resin prior to LA-AMS analysis.

(vii) **Shell sample: Arctica islandica**
The shell of Arctica islandica investigated here, was found at the beach of Fur, Denmark, in 1987. The shell skeletons consist of aragonite (Karney et al., 2012) with highly variable growth rates ranging from 0.2 to 1.0 mm/yr in the North Sea (Witbaard et al., 1999), that depend on environmental factors like temperature and food supply (Witbaard et al., 1997, 1999). Due to its good condition it was assumed, that the shell had been alive until shortly before it was found. From its size it was estimated that it had lived long enough to contain pre-bomb ^{14}C. Neither conventional ^{14}C measurements are available, nor other proxies that could provide information about the age of the shell. The sample was cut into slices, the surface of one piece was polished and subsequently embedded in gypsum.

(viii) **Shell sample: pearl oyster**
The black-lipped pearl oyster (Pinctada margaritifera) fishery at Pearl and Hermes Reef (Northwestern Hawaiian Islands) was closed in 1930 due to severe depletion (Galtsoff, 1933; Moffitt, 1994). Recent surveys indicate that the population has not recovered despite protection (Keenan et al., 2006). Estimates of age are 40-70 years for some of the largest shells using growth increment structure visible on the external surface (A.H. Andrews, NOAA fisheries, personal observation). However, these age estimates are not validated. Because of the potential lifespan of the black-lipped pearl oyster, bomb ^{14}C dating could provide validated estimates of age. The shell used in this study was collected in 1994. To assess a continuous axis of growth, the shell was sectioned longitudinally to reveal successive inner growth layers (oldest to youngest). The two sections were polished and embedded in epoxy resin prior to LA-AMS analysis.

(ix) **Otolith RS-07**
A large uncertainty of the longevity of the commercially and recreationally caught red snapper (Lutjanus campechanus) makes management approaches of their population difficult. Bomb ^{14}C incorporated into otoliths of sufficiently old fish has been used to validate ages (Baker and Wilson, 2001). LA-AMS has the potential for rapidly determining the age of red snappers via bomb-^{14}C in otoliths. The RS-07 sample was taken from a red snapper, which was collected in 2002 with a projected birth year earlier than 1958. Hence, it is expected that the sample comprises pre-bomb ^{14}C levels, the rise of the bomb peak and the post-bomb decline. For LA-AMS analysis a thin-section of the otolith was glued with epoxy resin onto a microscope slide.

5 Characterization of the setup*

The following section is divided into two main parts: part one covers the instrumental characterization of the LA-AMS setup including the comparison of different LA-cell insets, the ablation rate as well as sensitivity and signal stability. In the second part analytical aspects such as the blank level, washout behavior of the LA-cell, cross-contamination and the reproducibility of reference materials are addressed. All measurement settings for the following experiments are listed in Table 5.1.

5.1 Instrumental characterization

5.1.1 Comparison of inserts

The main objective of the insert, which is placed between the cell head and the sample surfacec, is to minimize the gap between the sample box and the ablation head, while at the same time the mobility of the positioning system needs to be maintained. Inserts for the LA-cell of different design and fabricated from different materials are compared with regard to short washout times and high ion currents.

Insert 1

A scheme of 'Insert 1' is shown in the left part of Figure 5.1. The laser beam is focused through a gap in the insert with dimensions of 2 x 6 mm^2 onto the sample surface. On the upper side of the insert, the helium stream coming from the He-inlet (right side of Figure 5.1) is separated via a Y-shaped slot into two sub-streams, which are fed through two orifices to the side towards the sample of the insert. Here, the He is flushed around a protruding rectangle to (i) keep CO_2 in the ablation head and (ii) to inhibit carry-over by preventing CO_2 that escaped from the ablation spot into the sample box from flowing back into the cell head. The distance between the insert and the upper surface of the sample (Δx) is a crucial factor: the smaller Δx, the larger is the gas flow resistance and the higher the CO_2 transport efficiency. However, when Δx is too small the positioning system is not capable to move samples, because at transitions between two samples and at regions where sample surfaces are not entirely even, the sample gets caught at the insert. With 'Insert 1' no ion currents were yielded, even when the laser was operated at maximum energy and

*Parts of this chapter are submitted to publication (Welte et al., submitted)

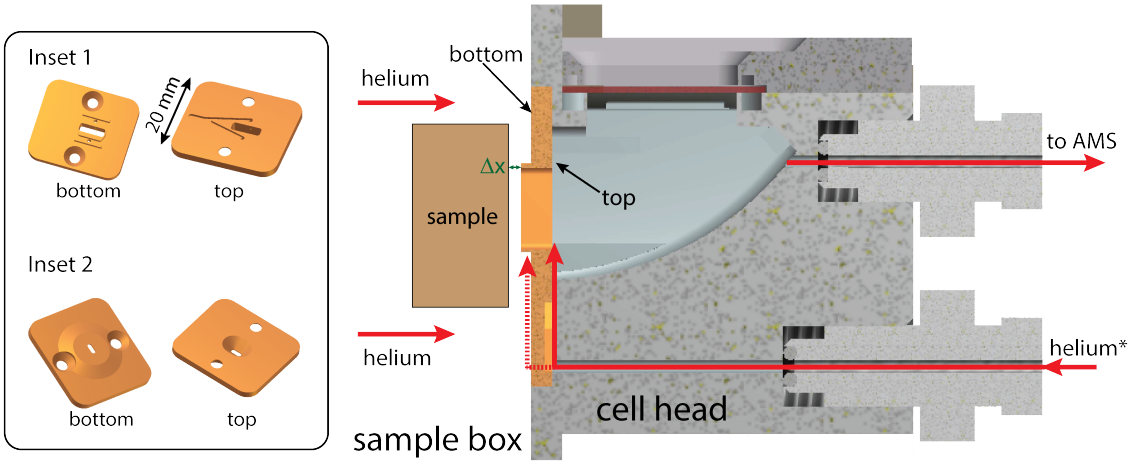

Figure 5.1: Upper and lower side of 'Insert 1' and 'Insert 2'. LA-cell head with 'insert 1'. Red arrows represent gas flows (details can be found in the text). The gap represented by Δx is at the order of 1/10 mm.

repetition rate. It is assumed, that insufficient sealing between the top side of the insert and the cell head causes parts of the incoming He to directly flow into the cell head and push most of the CO_2 into the sample holder (see right side of Figure 5.1). Based on these results, measurements were conducted without using He-inlet* and ion currents of less than 5 μA were yielded, which is more than a factor of three lower than currents normally reached. It is likely that the protruding rectangle is not creating a sufficiently high flow resistance and most of the CO_2 is lost into the sample box.

Insert 2

A second insert ('Insert 2') with a larger and circular protruding surface was constructed and is depicted in the lower left picture of Figure 5.1. For simplicity, the helium inlet* at the cell head was not used in combination with this insert. The measures and the cross section through the insert are given in Figure 5.2 (a) and a picture of the insert is shown in part (b). Two versions of the insert, with a difference in thicknesses of 0.1 mm, were constructed. With the thicker version an 'ideal' sample with a smooth and even surface could not be properly moved by the positioning system. Consequently, only the thinner model, providing a gap at the order of 1/10 mm, was employed for LA-AMS measurements. Ion currents yielded with 'insert 2' were comparable to those reached with normal gas measurements, however, still up to 60 % of the produced CO_2 is lost into the sample box (compare Section 5.1.4). Routine operation showed that the amount of gas loss varies from

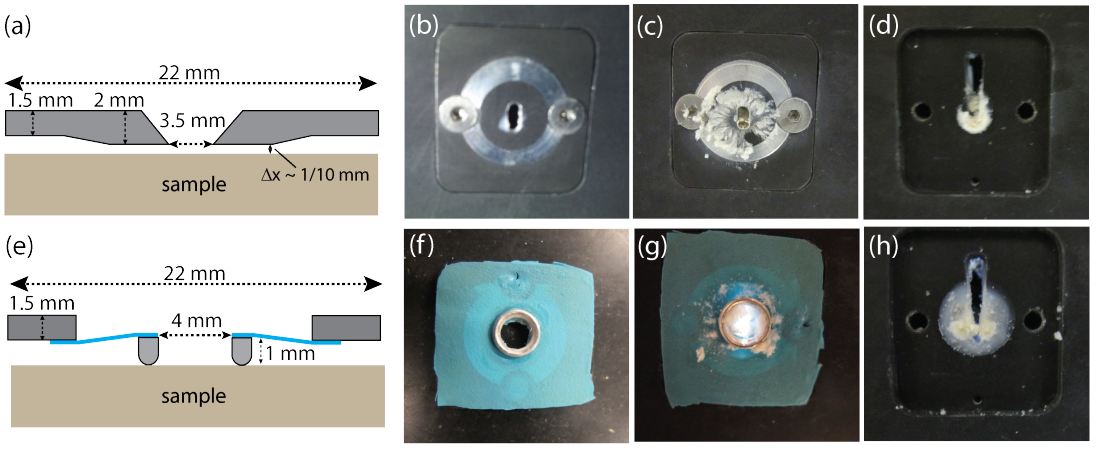

Figure 5.2: (a) Cross-section through a schematic drawing of 'insert 2'. (b) 'Insert 2' installed in the LA-cell before LA-AMS measurements. (c) Deposits on 'insert 2' after approximately 4 hours of measurement. (d) Deposits in the cell head (the insert is removed) after ablating for 4 hours using 'insert 2'. (e) Cross-section through a schematic drawing of the 'membrane insert'. The blue parts indicate the membrane. (f) Picture of the 'membrane insert' installed in the LA-cell. (g) Deposits on the 'membrane insert' after approximately 4 hours of LA-AMS measurements. (h) Deposits in the cell head after 4 hours of measurement using the membrane insert (the insert is removed in this picture).

day to day, which is probably caused by variations of the gap size of several 1/100 mm (Δx in Figure 5.1).

Membrane insert

A better sealing of the ablation volume relative to the sample box is expected to results in a higher CO_2 transport rate and, consequently in higher ion currents. The 'membrane insert' consists of a steel ring with an I.D. of 4 mm and is thick enough (1 mm) to ensure that it is in contact with the sample surface. Friction on the sample surface is reduced by polishing and rounding the contact surface of the ring (Figure 5.2 (e) and (f)). It is glued to a flexible nitrile butadiene rubber (blue in 5.2 (e), which is clamped onto an anodized aluminum frame. This makes the steel ring flexible, so that it can easily be moved over small unevennesses caused by the contact area of neighboring sample or roughnesses on the sample surfaces.

To ensure equal gas flow all over the sample, a polished marble sample precisely fitting into the sample holder was used for the following measurements. Comparable conditions of the

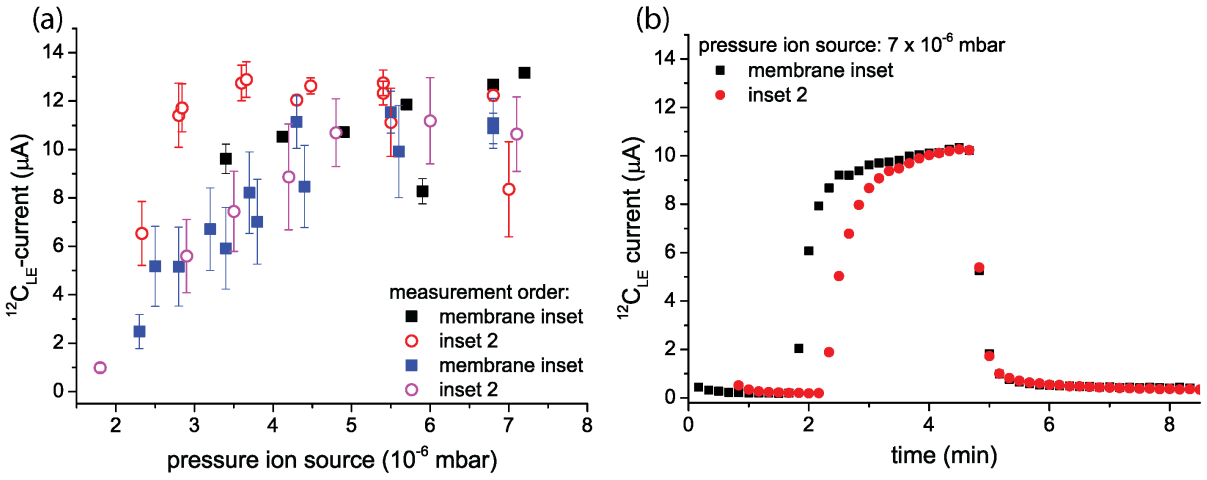

Figure 5.3: (a) Ion current plotted against the ion source pressure for the two inserts. For both inserts two sequences from low to high pressures were conducted. Highest ion currents are yielded for the first sequence using 'insert 2'. (b) Transient signals for the two inserts.

ion source were ensured by performing all measurements on the same day and alternating 'insert 2' and 'membrane insert'. For each insert, a measurement sequence with increasing gas flow rates, which is directly proportional to the pressure in the ion source (P_S), was performed by adjusting the helium background pressure between 700 and 1200 mbar in the LA-cell. For the first measurement sequence using the 'membrane insert' (black squares in Figure 5.2 (a)), the signal for each P_S was collected for approximately 1 minute and, subsequently, the flow rate was increased. The entire sequence was conducted on the same sputter target. For the other sequences (red open circles, blue solid squares, purple open circles), the signal for each P_S was collected on a single sputter target each for 3 - 4 minutes. The mean $^{12}C_{LE}$current for each insert and each P_S was calculated. The error bars represent the standard deviation of the current and, thus, display the signal stability of the single measurements. The ion currents yielded for both measurement sequences with the 'membrane insert' (black and blue squares) are lower than the first sequence with 'insert 2' (open red circles) and in the same order as the second sequence with 'insert 2' (open pink circles). Most likely, gradual clogging of the outlet by particles caused the decrease in ion currents for all measurements conducted after the first sequence (open red circles). This assumption is confirmed by the shift of the maximum current towards higher gas flow rates (i.e. higher P_S) for the second measurement represented by blue squares (Section 5.1.3). The ion currents yielded with the 'membrane insert' where in the same order as the ion currents achieved with 'insert 2'. This is also shown in Figure 5.2 (b), where the transient signals for the two inserts are directly compared. In both cases the P_S was set to 7×10^{-6} mbar and the observed washout behavior is very similar. It is concluded that the sealing effect for CO_2 gas of the two inserts is nearly the same and could not be improved with the 'membrane insert'.

The deposits found for the two inserts at the cell head and on the bottom side of the insert

are depicted in Figure 5.2 (c)-(d) and (g)-(h). In the case of 'insert 2', particles formed during the LA process deposit rather on the bottom side of the insert, i.e. between insert and sample (subfigure (c)) and to a lesser extent in the cell head (subfigure (d)). In the case of the 'membrane insert' the greater amount of particles is found in the cell head and fewer particles deposit on the bottom side of the insert. In contrast to a sealing effect for the LA-produced CO_2, a sealing effect of the 'membrane insert' for particles is observed. This effect is likely to increase cross-contamination when working with 'membrane insert', as particles deposited in the cell head are constantly exposed to the incident laser beam and, therefore, are prone to re-ablation.

Silicon insert

A fourth version of the insert has been designed using silicon as the sealing material. For this, negative-forms made from steel for inserts of different thicknesses ('silicon insert 1': 1.1 mm and 'silicon insert 2': 1.2 mm) were prepared. The two-part liquid silicon rubber (MED-4905, Nusil Silicone Technology, Carpinteria, USA) was mixed in a 1:1 ratio, filled into the forms, followed by a vacuum deaeration procedure and curing at room temperature for three days. Holes in the middle of the silicon form as well at the two outer edges were punched out, in order to create openings for the laser beam and for mounting the insert. The silicon part was then placed onto an anodized aluminum frame as shown Figure 5.4 (a) and fixed with two screws to the LA-cell. First tests of the silicon inserts of different thicknesses and the positioning system revealed that with 'silicon insert 2' a sample with a smooth surface could not be moved relative to the laser beam, because the friction between the insert and the sample surface was too high. Therefore, this insert was coated with a two-component low coefficient of friction silicone dispersion (MED-6670, Nusil Silicone Technology, Carpinteria, USA), which lowered the friction sufficiently.

The two silicon inserts were compared to 'insert 2' with regard to the ion currents that were yielded (i) on an 'ideal' (with respect to surface smoothness) marble sample and (ii) on a natural stalagmite sample. First, a scan on the marble sample was conducted for each insert. The signal was collected for 3 - 8 minutes and the average $^{12}C_{LE}$current was calculated. Second, multiple scans were performed on a natural stalagmite sample with 'insert 2' and 'silicon insert 1' while the measurement settings were kept constant. The results are shown in Figure 5.4 (b). Solid symbols represent the measurements on the marble sample, where the $^{12}C_{LE}$is highest for 'insert 2' and lowest for 'silicon insert 2'. Also for the measurements on the stalagmite sample the $^{12}C_{LE}$is highest for 'insert 2', but generally the currents are lower than for the marble sample. Most likely the natural stalagmite sample is more porous than marble. The signal intensities for both silicon inserts on both samples are lower than for 'insert 2'. The silicon inserts are more prone to catching small roughnesses on the sample surface than the aluminum inserts. Their thickness - on a level of 1/100 of mm - needs to be smaller and the gap to the sample box is therefore larger.

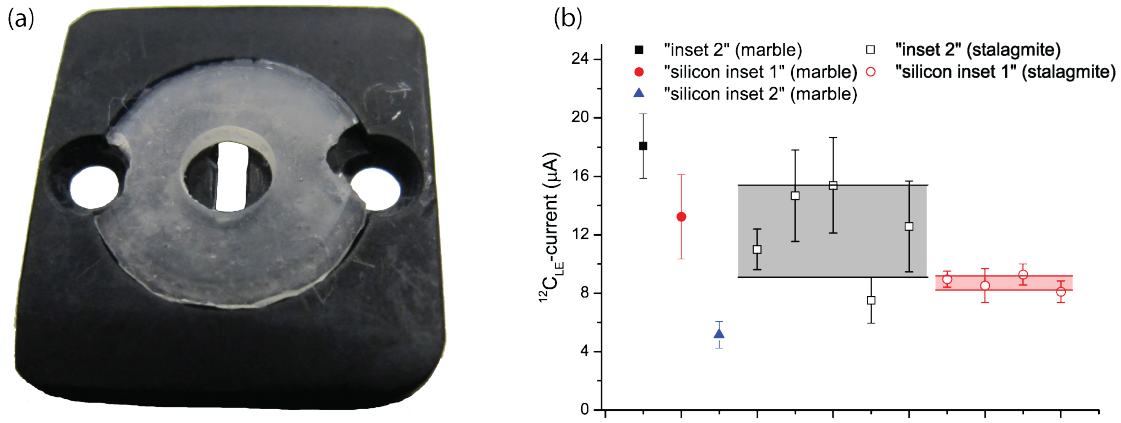

Figure 5.4: (a) The silicon form is fixed to the aluminum frame via the two openings at the side by two screws that are simultaneously used to mount the insert to the LA-cell. The laser passes through a hole in the middle of the silicon form that overlaps with a gap in the aluminum frame. (b) $^{12}C_{LE}$current yielded for a marble (solid symbols) and a stalagmite sample (open symbols) using the two silicon inserts and 'insert 2'. The error bars represent the standard deviation of the ion current corresponding to each measurement and are thus a measure for the stability. Solid lines represent one standard deviation for the replicates.

Final considerations

A major advantage of the LA-cell head is that inserts can easily be exchanged. This allows to compare different 'cell'-geometries without having to re-design the entire cell. Four inserts have been constructed and compared in order to optimize the cell washout and the CO_2 transportation rate: 'insert 1' and 'insert 2' made of aluminum with different flow resistances; 'membrane insert', which comprises a stainless steel ring attached to a flexible membrane and 'silicon insert 1 and 2', which are made from a low friction elastomer especially fabricated for sliding across surfaces with minimal friction. Tests on marble and natural samples showed, that comparably high signal intensities of up to 13 μA were achieved with 'insert 2' and 'membrane insert'. However, in the case of 'membrane insert' particles were deposited mainly in the LA-cell head, which is thought to enhance cross-contamination. 'Insert 1' yielded lowest ion currents of only 5μA, most likely caused by its geometry which poses a low flow resistance to the LA-produced CO_2. Signal intensities obtained for 'silicon insert' were lower than those obtained with 'insert 2' on marble and on a stalagmite sample. On an absolute scale ion currents ranged from 8 to 13 μA and, hence, are high enough for ^{14}C analysis in all cases. Since neither with 'membrane insert' nor with 'silicon insert' an improvement with regard to the CO_2 transport efficiency could be achieved, due to its simplicity and comparably good performance 'insert 2' is employed for all measurements presented in this work.

Table 5.1: Typical laser settings during LA-AMS measurements.

	Physical Quantitiy	**Setting**	**Unit**
Laser parameters	Repetition rate	200 - 250	Hz
	Laser energy on sample (per pulse)	0.8 - 2	mJ
	Spot size	680 x 110	μm^2
	Fluence on sample (per pulse)	1 - 2.5	J/cm^2
	Irradiance on sample (per pulse)	0.14 - 0.36	GW/cm^2
	Scan velocity	10 - 20	$\mu m/s$
Gas flow parameters	Capillary 1 (I.D.; length)	150; 100	μm; cm
	Capillary 2 (per pulse)(I.D.; length)	250; (100 + 64)	μm; cm
	He-background pressure in LA-cell	600 -1200	mbar

5.1.2 Ablation rate

The ablation rate, i.e. the mass of carbonate removed per laser pulse, depends on the laser fluence and on the density of the sample material. The ablation rate of the Ex5 laser system was determined on a marble sample using a repetition rate of 200 Hz, a fluence of of 1.8 J/cm^2, a scan velocity of 10 μm/s and a spot size of 110 x 680 μm^2. The mass of the sample was determined before and after ablation by weighing (Mettler AE 163, Mettler-Toledo, Greifensee, Switzerland). Five replicates were carried out and the mean ablation rate, determined from the mass difference and laser pulses applied, was (8.1 ± 0.4) ng $CaCO_3$ per pulse, corresponding to (97 ± 5) μg $CaCO_3$/min. Attempts have been made to determine the ablation rate by measuring the ablated volume using a microscope (Olympus BX-51, Olympus Schweiz AG, Volketswil, Switzerland). The results were rejected since they were not reproducible within a relative uncertainty of 20 %.

5.1.3 Sensitivity and signal stability

Determining the total gas flow rate

First LA-AMS measurements showed that the LA-cell requires a significantly larger He carrier gas flow for an efficient transport of the CO_2 to the gas ion source than conventional gas measurements. The total gas flow of the LA-AMS setup was assessed by calibrating the ion source pressure to the gas flow rate using a mass flow controller (MCC-2SCCM-TFT,

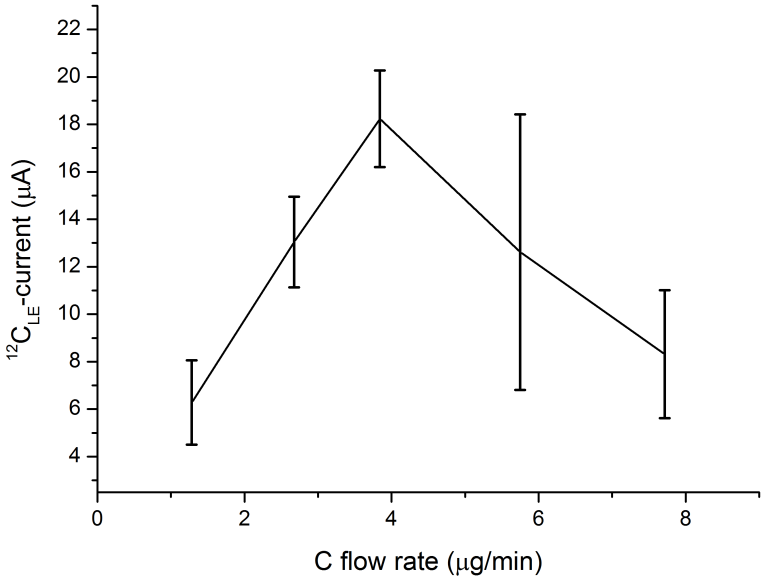

Figure 5.5: Ion current as a function of the C flow rate. The error bars indicate the range of the ion current and, thus, represents the signal stability. The pressure in the cell was kept constant resulting in a gas flow rate of 1.5 mL/min. The maximum ion current is found at a C flow of approximately 4 μg/min.

Alicat Scientific, Tucson, USA) with a working range from 0.025 to 2 std mL/min. The helium flow rate was varied between 1 - 2 mL/min STP corresponding to a pressure in the ion source ranging from 3.3×10^{-6} to 3.9×10^{-6} mbar. The sensitivity offset of the pressure sensor in the ion source for a mixture of 0.7 % CO_2 in helium (typical order found for LA-AMS) in comparison to pure helium was found to be on the order of + 10 %. Since the ion source pressure observed during LA-AMS measurements ranges from 2.7×10^{-6} mbar to 3.6×10^{-6} mbar the gas flow rate is determined to be between 1.1 mL/min and 1.7 mL/min.

Determining the C flow rate

The C mass flow rate from the LA-cell into the ion source was estimated from the CO_2 concentration and the total gas flow rate. Different CO_2 concentrations in helium were prepared from a 5 % CO_2 in helium mixture (Messer Schweiz AG, Lenzburg, Switzerland) and filled to a total pressure of 1200 mbar in the LA-cell. These mixtures were introduced into the gas ion source at a gas flow rate of 1.5 mL/min and the signal was collected for 5 minutes. For each measurement the average ion current collected during the last 50 s of the five minutes was evaluated. The results are depicted in Figure 5.5 where the

$^{12}C_{LE}$-current is plotted against the C flow rate. The error bars represent the variability of the ion current and are an indication for the stability of the measurement. Between 1 and 4 μg C/min the ion current increases with increasing C flow rate, reaching a maximum at approximately 4 μg/min. In this regime the efficiency is constant. For even higher C flow rates the ion current decreases with increasing C flow rate and also the efficiency drops. The relation between the ion current and the C flow rate is a complex process that has previously been observed and described by Fahrni et al. (2013).
During optimized LA-AMS measurements typical $^{12}C_{LE}$-currents between 10 and 20 μA have been observed. A decrease in the laser repetition rate resulted in nearly every case in a decrease of the ion current. Thus, based on the calibration curve (Figure 5.5), the CO_2 concentration in the He gas supplied by the LA-system can be estimated to be in a range of 2 to 4 μg/min. Fahrni et al. (2013) showed thatthe optimum C flow for conventional gas measurements is between 2 and 3 μg/min, which is of similar magnitude as for the LA-AMS setup, even though the total gas flow rate applied during LA-AMS measurements is one order of magnitude higher.
Routine gas measurements have shown that not only the magnitude of the ion current but also the stability of the gas measurements depend on the C flow. Two different transient ion signals observed during LA-AMS are shown in Figure 5.6. The behavior for an optimum C flow range is depicted in panel (a): a quick rise of the ^{12}C-current occurs when the CO_2 reaches the ion source, followed by a moderate increase of the signal intensity. If the C-flow is below the optimum, much lower initial ion currents are obtained that subsequently increase steeply as displayed in panel (b). A third case that has rarely been observed during LA-AMS is a C flow rate above the optimum, i.e. larger than 4 μg/min. This results in a first quick and very steep rise of the current followed by a signal drop. The different transient behaviors of the ion current are so far not well understood and are most likely caused by complex processes (i) during the extraction of CO_2 from the LA site and (ii) those occurring in the ion source. Possible explanations for the different C flow rates obtained during LA-AMS, even when laser and gas flow settings were kept constant, are discussed below (Section 5.1.4).

Comparison of capillaries

The I.D. and length of the connecting capillary ("6" in Figure 3.7) and the pressure in the LA-cell determine the gas flow rate into the ion source. If a larger I.D. and equal length are used, the pressure in the cell has to be lowered to maintain the gas flow rate. Two capillaries of different I.D. and length were alternatingly installed between the LA-cell and the ion source. For each capillary the helium pressure in the LA-cell was varied while the laser parameters were kept constant (compare Table 5.1). The resulting ion currents were collected for approximately 3 minutes during ablation of the marble sample. Maximum ion currents for both capillaries were on the order of 14 μA, but required different LA-cell pressures as shown in Figure 5.7. For capillary 1 higher cell pressures (900 - 1100 mbar) compared to capillary 2 (500 - 700 mbar) were necessary to obtain optimum C flow rates

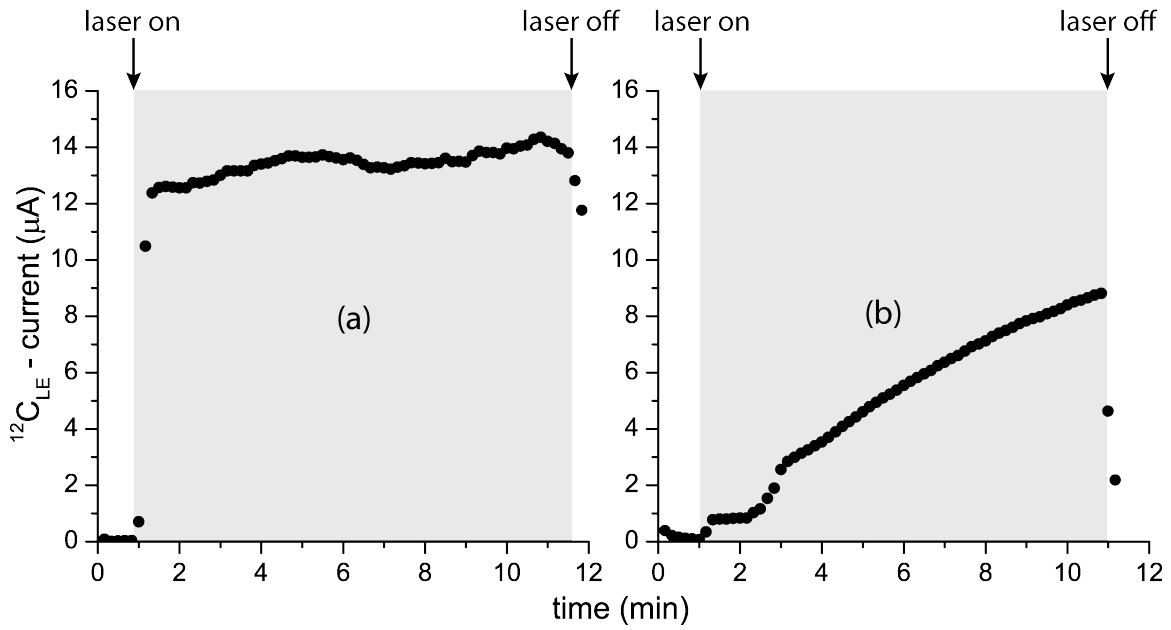

Figure 5.6: Depending on the C flow rate into the ion source one of the following cases occurs: (a) Optimum conditions cause a quick rise in the $^{12}C_{LE}$-current which is followed by a steady signal. (b) A low C flow results in a slow and steady signal rise. The current increase at 2.5 minutes is caused by an increase in the helium background pressure in the LA-cell. For both cases LA was used as a sample introduction technique.

and, hence, maximum ion currents. Routine LA-AMS measurements showed that the longer the capillaries were in use, the higher the LA-cell pressure had to be in order to maintain the gas flow rates, which were monitored vie the pressure in the ion source. This is due to gradual clogging of the capillary as a result of laser produced particles that are fine enough to pass through the filters and sediment along the capillary. Capillary 2 with the larger I.D. has shown to be more suitable for the LA-AMS setup as it clogs much slower (sever and will be employed for the following LA-AMS measurements.

5.1.4 Overall considerations

Assuming a CO_2 conversion efficiency of 53 % ± 2 % (see Section 3.2.1) and considering the ablation rate of (97 ± 5) µg/min of $CaCO_3$ (200 Hz, 1.8 J/cm^2) results in a CO_2 production rate of (23 ± 3) µg/min, corresponding to (6.2 ± 0.9) µg carbon/min. In order to assess the overall efficiency of the LA-AMS setup, this can be compared to the amount of C that is transported into the ion source (2 - 4 µg C/min). Accordingly, there is a discrepancy between the produced and the detected C of 30 - 60 %. Most likely CO_2 is lost in the LA-cell through the gap between the insert and the sample surface by diffusion. This loss can be reduced by increasing the helium gas flow rates (1 - 2 mL/min) into the ion source. Day to day variations of the gap size most likely result in changes in the CO_2-transport

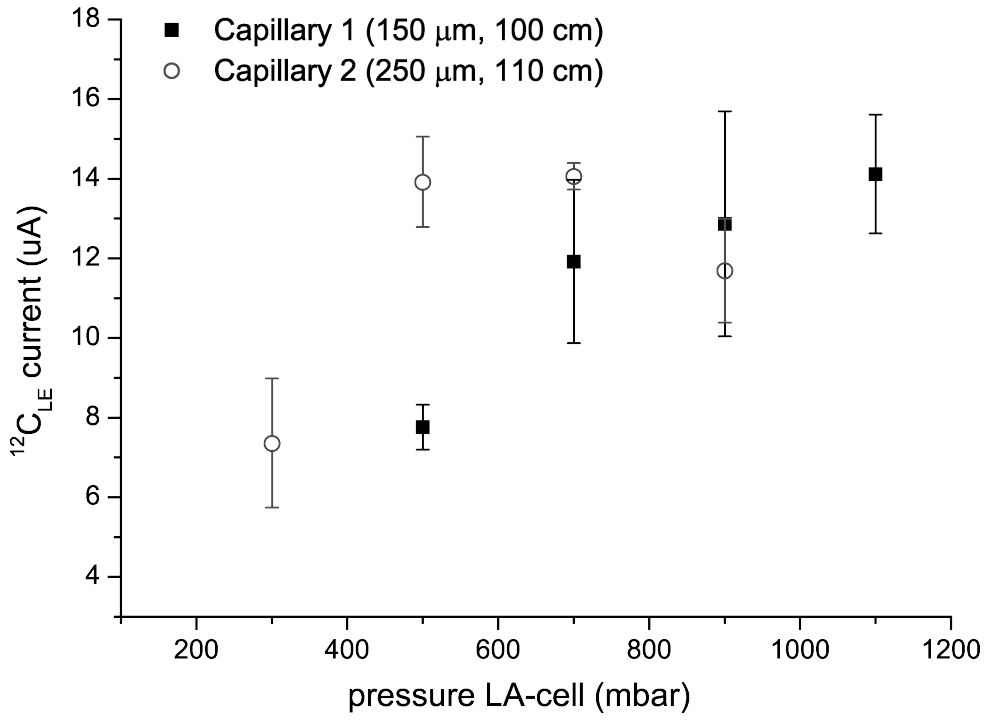

Figure 5.7: Ion current dependence on the helium background pressure in the LA-cell for two capillaries with different flow resistances. The maximum ion current is reached at different pressures for the two capillaries.

efficiency from the LA-cell into the ion source: a larger gap will result in a greater CO_2 loss into the sample box, thus reducing the C-flow into the ion source and vice versa. These variations are most likely the reason for the different transient behaviors that have been observed during LA-AMS measurements for the same measurement settings. A modification of the insert of the LA-cell could reduce the CO_2 losses into the sample box. The total efficiency of the LA-AMS setup can be derived by comparing the ablated C with the number of ions reaching the detector and is on the order of 5 ‰. Considering the CO_2 conversion efficiency and the losses in the LA-cell, i.e. comparing the C entering the ion source with the number of ions reaching the detector, the negative ion yield for the LA-AMS system is $\sim 4\,\%$ and, thus, approximately 1.5 times lower than for conventional gas measurements as reported by Fahrni et al. (2013). Most likely, the high carrier gas flow rate applied for LA-AMS cause losses in the sputter targets, thus, decreasing the sputtering efficiency. While the gas ion source principally seems to accept higher gas flows with respect to stability and vacuum conditions, possibly less CO_2 gets into contact with the Ti surface of the gas targets. The Ti acts as a getter material for the CO_2 (Middleton, 1984), from where it is subsequently sputtered and converted to negative ions. Previous tests at lower gas flows have shown that the target geometry plays a crucial role to achieve a high negative C-ion yield. For future measurements, the target geometry should be improved for high gas flows. A comparison of the key parameters for conventional gas

Table 5.2: Comparison of optimized settings during conventional gas and LA-AMS analysis.

	Conventional gas measurements	**LA-AMS**
Carrier gas flow (mL/min)	0.1	1.5
Gas mixture (% CO_2 in helium)	5	0.3 -0.5
C gas flow into ion source (μg/min)	2.7	2 - 4
Negative ion yield (%)	6	4

measurements and for the LA-AMS setup can be found in Table 5.2.

5.2 Radiocarbon analyses with LA

^{14}C analyses of natural samples using LA-AMS requires knowledge of the blank level, which defines the smallest detectable concentration, as well as the washout of the LA-cell and the effect of cross-contamination, as both factors play an important role when performing continuous scans. Accuracy, precision and reproducibility are further figures of merit, that determine what is achievable when applying the method to natural samples. These analytical aspects will be addressed in the following section.

5.2.1 Blank level

The standard corrected blank values were calculated according to Wacker et al. (2010) for the marble sample analyzed by LA-AMS and are displayed in the left part of Figure 5.8 (solid and open black circles), where also the mean ^{12}C-current corresponding to each blank measurement is depicted (red triangles). Dashed vertical lines separate different days or indicate the re-opening of the LA-cell. The error bars result from counting statistics with 18-24 ^{14}C counts per minute. Measurement times for each data point vary between 2.5 and 5 minutes. The laser settings were kept as similar as possible for the three measurement days (see Table 5.1 and caption of Figure 5.8). No obvious correlation between the ^{12}C-current and the blank level is observed, indicating that residual CO_2 in the gas volume of the ablation cell is not the main source of higher ^{14}C in the beginning of the experiment (open black circles). The mean blank value including all data points results in a $F^{14}C$ of 0.013 $\pm$ 0.004 (not shown in Figure 5.8). After a measurement time of approximately 15 minutes it converges to a level of 0.011 $\pm$ 0.002 (grey area in Figure 5.8). This is significantly higher than 0.006 $\pm$ 0.002 (shaded area) normally reached with the

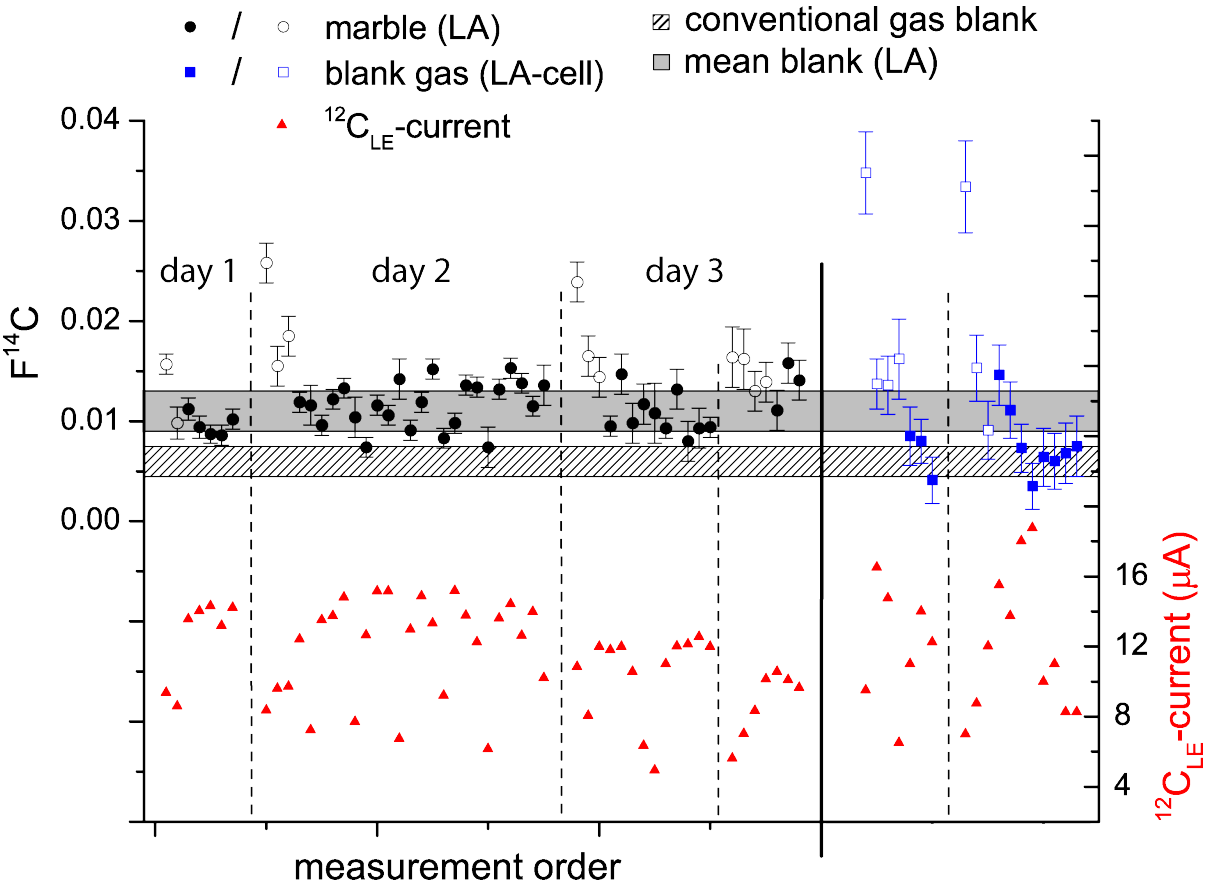

Figure 5.8: LA-blank measurements (black dots) during three days and blank gas passed through the LA-cell on two days (blue squares). The open symbols represent the first 15 minutes of measurement on each day and were excluded from calculating the mean blank value for the three days and its standard deviation (grey area). The shaded area corresponds to the conventional gas blank level. Furthermore, the ^{12}C-current (red triangles) corresponding to each blank measurement is depicted. Laser settings can be found in Table 5.1. The pressure in the LA-cell was set as follows: 200 - 500 mbar (capillary 2) on day 1, 500 - 1100 mbar (capillary 1) and 300 - 900 mbar (capillary 2) on day 2, 550 - 1100 mbar (capillary 1) on day 3.

conventional GIS. The initial elevation of the LA-AMS blank level on each measurement day is possibly caused by an exchange reaction between newly produced CO_2 and CO_2 previously adsorbed on the surfaces of the instrument, on samples or on deposits. After a sufficiently long exposure to CO_2 with constant $F^{14}C$, stable conditions are achieved.
Blank gas has also been passed directly through the LA-system at different cell pressures and with different CO_2/He-mixtures before introduction into the ion source. The results obtained for two measurement days are shown in the right part of Figure 5.8, where the open symbols represent the first 15 minutes of each day. Again, the initial blank level for each day is elevated, which confirms the assumption of gas exchange reactions taking place. Considering only the data points after the first 15 minutes, a $F^{14}C$ mean blank level of 0.008 ± 0.004 is yielded for the blank gas. This blank level is on the same order as the blank level from conventional gas measurements, which indicates that the higher blank value, observed during LA measurements in comparison to conventional measurements is the result of the LA process. Residual CO_2, adsorbed on the sample surface or the LA-cell interior that successively is removed by shockwaves formed by LA, desorption by light or heat generated during the laser pulse, might be the reason for the elevation of the LA-AMS blank level.

5.2.2 Washout and cross-contamination

The washout of the LA-cell, i.e. the time in which the is depicted in Figure 5.9 (a) after ablating a carbonate sample for 30 minutes. Once the laser is turned off the signal drops from 11 to 0.6 μA within 30 s corresponding to a time constant for washout of 6 s. The subsequent drop is much slower and, until, the lifetime of the target ($\sim$ 23 minutes), the level is still elevated compared to the current typically reached with helium on a cleaned target after pre-sputtering with Cs (<0.1 μA; dashed line). This elevation can be explained by CO_2 that escaped during the measurement into the sample box of the LA-cell. Therefore, the LA-cell is evacuated and flushed with helium between the measurements of different samples in order to avoid the carry-over of CO_2 from the previous sample. A second source possibly contributing to the ion current observed after the laser is turned off, is carbide that formed during sputtering of the CO_2 on the titanium (Ognibene et al., 2015).

The effect of cross contamination of the LA-AMS system was investigated and the results are summarized in Figure 5.9 (b). Laser and cell parameters were set to maximize the $^{12}C_{LE}$currents (settings as in Table 5.1 with capillary 1). Three samples with different ^{14}C content (marble, IAEA-C2 and the stalagmite in-house standard) were measured in the order indicated on the x-axis of the figure. Each data point corresponds to an

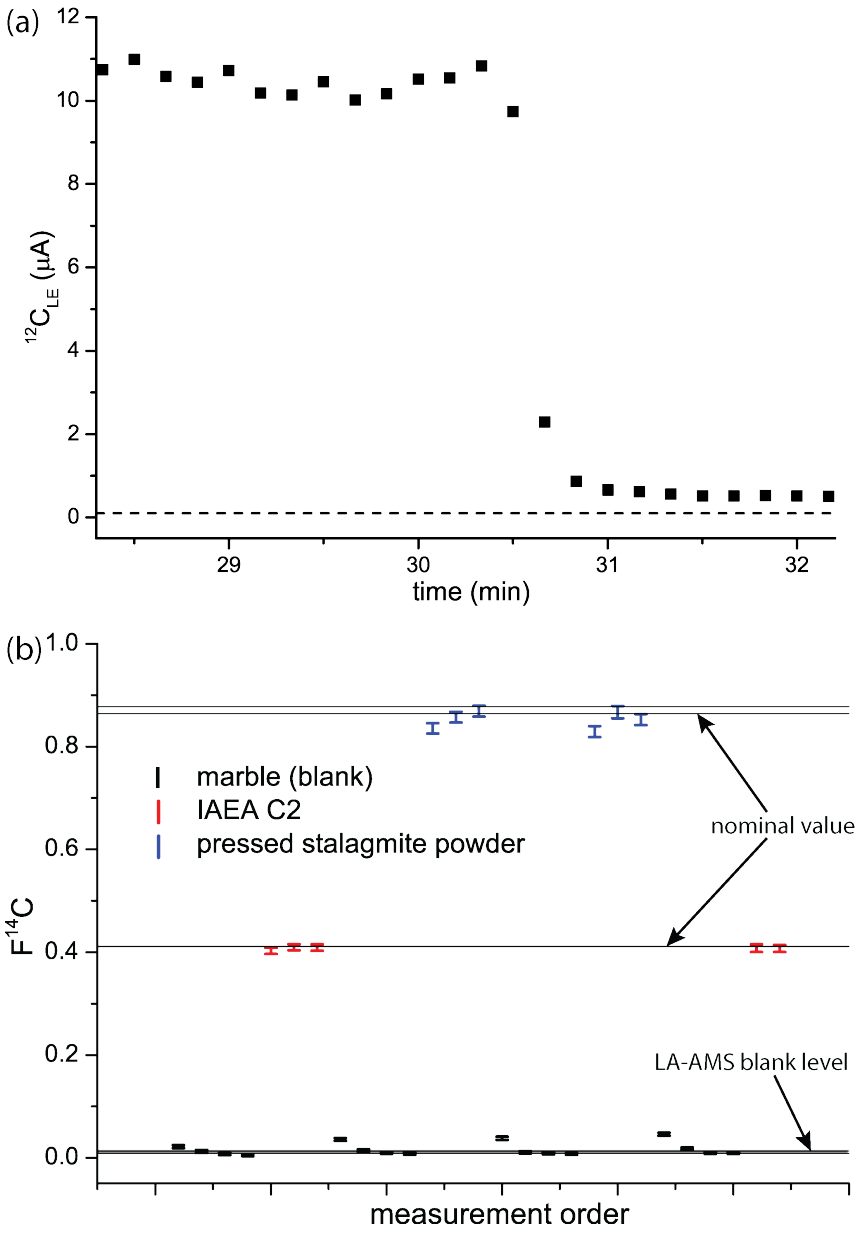

Figure 5.9: (a) Washout behavior of the LA-cell after lasing for 30 minutes which is an exceptionally long lifetime of the sputter target. The dashed line indicates the background level of the ion current which normally reaches 0.1 μA after pre-sputtering. (b) Study of the effect of cross contamination during LA. Blanks measured directly after standards are elevated. The same can be observed for standards measured after blanks. The grey band represents the blank range normally yielded for LA-AMS measurements. For the standard materials the standard deviation of the nominal value is shown (grey lines).

integration time between 3 and 6 minutes. Between ablation of different samples, the cell was evacuated and flushed with helium three times in order to minimize the level of residual CO_2 from the previous sample. The $F^{14}C$ of the blank sample increases by a factor of more than four after the measurement of a standard and this effect increases with time. When measuring a standard after a blank sample the opposite effect is observed: the first standard analyzed exhibits a lower $F^{14}C$. This is especially pronounced for the stalagmite standard, which has the highest ^{14}C content. A longer evacuation and flushing procedure between a standard and a blank sample did not lower the initial $F^{14}C$-ratio measured for the blank. It is thus likely that as in the case of the blank levels an equilibration between the newly produced CO_2 and CO_2 previously adsorbed on the surfaces of the instrument, samples or deposits is the major source of these deviations. As observed above for the blank levels, stable conditions are achieved after a sufficiently long exposure to CO_2 with the same $F^{14}C$.
The gas sputter targets show furthermore relatively strong memory effects (Fahrni et al., 2013; Ognibene et al., 2015). While gas targets are changed between individual samples in routine gas measurements, in a scan mode one target is used for numerous subsamples. A reduction of memory on the gas targets will be necessary to increase precision and reliability of LA-AMS measurements. Thus re-designing the sputter targets should significantly reduce memory effects in scan modes.

5.2.3 Reproducibility of analyses of reference materials

As no matrix matched ^{14}C standards for carbonates are available, pressed IAEA C2 and CSTD powder were used to investigate how accurate nominal values of reference materials can be reproduced using the LA-AMS setup. Ion currents yielded for the pressed carbonate powders were comparable to those of the marble sample. The measurement parameters are listed in Table 5.1 and the results are sown in Figure 5.10. The CSTD standard was measured multiple times on four measurement days. The measurement precision for the single days was between 0.7 % and 1.1 % yielding a mean $F^{14}C$ of 0.94 ± 0.01, which matches within one standard deviation the nominal value of 0.9445 ± 0.0018. Eight replicates of the C2 standard on two measurement days yielded a mean $F^{14}C$ of 0.410 ± 0.009, which matches within one standard deviation the certified value of 0.4114 ± 0.0003. Measurement precisions reached for the two days were 2.9 % and 0.3 %, respectively. The low precision obtained on day 5 is due to overall low ion currents attained that day. The three values from "day 6" (open symbols) are from the experiment shown in Figure 5.9 (b), not considering ^{14}C-depleted data points. Eight replicates of the in-house prepared powder from a modern stalagmite yielded a $F^{14}C$ value of 0.84 ± 0.01, which agrees with the value of 0.871 ± 0.007 obtained from five conventional gas measurements within two standard deviations. For the single days the precision achieved were 1.5 % and 0.8 %.

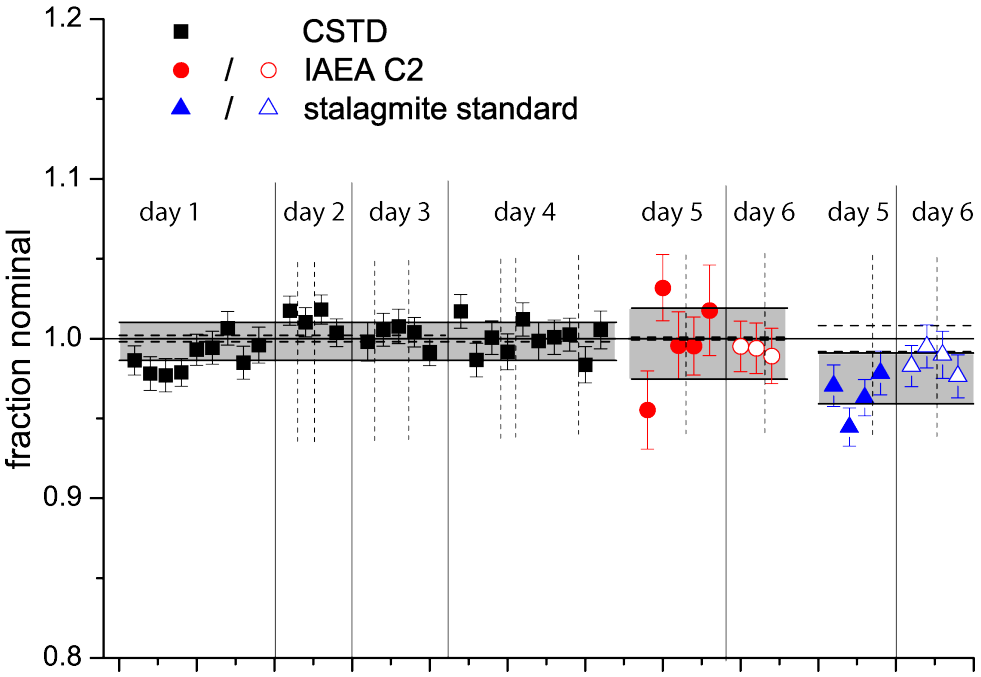

Figure 5.10: Measured F^{14}C divided by the nominal value (referred to as 'fraction nominal') for three standard materials using LA-AMS. The open symbols represent data that is also shown in Figure 5.9. Solid vertical lines indicate different measurement days, dashed lines represent the measurement of other samples in-between. The solid horizontal line indicates the nominal value of the standards, dashed horizontal lines the standard deviation of the nominal value and grey areas represent one standard deviation of the measured values.

5.2.4 Summary

The blank value of the LA-AMS setup is sufficiently low to allow ^{14}C measurements of ages as low as 35 000 years. Standards could be reproduced with a precision of better than 1 % and reference materials matched nominal values within the uncertainties. When performing continuous scans on natural samples with changing ^{14}C-content, washout and cross-contamination need to be considered. The LA-cell cannot be evacuated and flushed during the scan. As a result, the ^{14}C signal can be altered by the washout. A significant effect of cross-contamination could be observed between samples of highly different ^{14}C-content (Figure 5.9,(b)). Since for naturally grown samples the difference in ^{14}C-content between two neighboring layers is significantly smaller, this carry-over effect is less pronounced when performing continuous scans. Nevertheless, for future experiments a suitable data processing scheme should be applied where carry-over correction for the washout and other cross-contamination effects are taken into account.

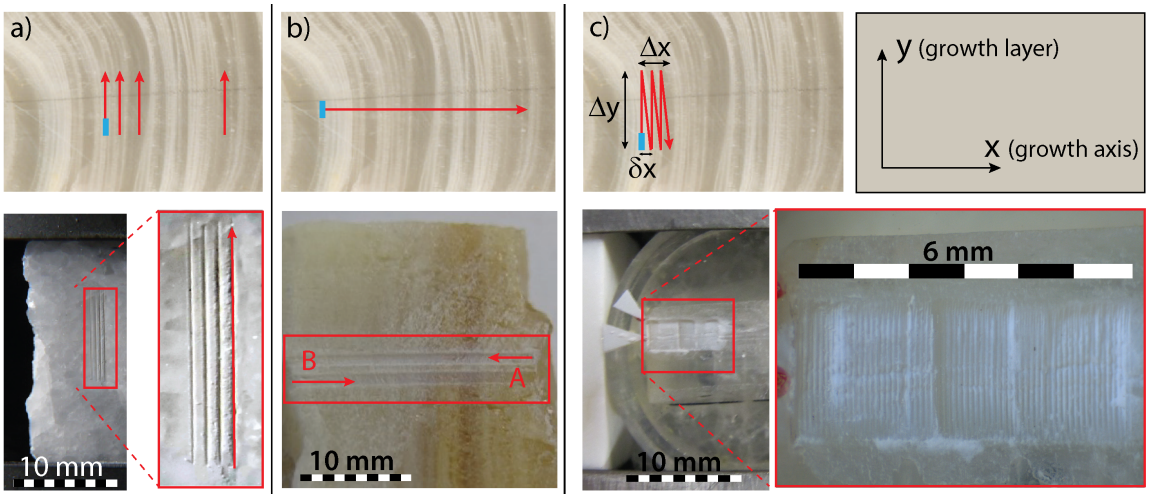

Figure 5.11: Comparison of the three scanning modes: (a) discrete layer analysis within a growth layer, (b) survey scans parallel to the growth direction, (c) precision scans. Red arrows represent the scanning direction and blue rectangles indicate the orientation of the laser spot. In the upper row the scanning schemes are depicted, while the lower row shows the corresponding laser tracks on real samples: (a) single scans on a marble sample. (b) Two survey scans in opposite directions. (c) Laser tracks of a precision scan on a stalagmite sample (BU-4) embedded in epoxy resin.

5.3 Sampling strategies

Requiring only minimal sample preparation, the new setup is capable of providing a quasi-continuous stream of ^{14}C data while the sample is being ablated. Three generally different sampling strategies have been developed in order to provide high flexibility in the analysis of different layered materials. Discrete scans, comparable to conventional sampling, can be performed within growth layers. A fast scan mode, that provides a quick overview about the ^{14}C content of the sample and a high resolution mode performed at regions identified as interesting. Here, data is integrated over several minutes, while the ablation rate is kept constant, to achieve higher precision.
The xy-positioning system in the LA-cell is controlled by an in-house developed LabVIEW program (National Instruments, Austin, Texas, USA) and allows precise movement of the sample relative to the laser beam. A scheme of each implemented mode is depicted in the upper part of Figure 5.11. The x-direction represents the growth axis of the carbonate record, the y-direction points along a growth layer and red arrows indicate the direction of the laser track on the sample.

(i) **Discrete layer analyses (mode 1)** are equivalent to conventional drilling of samples by ablating material along the growth layer only. The tracks can be placed

at any spot on the sample and the spatial resolution along the growth axis depends on the laser beam width and the alignment of the laser track relative to the growth layer. In order to reach the optimum spatial resolution, the growth layer has to be oriented parallel to the laser beam. Otherwise, the 'effective' spatial resolution will be reduced as the $F^{14}C$ value will reflect portions of all layers that were ablated.

(ii) A **survey scan (mode 2)** allows scanning along an arbitrary distance on a sample. The spatial resolution ultimately depends on laser beam size, laser repetition rate and scan speed.

(iii) A **precision scan (mode 3)** allows the continuous sampling along the growth axis while increasing the measurement time within a growth layer by scanning in a zig-zag pattern. Here, part of the scan with a length Δy is performed within single growth layers followed by a return scan with a displacement δx along the x-axis. The entire length in direction of the growth axis is denoted with Δx. These parameters will be reported as (Δx, Δy, δx).

In the bottom row of Figure 5.11 pictures of the laser tracks corresponding to the different measurement modes are depicted. Red boxes indicate the area in which the scans were performed. In part (a) four discrete scans on a marble sample are shown and an enlargement of the laser tracks can be seen. Figure 5.11 (b) shows two 'survey scans' labeled A and B. The two scans were performed on a stalagmite sample in opposite direction. In Figure 5.11 (c) a precision scan on a stalagmite sample is depicted. The scan is enlarged in the right red box of part (c) and the varying depth of the individual tracks results from multiple scan lines placed on top of each other.
In the case of conventional graphite and gas ^{14}C measurements with AMS, data evaluation has the following scheme: individual samples are measured and the normalized ^{14}C /^{12}C-ratios are integrated yielding one averaged ^{14}C concentration. Hence, the 'data integration period' is equal to the 'data acquisition period', which is also the case for mode 1. Mode 2 and 3 require a different data evaluation procedure: the ^{14}C /^{12}C-ratio continuously changes as the laser scans across different growth layers of the carbonate record and depending on the measurement time one or more sputter targets are used. This offers a great flexibility concerning the data evaluation as the 'data integration periods' and, hence, spatial resolution and measurement precision can be selected according to the needs of the application.
A stalagmite sample considered 'ideal' for first LA-AMS analyses due to its distinct ^{14}C signal is used to compare the different scanning modes. A large growth rate and a low dead carbon fraction (dcf), which is C originating from the ^{14}C depleted host rock above the cave, result in a pronounced bomb peak with a difference in $F^{14}C$ of more than 0.3. Aspects as analysis time, material consumption, spatial resolution and measurement precision will

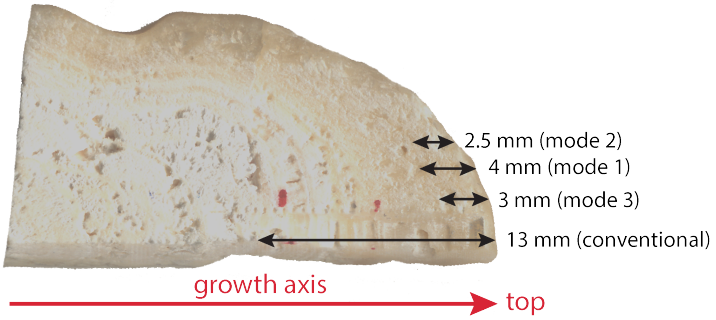

Figure 5.12: Areas of sampling for the different measurement modes on the top section of stalagmite ER-77. A survey scan (mode 2) was performed covering a distance of 2.5 mm, the discrete layer analysis (mode 1) covered an effective distance along the growth axis of 4 mm, the precision scan covered an effective distance of 3 mm and conventional sampling was performed in the top 13 mm right at the growth axis of the stalagmite.

be addressed. Conventional samples are available and will be compared to the LA-AMS data: Fohlmeister et al. (2011) analyzed the ^{14}C content of 17 samples within the upper 13 mm that were taken by micro milling with a spatial resolution of 600 μm. The sampling was performed along the stalagmite's growth axis consuming about 8 mg of material per subsample and a measurement precision of 0.4 % for each subsample was obtained. The bomb peak expands across the six topmost samples covering a width of approximately 4 mm. The overall analysis time for each conventionally analyzed subsample including sampling, chemical preparation and AMS-measurement is on the order of one hour. Hence, establishing a data set, covering the entire bomb peak takes approximately six hours. The three different scanning modes were performed with different offsets to the growth axis as indicated in Figure 5.12.

5.3.1 Discrete layer analyses

Nine single measurements each covering a scanning distance Δy of 2 - 2.6 mm were performed. Measurement settings for this and all subsequent experiments are listed in Table 6.1. The scan velocity was set between 2.5 - 5 μm/s and the lateral displacement between each scan covered 300 μm for the seven topmost samples and 1 mm between the two last ones. For each of the nine scans the average $F^{14}C$ was calculated and is plotted in Figure 5.13 (a), where the ^{14}C /^{12}C raw data (blue dots) exhibits the bomb peak after 60 minutes of measurement. The red lines indicate the lifetime of a sputter target corresponding to the period of continuous data acquisition. The black lines indicate 'data integration periods'. Integrated, background corrected and normalized data are depicted in Figure 5.13 (b), where red circles represent the LA-data and black squares are from

conventional measurements. A measurement precision on the order of 2 % is achieved and the spatial resolution, defined by the crater width, is 110 μm. The material consumption lies between 1 - 1.5 mg per subsample and the measurement time ranges from 8 - 15 min summing up to a total analysis time of approximately 2 hours. The LA-derived data match the conventionally derived $F^{14}C$ values very well within the uncertainties (Figure 5.13 (b)). There is capacity for placing two to three additional subsamples between the topmost 7 samples and up to nine between the two lower ones.

5.3.2 Survey scan

A survey scan covering the top 2.5 mm of the stalagmite was performed with a scan velocity of 2.5 μm/s resulting in an overall measurement time of 17 minutes. The $^{14}C/^{12}C$ raw data are shown in Figure 5.13 (c) (blue dots) and with increasing scanning time the $^{14}C/^{12}C$-ratio starts to increase as the onset of the bomb peak is reached. The scan was performed on one sputter target (indicated by the solid red bar) and a 'data integration period' (vertical dashed lines and black horizontal bars) of 60 sec was selected. The corresponding $F^{14}C$ is represented by the red circles in Figure 5.13 (d). The survey scan was performed within less than 20 minutes yielding a precision for each subsample on the order of 4 % and a spatial resolution around 260 μm. 1.6 mg of $CaCO_3$ were consumed for the entire scan corresponding to 0.1 mg for each subsample, which is one order of magnitude less than consumed in mode 1. The main advantage of survey scans is the short analysis time while a comparably large section of the sample is covered: several centimeters can be analyzed within one hour. This allows to establish a quick overview of the ^{14}C-content across a carbonate record, albeit at the cost of measurement precision. In the case of the ER-77 the scan was performed with an offset of approximately 1 cm relative to the growth axis. The growth layer structure at this region is different than at the center of the stalagmite as growth layers get thinner and start to slope. Therefore, the bomb peak is found in the upper 2.5 mm instead of the upper 4 mm as it is the case for conventional analysis where samples were taken at the stalagmite's growth axis.

5.3.3 Precision scan

Three precision scans were performed covering the top 3 mm of the ER-77 stalagmite. For the first scan the velocity was set to 200 μm/s allowing to scan back and forth on the same sputter target. The scan parameters were ($\Delta x = 3$ mm, $\Delta y = 2$ mm, $\delta x = 100\,\mu$m). A second and third scan stacked on the track of the first one, this time facing towards the

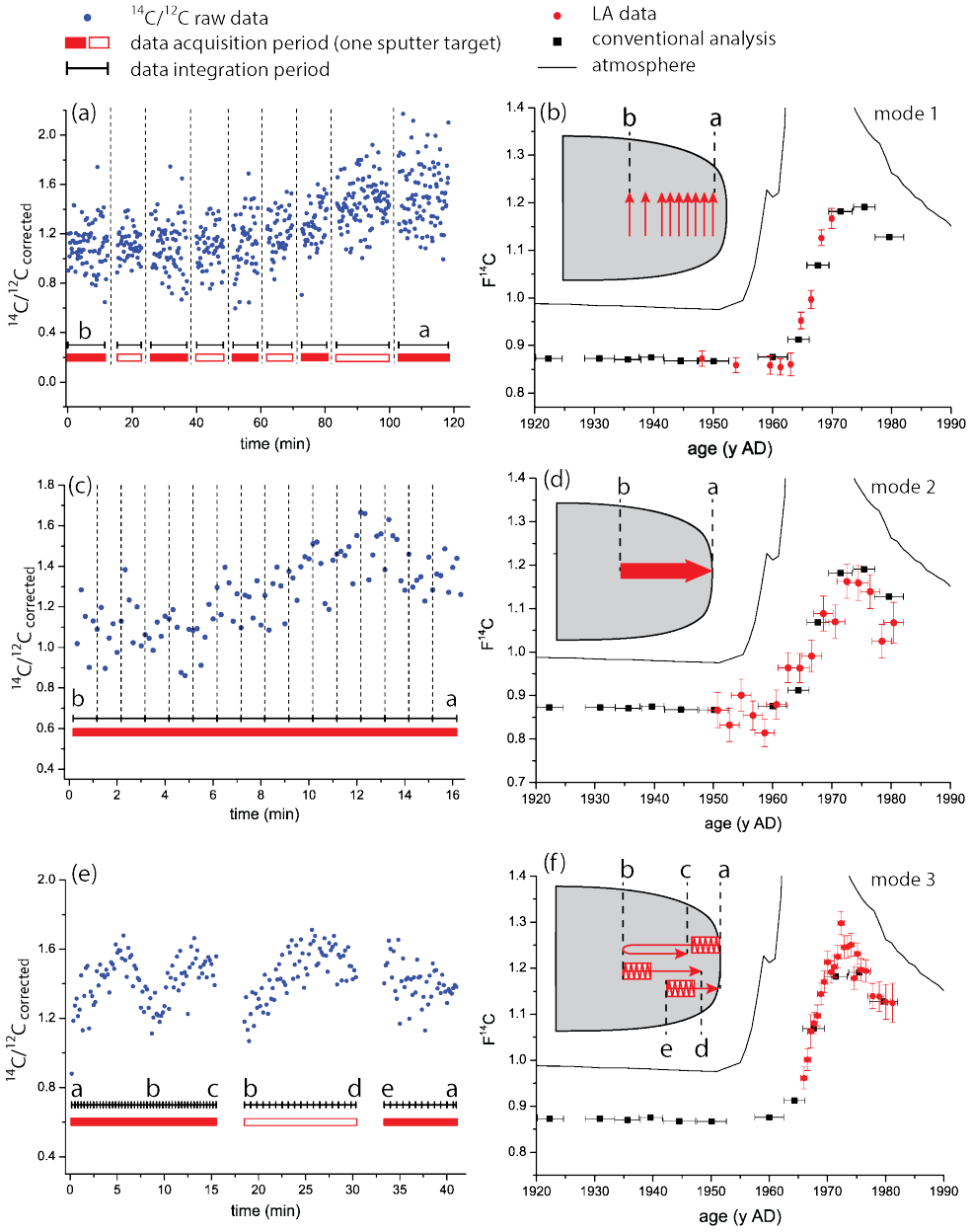

Figure 5.13: Comparison of the three measurement modes using stalagmite ER-77: (a) and (b) discrete layer analysis, (c) and (d) survey scan, (e) and (f) precision scan. In the left part of the figure corrected ^{14}C $/^{12}C$-ratios are plotted against the acquisition time. Each red bar (open and solid) corresponds to one sputter target and black bars correspond to the integration time. In the right part of the figure, the integrated $F^{14}C$ values are shown and the inserts indicate the path of the scan (not to scale). The precision scan (mode 3) consists of three subscans: first, a scan forth and back on one sputter target (a to b to c), second a scan towards the top (b to d) and third a scan overlapping with the previous scan (e to a).

top, were performed with a scan velocity of 100 μm/s, while all other parameters were kept constant. The scanning pattern is reflected in the $^{14}C/^{12}C$ raw data (blue circles) shown in Figure 5.13 (e). The two peaks on the first sputter target (first red line) correspond to the back and forth movement across the sample. The second and third scan were performed on two sputter targets with an overlap at the transition. In the last two scans, the bomb peak was crossed only once. The average of one zig-zag step for each scan was chosen as the integration interval (compare black horizontal bars in Figure 5.13 (e)). The average for all three scans was calculated and the results are represented by the red squares in Figure 5.13 (f). The signal intensity of the four data points at the top was much lower than for the other samples. Therefore, the mean of two zig-zag steps was taken resulting in a reduced spatial resolution (300 μm). A relative error between 2 and 4 % is obtained. The spatial resolution for the other subsamples is in the order of 200 μm for an integration time of 60 s with a measurement precision of 2 % and a material consumption of 130 μg $CaCO_3$.

Table 5.3: Comparison of the LA-AMS modes with conventional graphite-AMS measurements using ER-77. The listed values indicate the typical range for each quantity, but depending on settings like the scan velocity, repetition rate, etc. they can be different.

Measurement mode	**time/data point**	**spatial resolution**	**material consumption**	**measurement precision***
unit	min	μm	mg $CaCO_3$	%
Conventional graphite	60	600	8	0.4
LA - discrete layer analysis	10	100 - 200	1 - 1.5	1 - 2
LA - survey scan	0.5 - 2	300 - 3000	0.1 - 0.2	4 - 6
LA - precision scan	0.5 - 4	200 - 1000	0.1 - 0.4	1 - 3

* for a modern sample

5.3.4 Summary

Continuous scans offer a great flexibility regarding the spatial resolution and the measurement precision. When performing a survey scan at a scan velocity v_{scan} of 10 μm/s, several centimeters can be analyzed within one hour. Operating at a laser repetition rate of 200 Hz, about 6 mg of material will be consumed. With an integration time t_{int}=10 s, the spatial resolution corresponds to 200 μm and for a modern sample the measurement precision p is on the order of 5 %, assuming a negative ion current of 6 μA. This can be mathematically expressed by combining the relation between the spatial resolution, the scan velocity and the integration time

$$\Delta x = v_{scan} \cdot t_{int} \tag{5.1}$$

with the relation between the number of counts in the detector N, the efficiency $\mathcal{E}$, the C production that depends on the laser frequency and fluence $P_C(\nu,F)$ and the measurement precision $p = 1/\sqrt{N}$

$$N = P_C \; \mathcal{E} \; t_{int} \tag{5.2}$$

yielding the following expression

$$\Delta x \cdot p^2 = \frac{v_{scan}}{P_C(\nu, F) \; \mathcal{E}} \tag{5.3}$$

The product of the spatial resolution and the measurement precision depends on the scan velocity, laser parameters and the efficiency of the setup. An improvement of the spatial resolution results in less precise data and vice versa.

Each of the presented scanning modes implemented for LA-AMS measurements has advantages and disadvantages with regard to measurement time, achievable precision, spatial resolution and material consumption. The major advantage of all three measurement modes compared to conventional methods is the analysis time, which is by more than a factor of 50 shorter for mode 2 and 3 per subsample. Mode 1 is approximately six times faster than conventional analysis, but yields up to ten times lower measurement precisions. Longer LA analysis times will result in better counting statistics and, hence, in increased measurement precision, which implies to select long scan distances within one growth layer (mode 1 and 3) and to choose low scan velocities (valid for all three scanning modes) when aiming for high measurement precision. This is limited by the fact that with decreasing scan velocity the laser drills deeper into the material, which eventually results in a lower CO_2-production when the sample surface moves out of the laser's focus, causing a loss of signal intensity. Spatial resolution is up to a factor of 2 - 6 better for LA-AMS than for manually drilled samples. Ablating across different growth layers is only desired in the case of survey scans. For discrete layer analysis and precision scans, material is collected within one growth layer, but since the laser beam is of rectangular shape the maximum scanning distance within each growth layer is limited by the region of parallel growth in the sample (compare Figure 5.11 (a) and (c)). This could be improved by using a smaller, quadratic or circular spot, at the expense of CO_2 production. Consequently, signal intensities obtained with LA-AMS setup need to be improved, which could be achieved by a modified cell design allowing to ablate at higher laser fluences or by lowering the gas losses in the LA-cell.
The material consumption depends in the first place on the laser fluence and repetition rate as well as on the measurement time: higher repetition rates and longer measurement times result in higher material uptake, therefore, subsamples of survey scans consume less material than the other modes at the cost of measurement precision. Nevertheless, for mode 2 and 3 the material needed for the ^{14}C analysis of one subsample is significantly below the amount, which is required for the measurement of one conventional sample.

With all three measurement modes the ^{14}C in stalagmite ER-77 was reproduced within the uncertainties, while different analysis times, precision and spatial resolution were obtained for the different modes. The precision scan revealed that the bomb-^{14}C reaches $F^{14}C$ levels of up to 1.30, whereas conventional data suggested that the peak is at a $F^{14}C$ of approximately 1.20. This highlights the enormous potential of the novel method.
The key findings for all three LA-AMS scanning modes and for conventional AMS measurements are summarized in Table 5.3.

6 LA-AMS of natural samples*

In the following chapter LA-AMS is used for the analysis of natural samples. The first part covers terrestrial carbonates and in the second part marine carbonates, such as corals and shells are addressed. Samples analyzed were selected according to their (i) ^{14}C signal sequence, i.e. whether they exhibit a distinct signal such as the bomb peak, (ii) the magnitude of the signal change, and (iii) the spatial expansion of the signal in the sample. The major influencing factors on the ^{14}C signal in a carbonate record are (i) the growth rate of the sample, as faster growing samples record temporal changes in the ^{14}Csignal in a larger sample section, and (ii) on the attenuation of the signal, resulting from the mixing of reservoirs with different ^{14}C content. In the case of stalagmites the atmospheric ^{14}C imprint is attenuated mainly by the dead carbon fraction (dcf) that originates from the host rock above the cave and whose magnitude is very variable from cave to cave.

6.1 Terrestrial carbonates

Four terrestrial carbonates, i.e. stalagmites comprising a variety of ^{14}C signals were analyzed, applying the different measurement modes introduced in Section 5.3. Two stalagmite samples exhibiting the ^{14}C bomb imprint - one with a pronounced signal (see

Table 6.1: Summary of the settings used for the subsequent LA-AMS analyses.

	Physical Quantity	**Settings**	**Unit**
Laser parameters	Repetition rate	150 -250	Hz
	Laser energy on sample (per pulse)	0.8 - 2	mJ
	Laser spot size	680 x 110	μm
	Fluence on sample (per pulse)	1 - 2.5	J/cm^2
Gas flow parameters	Gas flow rate	1.5	mL/min

*Parts of this chapter are submitted to publication (Welte et al., submitted)

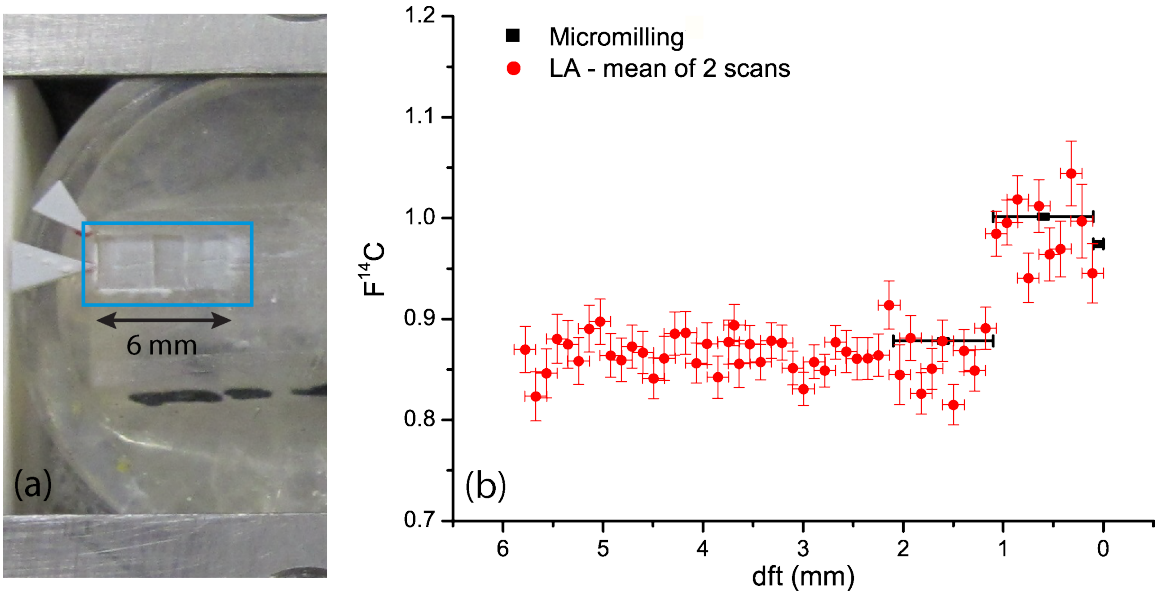

Figure 6.1: (a) Laser tracks of the two precision scans performed on the BU-4 stalagmite. (b) LA-AMS data (red circles) compared to conventionally derived solid AMS measurements (black squares). The high resolution achieved with LA-AMS allows to reveal the abrupt onset of the bomb peak at a distance from top (dft) of 1 mm.

previous chapter) and the other one with a more attenuated one - were investigated. A slow growing stalagmite covering almost 10,000 years within a few cm and a growth stop of more than 300,000 years is also analyzed. Furthermore, exceptional large ^{14}C variations are revealed in a stalagmite from an alpine cave. Signal intensities obtained for the stalagmite samples were on the order of 18 μA, which is only slightly lower than ion currents yielded for conventional gas samples.

6.1.1 Stalagmite BU-4

Two stacked precision scans were performed in opposite directions covering the top 6 mm yielding an overall measurement time of approximately one hour. The scan velocity was set to 140 μm/s and the parameters of the precision scan were (Δx = 6 mm, Δy = 2 mm, δx = 100 μm). The laser tracks are depicted in Figure 6.1(a) and the integration time corresponds to one zig-zag step for both scans. Subsequently, the average $F^{14}C$ of the two scans was calculated, which are depicted in Figure 6.1(b) (red circles) and compared to conventionally obtained data points (black squares). Both data sets match well within the uncertainties. The abrupt onset of the bomb peak could be revealed by the LA-AMS data achieving a spatial resolution of 200 μm for each data point and yielding a relative

uncertainty on the order of 2 - 3 %. The bomb peak of the BU-4 covers a $F^{14}C$ increase of 0.12, which is less than half of the rise found for the ER-77 and it is located in the upper millimeter.
Averaging the LA-AMS data that spatially correspond to one conventional data point, a relative uncertainty of 0.9 % is yielded, which is by a factor of three higher than the uncertainty obtained for conventional analysis. However, the analysis time was approximately three times shorter for LA-AMS compared to conventional measurements.

6.1.2 Stalagmite SOP-20

SOP-20 is an interesting sample for demonstrating the applicability of the LA-AMS method: (i) due to its slow growth over nearly 9000 years, a drop covering a difference in $F^{14}C$ of more than 0.3 is expected within a few cm. (ii) The hiatus appears as a $F^{14}C$ step covering approximately 0.3. The stalagmite consists of three pieces as shown in Figure 6.2 (a) to (c).

LA-AMS analysis of SOP-20

In the following paragraph data resulting from multiple scans that were performed on each of the three sections of the SOP-20 stalagmite are presented. Open circles represent data points that either exhibit $^{12}C_{HE}$-currents of less than 3 μA or an unstable $^{13}C/^{12}C$-ratio, so that the fractionation correction cannot be performed properly. These data points should be treated with care.

- **SOP-20 top**

  Two stacked scans were performed on the top part, (i) a precision scan consisting of seven sub-scans from top to bottom and (ii) a survey scan consisting of three sub-scans from bottom to top. The results for both scans are depicted in Figure 6.2 (d). Dark and light blue squares (open and solid) represent the precision scan, while red and purple circles (open and solid) correspond to the survey scan. The sub-scans are color-coded in the figures. The parameters of the precision scan were (Δx = 27 mm, Δy = 4.5 mm, δx = 100 μm). Each data point in Figure 6.2 (d) corresponds to an integration time of 80 s resulting in an overall measurement time of the seven precision scans of 90 minutes. The spatial resolution of the data points

ranges from 140 - 540 μm and correspond variations in the scan velocity between 100 and 500 μm/s. The measurement precision is on the order of 2 %.
For the survey scan, which covers a distance of 24 mm spatial resolution of the data points ranges from 700 to 1700 μm depending on the scanning velocity that was set between 10 and 25 μm/s, resulting in an overall measurement time for the three sub-scans of 25 minutes. The integration time is 60 s yielding a measurement precision on the order of 4 - 5 %.
When comparing the two scans, a small offset between the two datasets can be observed. The scan performed from top to bottom is shifted to higher $F^{14}C$ in comparison to the scan performed from bottom to top. This is possibly caused by a combination of transport delay from the ablation spot to the ion source and of cross contamination: during the scan from top to bottom (bottom to top), the measured sample is affected by the sample measured previously and, hence, the $F^{14}C$ is higher (lower) when the scan is performed from young to old (from old to young). A χ^2-test, that is used to determine whether there is a significant association between two variables, was applied to the two scans. First the 60 data points from the precision scan were averaged to spatially match the 20 data points from the survey scan. For each pair the χ^2 value was calculated according to:

$$\chi_i^2 = \frac{(x_i - y_i)^2}{\Delta x^2 + \Delta y^2} \tag{6.1}$$

where x_i and y_i denote the single data points of the two scans x and y, and Δx^2 and Δy^2 the corresponding uncertainties from counting statistics. The χ_i^2 were then summed up and divided by the degrees of freedom, in this case 19 (20 measurement points), yielding a value for the reduced χ_{red}^2 of 2.3, which should be close to 1. This is not within the 95 % confidence limits ranging from 0.5 to 1.8. When shifting the survey scan 1 mm to the right, a χ_{red}^2 of 1.3 is yielded, which lies within the 95 % confidence limits, confirming the assumption that there is a significant delay between the time of lasing at a certain region and the actual analysis of the corresponding CO_2 gas. The time delay corresponding to the shift of 1 mm equals 23 seconds. Further investigation on the effect of cross-contamination is necessary and a suitable data-evaluation scheme needs to be developed. It is suggested that without a proper correction procedure always two scans facing in opposite direction should be performed and the corresponding average $F^{14}C$ for each location should be taken.
Furthermore, conventional data is plotted in Figure 6.2 (d), represented by the black stars. The conventional sampling was done using a commercial microdrill (5410A-DRO, Sherline, USA) with a drill of 0.8 mm width operating between 600 and 800 rpm. The sampling was performed at 400 μm spatial resolution and the material was subsequently weighed to aliquots of roughly 400 μg. The ^{14}C-analysis

was done with a recently introduced method at the gas ion source of the MICADAS (Seiler et al., in prep.), where 100% phosphoric acid is added to the samples and the formed CO_2 is directly flushed into the ion source. The trendline of the precision scan matches well with the GIS data. The comparably large discrepancy of the LA-data between 22 and 25 mm is discussed below.

- **SOP-20 middle**

Three scans were performed on the middle section of the SOP-20 as depicted in Figure 6.2 (e). The stalagmite was embedded in a thin layer of epoxy resin, allowing both sides to be used for LA-analysis. Therefore, laser tracks were placed on both sides of the section, which are expected to generate the same signal evolution. First, a precision scan (Δx = 12 mm, Δy = 3 mm, δx = 100 μm) consisting of five sub-scans was performed from bottom to top on the front side with a scan velocity of 600 - 800 μm/s (open and solid purple squares). The spatial resolution is on the order of 1 - 1.2 mm with an integration time of 100 seconds and an overall measurement time of 15 minutes. A measurement precision between 3 and 4 % is yielded. Second, a precision scan (Δx = 18 mm, Δy = 3 mm, δx = 100 μm) from top to bottom on the back side of the section was performed with an overall measurement time of 25 minutes. The scan velocity of 800 μm/s yielded a spatial resolution of 1.5 mm when averaging 100 seconds, with a measurement precision between 2 and 3 %. Third, a survey scan covering 22 mm from bottom to top on the back side (orange squares) was performed. The scanning velocity was 25 μm/s and the average of 40 seconds correspond to a spatial resolution of 1 mm and an overall measurement time of 25 minutes resulting in a measurement precision between 3 and 4 %. Finally, conventional samples (method as above) were taken at regions were large discrepancies between the LA-scans were found and are represented by the black stars.
Between a dft of 33 and 40 mm, the precision scan performed on the front (purple squares) matches the data obtained from the survey scan (orange squares) when omitting the data with low ion currents and unstable $^{13}C/^{12}C$-ratio (open symbols). The last two data-points are most likely depleted due to contamination with epoxy resin from embedding. Between 27 and 35 mm the data from the precision scan on the back (green) exhibit an unstable $^{13}C/^{12}C$-ratio (open symbols). Therefore, this data is not considered in the following discussion. Between 35 and 43 mm the data matches the trendline given by the two regions with known $F^{14}C$-values (black stars). The last two data points show an elevation relative to the conventional data. The survey scan (orange squares) generally is in good agreement with the conventional data, even around 44 to 48 mm, where low currents were obtained. Only the last data point shows an elevated $F^{14}C$. Between 40 and 45 mm from top four subsequent data points exhibit too high values. The χ^2_{red} was calculated for the three scans yielding values between 4 and 8, which is not within the 95 % confidence limits.

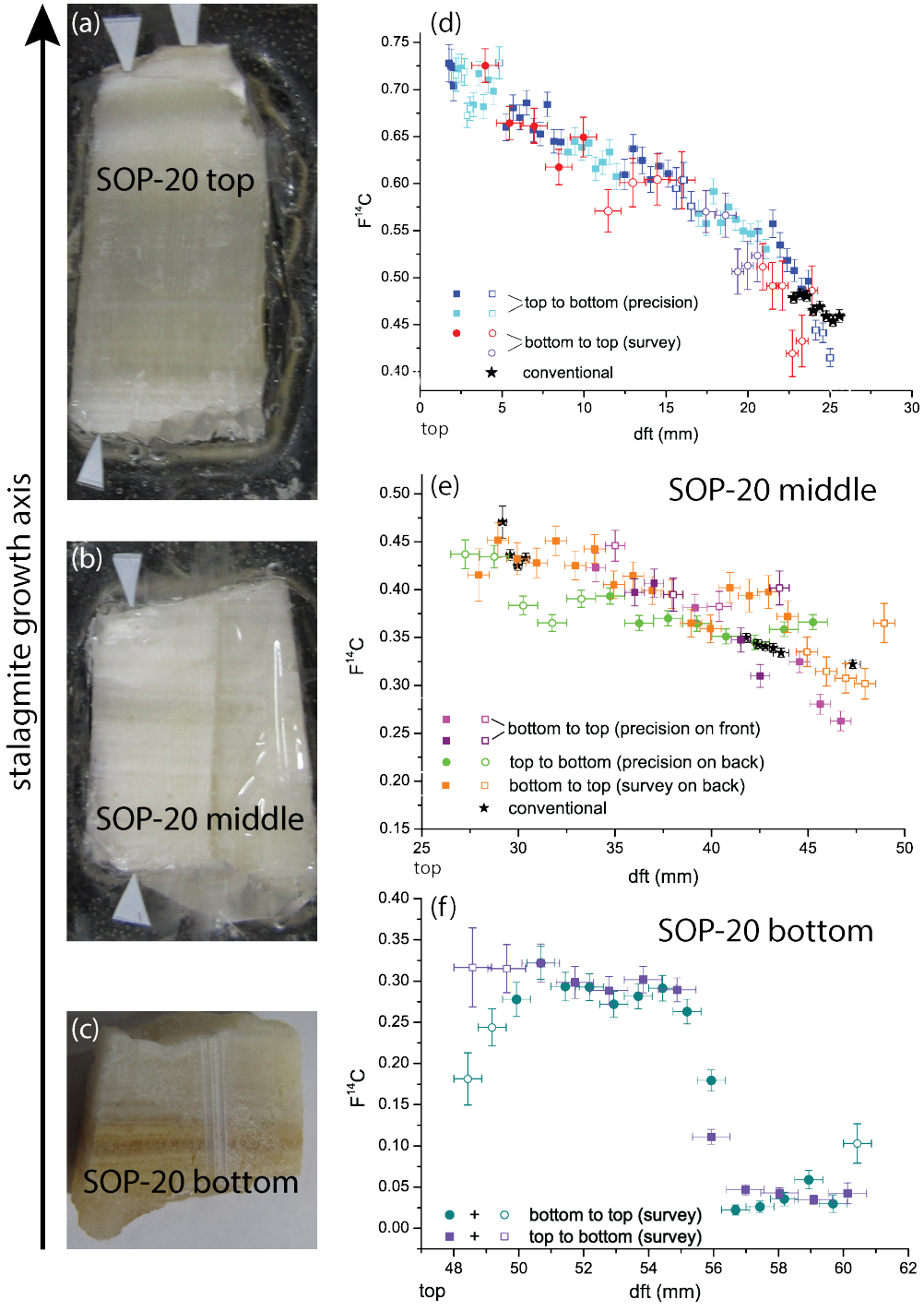

Figure 6.2: (a) to (c) show the three parts of stalagmite SOP-20 chronologically aligned. The black arrow indicates the growth axis. Subfigure (d) to (f) depict the signal derived from LA-analysis for the three pieces. Open symbols represent measurement cycles that should be treated with care due to low ion currents or where the fractionation corrections cannot be applied.

The precision scan performed from bottom to top (purple squares) exhibits too low values, which could also be the result of a contamination with epoxy. For the region between 35 and 40 mm all three scans match within two standard deviations, but no conventional data is available to confirm the LA-data. Generally, measurement conditions during the analysis of this sample were not optimal as ion currents were low and the $^{13}C/^{12}C$varied considerably.

- **SOP-20 bottom**

The bottom part of SOP-20 exhibits the hiatus and, therefore, the lower part is expected to be strongly ^{14}C-depleted. Two survey scans covering 13 mm were performed. The first scan was conducted from bottom to top (violet squares) with a scan velocity of 25 μm/s and the second scan from top to bottom (blue circles) was performed at 35 μm/s. For both scans the integration time was set to 30 seconds and the overall measurement time of the scans were 6 and 9 minutes. The spatial resolution of the first scan is 730 μm and of the second scan 1000 μm. The χ^2_{red} was calculated for the two scans yielding between 4, which is not within the 95 % confidence limits.
Carry-over is apparent when comparing the two scans at the growth stop of the stalagmite between a dft of 55 and 57 mm. When scanning from old to young the $F^{14}C$ just before the step is lower compared to the scan from young to old. This can be caused by the older layers ablated before and mixing into the signal. For the same reason, the $F^{14}C$ of the young part after the growth stop is not immediately reached. The scan from young to old behaves in the opposite way: the young part with a comparably high $F^{14}C$ mixes into the signal from the old layers after the step causing an elevated signal. The χ^2_{red} was re-calculated, this time neglecting the data points at the step. A value of 0.9 was obtained, which now lies within the 95 % confidence limits.

Combining the individual scans in a composite record

The LA derived ^{14}C-data from the individual scans performed on stalagmite SOP-20 is summarized in Figure 6.3. For the top scan, the shifted data with the optimized χ^2 is taken. For the middle part, data with low currents and unstable $^{13}C/^{12}C$-ratio is excluded and for the bottom part the values towards the edges that exhibited high uncertainties and low ion currents are not considered. Furthermore, the conventional data is depicted. As expected, a continuous drop over the first 55 mm is observed, reflecting the continuous growth of sample during the Holocene and showing the ^{14}C decay. The principal trend

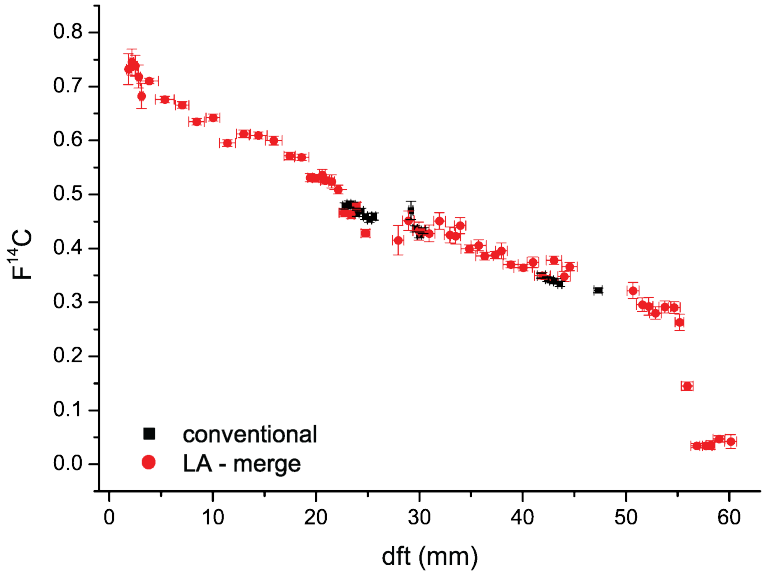

Figure 6.3: Summary of the individual measurements performed on the three sections of stalagmite SOP-20. Red circles correspond to LA-AMS-derived data and black squares to conventionally derived $F^{14}C$-values.

is in the agreement with the conventional ^{14}C data. The overall measurement time for the entire record is approximately 3 hours with a measurement precision between 0.7 and 2.5 % for the samples between 5 and 25 mm. For the older samples the relative error ranges between 2 and 3 % and for the oldest samples below a dft of 55 mm it is larger than 10 %. The spatial resolution ranges from 0.4 to 1.6 mm. Creating a record conventionally with 65 data points would take more than 8 working days.

Modeling the washout behavior of the LA-cell

If the washout time of an LA-cell is not fast enough to ensure that discrete pulses are transported into the ion source while a scan is performed, an overlap of the signals generated from different sample areas will occur, which results in a loss of spatial resolution. Numerous attempts have so far been made to establish deconvolution procedures for LA-derived data (Bleiner and Günther, 2001; Plotnikov et al., 2002; Bleiner et al., 2005). Van Malderen et al. (2015) set up a post-acquisition iterative deconvolution procedure, which allowed to to increase the spatial resolution by a factor of three. Because the repetition rate applied in LA-AMS analysis is approximately 200 Hz, with scan velocities on the order of

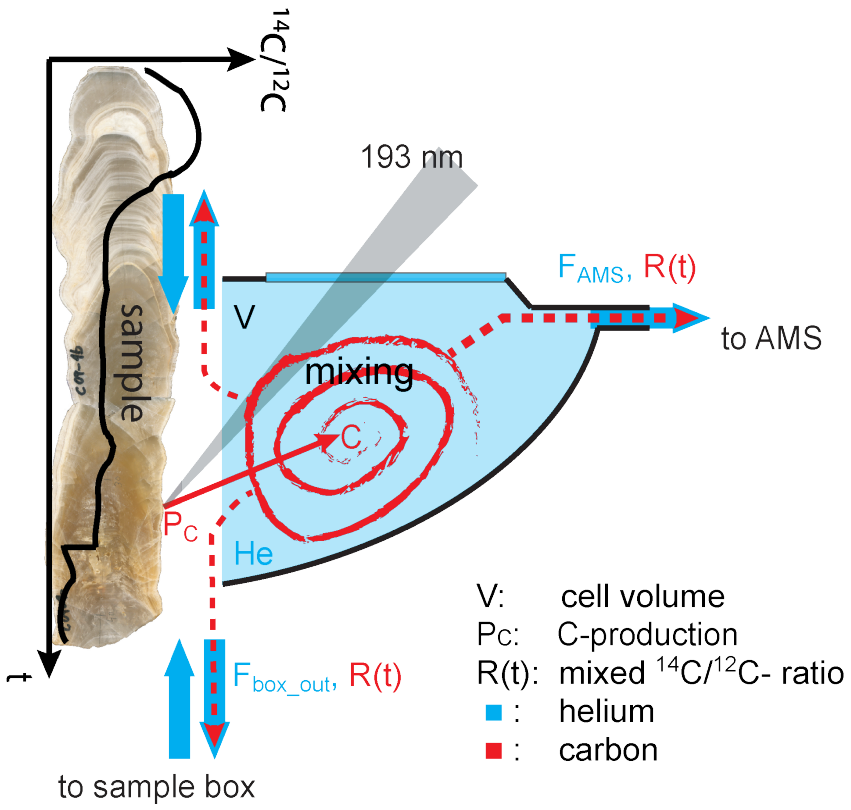

Figure 6.4: Schematic overview of the processes happening inside the LA-AMS cell. C with a time dependent $^{14}C/^{12}C$-ratio is produced by LA (P_C, red solid arrow). Diffusion inside the cell head causes mixing, which results in an overlap of the LA-generated gas from different growth layers. The mixed gas has a $^{14}C/^{12}C$-ratio (R(t)) and is transported out of the cell (red dashed arrows) at the outlet (F_{AMS}) and to the sample box (F_{box}) by the carrier gas (blue arrows).

20 μm/s, approximately 1200 pulses are fired within 6 sec. This is equal to the washout time estimated for the LA-AMS-cell (Section 5.2.2) in which a distance of 230 μm is scanned (including the spot width of 110 μm). The CO_2 generated from these 1200 pulses covering an area of 230 x 680 μm^2 will mix in the cell yielding a convoluted signal. This is especially pronounced, when analyzing samples with large $F^{14}C$ differences, because for smaller changes the convolution is negligible compared to the current measurement precision.
The bottom section of the SOP-20 comprises a growth stop covering more than 300,000 years, which is ideally suited to establish a mixing model. In Figure 6.4 a scheme of the LA-cell, as well as He (blue) and C (red) gas flow rates are shown. Several assumptions based on the results of Section 5.1.4 were made (note: in the following, C represents carbon that is present in the form of CO_2 gas). Approximately 6 μg/min of C are produced (red solid arrow, P_C) by the laser with a $^{14}C/^{12}C$-ratio that changes with time as the laser scans across the sample. The ablated C that stems from neighboring layers of the carbonate record with different $^{14}C/^{12}C$-ratios mixes in the cell and forms a time dependent

ratio R(t). Approximately 50 % of this mixture is transported by the carrier gas (He) into the AMS at a gas flow rate of 1.5 mL/min (F_{AMS}) and roughly the same amount of carbon diffuses into the sample box (F_{box}). In order to simulate the CO_2 diffusion and for simplification, the loss will be treated as an advective flow similar to a leak. This implies a second simplification, i.e. that CO_2 previously lost into the sample box, flowing back into the cell head is not considered. The two flow rates (F_{AMS} and F_{box}) will be considered as one total outflow ($F_{out} = F_{AMS} + F_{box}$) of 3 mL/min. The volume of the cell (V) is approximately 600 μL.
First, the exchange coefficient a, which relates the cell volume V with the exchanged volume per unit time, is calculated according to:

$$a = \frac{F_{out}}{V} \; [s^{-1}] \tag{6.2}$$

The ^{12}C and ^{14}C production will be treated separately:

(i) **^{12}C production**
The number of ^{12}C atoms present in the LA-cell (referred to as C_{12}), which is a function of time, is calculated. The number of ^{12}C atoms is assumed to be constant after a certain time span in which the amount is building up. A differential equation describing the constant production and exchange of the ^{12}C can be set up:

$$\frac{dC_{12}}{dt} = -a \cdot C_{12} + P_{12C} \tag{6.3}$$

where P_{12C} represents the ^{12}C production rate. The analytical solution of Equation 6.3 is

$$C_{12}(t) = \frac{P_{12C}}{a} \cdot (1 - e^{-at}) \tag{6.4}$$

The steady state value $C_{12,equ}(t > t_{equ}) = \frac{P_{12C}}{a}$, where t_{equ} represents the time after which equilibrium is reached, is used for the following calculations.

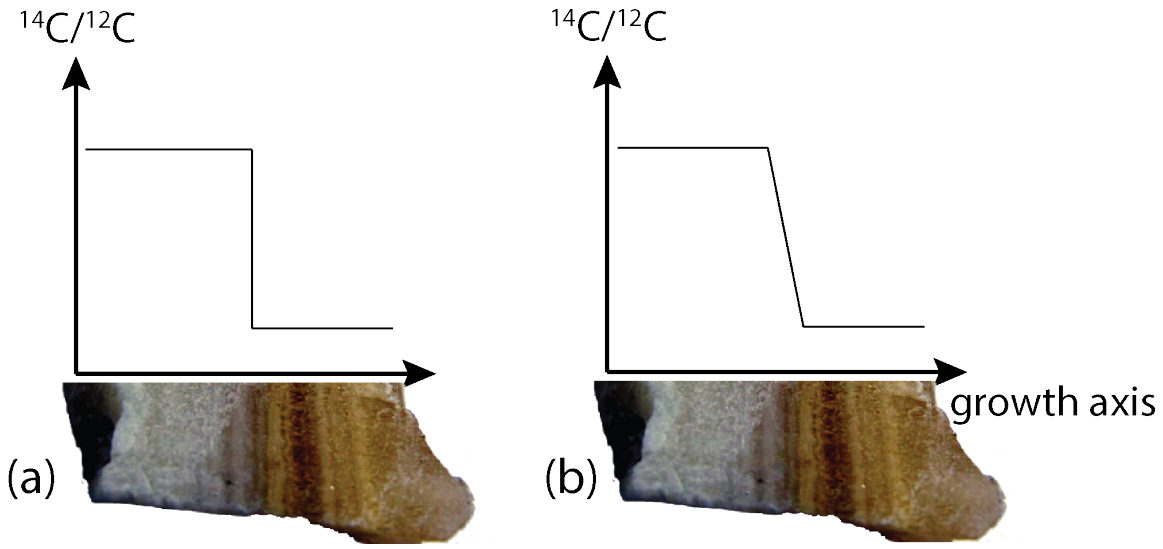

Figure 6.5: Two cases considered for the LA-AMS deconvolution model. (a) The growth stop is an 'ideal' step, (b) the growth stop has a finite width and the decrease is assumed to be linear.

(ii) **^{14}C production**
The number of ^{14}C atoms present in the LA-cell (referred to as C_{14}) is not constant over time and, therefore, an iterative approach is selected.

$$dC_{14} = (P_{14C}(t) - a \cdot C_{14})\Delta t \tag{6.5}$$

$$C_{14}(t+1) = C_{14} + dC_{14} \tag{6.6}$$

where dC_{14} corresponds to the change in ^{14}C atoms per time step Δt, P_{14C}(t) to the time dependent production rate of ^{14}C atoms and C_{14} to the amount of ^{14}C atoms present in the LA-cell.

Initially, it is assumed that the growth stop corresponds to an 'ideal' step, i.e. its width is 0 mm (Figure 6.5 (a)). Accordingly, a step function is overlaid to Equation 6.5. The calculation is performed for the scan from 'bottom to top' and for the reversed one.

(iii) **Combining ^{12}C and ^{14}C**
The ratio R(t) is formed by dividing C_{14}(t) by C_{12}(t>equ) = $\frac{P_{12C}}{a}$ and the results are integrated using the same time intervals that were applied to the measured data.

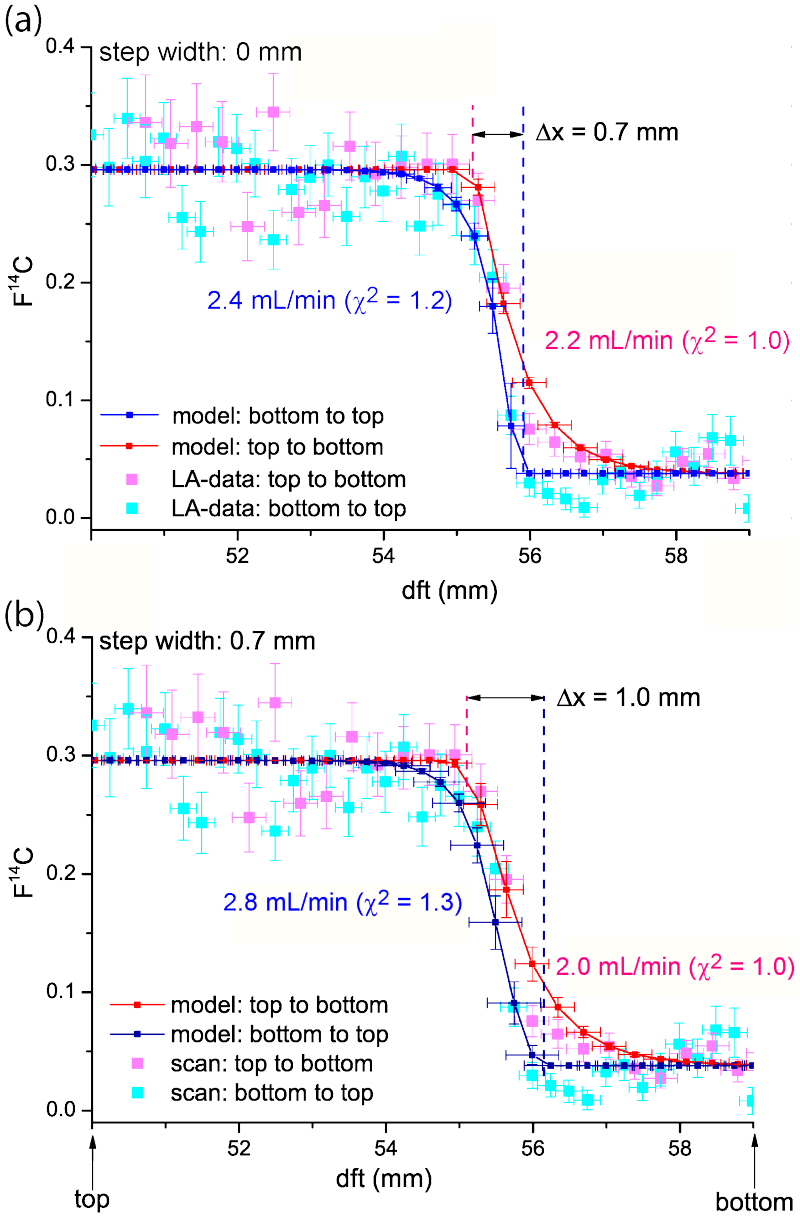

Figure 6.6: Comparison of the modeled and measured data for (a) an 'ideal' step and (b) for a continuous step. Large symbols represent the measured data for the two scan directions. Small and dark symbols connected by a trendline represent the modeled data. The total gas flow rate F_{out} for both sub-scan for the optimum χ^2 are given. In both cases, the step width derived from the modeled data is larger than the step width of the input function. Details can be found in the text.

The reduced χ^2 comparing the modeled and measured data for both sub-scans is calculated and optimized (i.e. set as close as possible to 1) by varying the flow rate F_{out}. The results are depicted in Figure 6.6 (a), where the light blue circles and the light pink squares correspond to the measured LA-data. The modeled data is represented by the smaller and dark symbols with the trendlines. For the scan from 'bottom to top' the modeled optimum flow rate was found to be 2.2 mL/min with a reduced χ^2 of 1.0. For the opposite scan the optimum modeled flow rate is 2.4 mL/min with a reduced χ^2 of 1.2. The flow rates obtained for the two scans are on the same order but slightly lower than the flow rate of 3 mL/min initially assumed. The locations of the step for both scans derived from the model are indicated in Figure 6.6 (a) by the vertical dashed lines (blue for the scan from 'bottom to top' and pink for the scan from 'top to bottom'). The two lines do not overlap, as expected, but exhibit a distance of 0.7 mm. This is an indication, that the step on the sample is not ideal as assumed but has a finite width.
Consequently, the ^{14}C input function of the model was changed assuming a step width of 0.7 mm (Figure 6.5 (b)) and the results are depicted in Figure 6.6 (b). A flow rate of 2.8 mL/min is found for the scan from bottom to top with a reduced χ^2 of 1.3 and a flow rate of 2.0 mL/min for the opposite scan with a reduced χ^2 of 1.0. The position of the step for each scan is indicated in the Figure 6.6 (b), yielding a spatial difference of 1.0 mm. The difference between the flow rates is now even larger than in the first case.
An alternative explanation for the step width found in the first case, is an improper alignment of the laser tracks relative to the growth layers of the sample. They were not perpendicular to each other, but tilted at an angle of approximately 3° - 5°. Taking into account that the two tracks were positioned at a distance of 2 mm, an artificial step width of approximately 0.1 mm - 0.2 mm is yielded. Therefore, the step width in the sample can be assumed to be approximately 0.5 mm. Further calculations are necessary to confirm this assumption.

A simple model has been developed that approximates the mixed $^{14}C/^{12}C$-ratio produced by a LA-scan across a sample with layers of different ^{14}C-content. For simplicity in the model only mixing in the LA-cell volume is considered and diffusion and mixing processes occurring in the capillary are neglected. A χ^2-fit was used to match modeled and measured data and to optimize gas flow rates. Values for F_{out} were found to range from 2.0 to 2.8 mL/min, which is somewhat lower than the assumed value of 3 mL/min. Since the magnitude of the gas flow rate into the ion source is better known ($F_{AMS} \sim 1.5$ mL/min) than the loss into the sample box, it is concluded that the loss is lower than the initially assumed 1.5 mL/min. Routine measurements have shown that the gas flow rate into the ion source and the loss into the sample box vary from day to day, due to small changes (several 1/100 mm up to 1/10 mm) of the gap between the inset and the sample surface (compare Section 5.1.4). It is concluded, that the gas flow rates derived from the model need to be determined for every measurement day. A standard comprising an ideal step

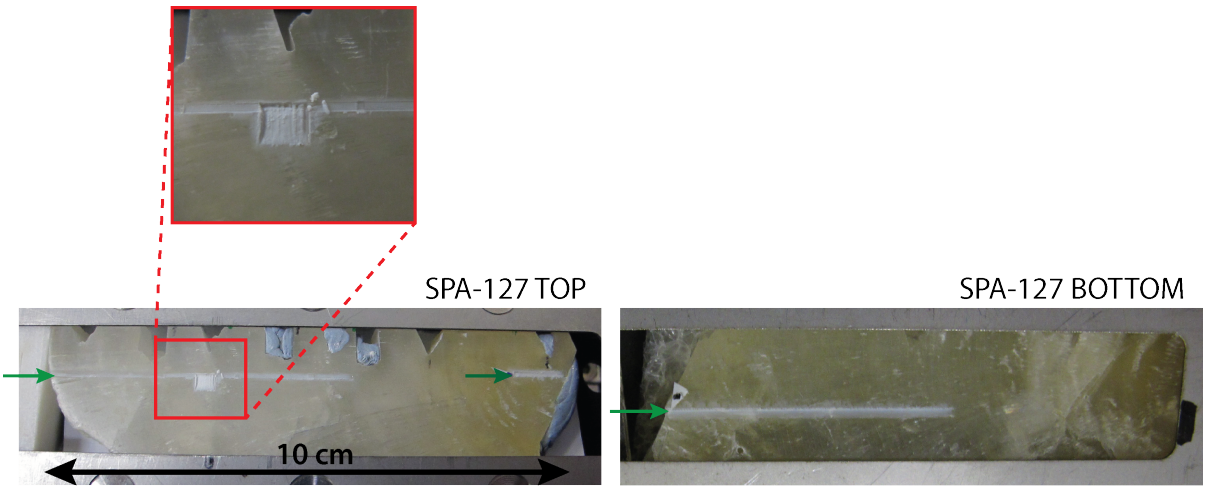

Figure 6.7: Pictures of the top and bottom section of the SPA-127. Laser tracks from survey scans are visible on both pieces and indicated by green arrows. The red box shows the location of the precision scan, which is also depicted in the enlarged inset.

by combining a marble sample with a modern sample and measuring this standard when performing LA-AMS analyses would allow to establish a deconvolution model for each measurement in order to correct for washout effects.

6.1.3 Stalagmite SPA-127

In order to investigate if the hypothesis of carbonate formation due to oxidation of sulfides at Spannagl cave is valid, LA-AMS analysis is applied to this speleothem. For the conventional ^{14}C-analysis of speleothem carbonates a large amount of samples would be necessary to resolve the short range changes in the C isotope composition.

The SPA-127 covering more than 15 cm in length was cut into two pieces, labelled 'top' and 'bottom' (Figure 6.7). First test measurements have been performed on the two sections of the SPA-127. On the top of the upper section a survey scan consisting of six sub-scans was performed (open squares and solid circles in Figure 6.8 (a)) with an overall measurement time of 50 minutes. For this test the scans were performed relatively far away from the stable isotope track on the half of the stalagmite slab previously dated by U/TH. The measurement parameters of all scans performed on SPA-127 are summarized in Table 6.2. The data evaluation was performed applying different integration patterns: the red and green open squares correspond to an integration time of 60 s, resulting in a spatial resolution of 1.4 mm and a measurement precision on the order of 3.5 %. The integration

Table 6.2: Measurement settings and results for SPA-127

symbol in Figure 6.8	**laser parameters**			**data evaluation**		
	frequency	fluence	scan velocity	integration time	spatial resolution	precision
unit	Hz	J/cm^2	μm/s	s	μm	%
open squares	200	1.0	20	60	1400	3.5
solid circles	200	1.0	20	30	800	4 - 5
solid diamonds	200	1.0	10	30	400	5 - 6
solid triangles	250	1.5	20	30	800	4.5
orange stars	200	1.0	80	100	200	2.5

time of the solid circles (orange, pink, light and dark blue) is 30 s, resulting in a spatial resolution of 0.8 mm and a measurement precision between 4 and 5 %. Between a distance from top of 24 and 27 mm a precision scan was performed (Δx = 3.8 mm, Δy = 2 mm, δx = 50 μm) with a lateral velocity of 80 μm/s represented by the black stars. The integration time was 100 s resulting in a spatial resolution of 200 μm and a measurement precision of 2.5 %. An enlargement of the section with the precision scan is shown in Figure 6.8 (b). Both survey scans (black and brown circles) are in good agreement with the precision scan exhibiting the same ^{14}C signal.A survey scan was performed at the bottom of the top part (purple diamonds in Figure 6.8 (a)). The integration time is 30 s and the resulting spatial resolution is 400 μm with a measurement precision between 5 and 6 %. The measurement time was 15 minutes. Two survey scans were performed on the bottom part of SPA-127 (solid triangles) with an integration time of 30 s resulting in a spatial resolution of 0.8 mm and a measurement precision around 4.5 %. The two sub-scans covered a distance of approximately 33 mm resulting in a measurement time of 30 minutes.

The overall measurement time of all survey scans depicted in Figure 6.8 (a) was 95 minutes covering a distance of 90 mm. For the various sub-scan, different integration times and thus different spatial resolutions and measurement precisions were achieved, showing that the LA-AMS method offers a great flexibility with respect to the data evaluation. An overview is given in Table 6.2. As the data shown here were produced in the framework of a first test, allowing to establish a quick impression about the ^{14}C content of the SPA-127, scans in only one direction were performed. In order to verify the quality of the LA-AMS data and to establish a complete ^{14}C record of the SPA-127, further measurements with scans facing in both directions are planned. Precision scans will be performed in regions where the ^{14}C signal shows large variations, i.e. between a dft of 15 and 35 mm.
The start and end point of all subscans are in good agreement and the general trend of decrease in ^{14}C with increasing dft, reflecting the decay of ^{14}Cis visible. Furthermore, the good agreement between the precision scan and the survey scans suggests, that the

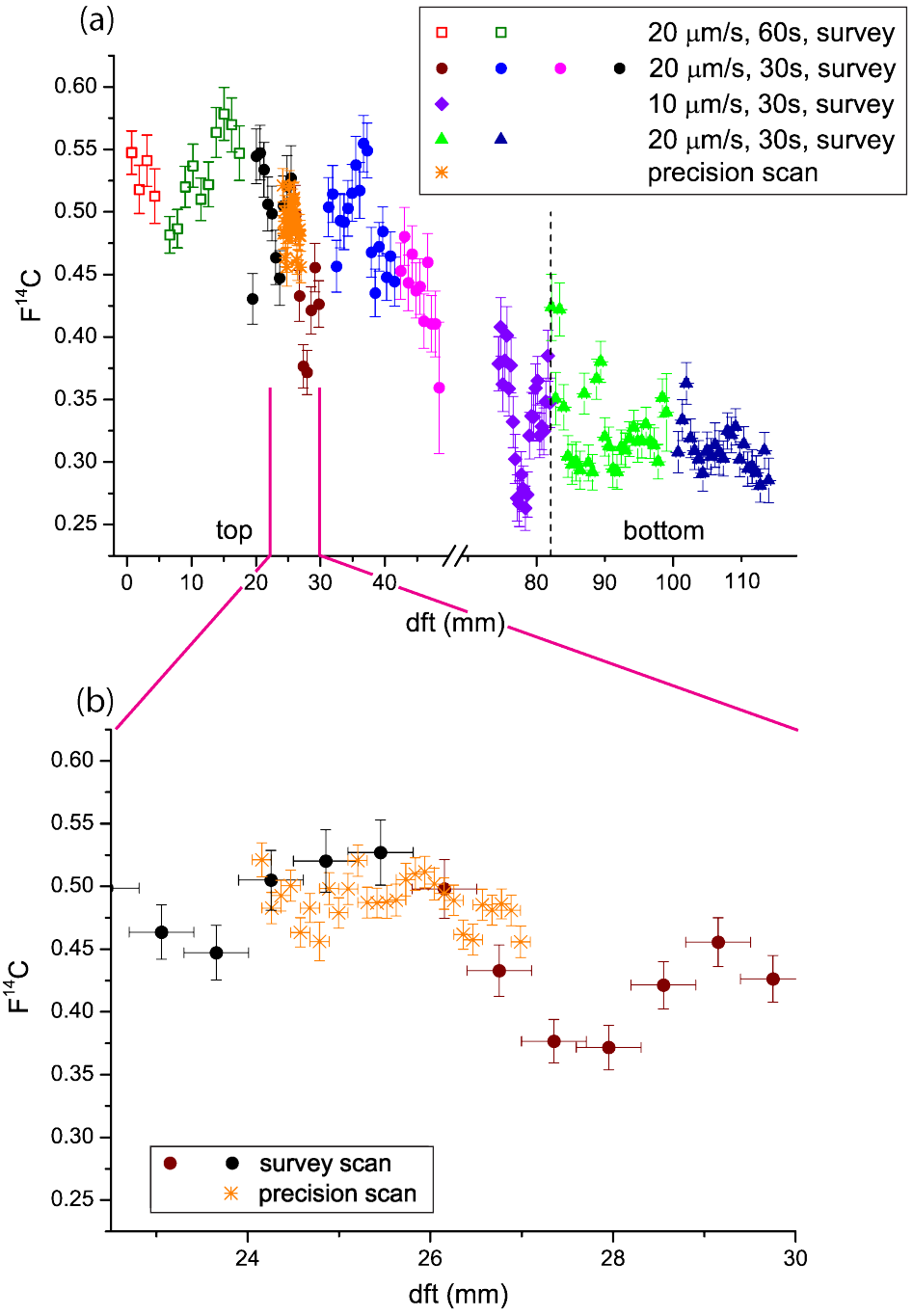

Figure 6.8: (a) Survey and precision scans performed on the two sections of the SPA-127. The dashed vertical line represents the cutting point. Symbol shapes represent measurement settings and colors individual sub-scans. (b) Enlargement of the section where the precision scan was performed. For comparison, also the survey scans at this region are shown.

LA-derived ^{14}C-data from the test measurements are of good quality despite the fact that the scans faced only into one direction. Large variations in the F^{14}Cacross the entire record can be observed. It is very likely that these variations reflect strong changes in the dcf, which should also be visible in the stable C isotope signature. However, a first comparison of the LA-data with the δ^{13}C could not confirm this assumption on the section studied here. This could be a matter of the alignment between the stable and cosmogenic C isotope tracks and the curved growth behavior of stalagmites. Therefore, as a next step, LA-AMS measurements are planned to be performed right next to the stable isotope track to ensure proper alignment of both data sets.

6.2 Marine carbonates

Besides speleothems, the LA-AMS method has also been applied to marine carbonates, such as corals, shells and fish ear stones (otoliths). In the following section the analysis of two coral samples, two shells from different species (Arctica islandica and pearl oyster) and an otolith will be presented. A pearl oyster sample is used to compare the normalization procedure of LA-AMS measurements using the OxII and CSTD standard.

6.2.1 Coral samples

Two bamboo corals were analyzed with LA-AMS yielding ion currents on the order of 13 μA, which is slightly below ion currents achieved for conventional gas measurements.

Bamboo coral DR241300

Bamboo coral- DR241300 has been studied by comparing scans on two different sections of the specimen. For this, the sample was cut in two sections, labeled coral-1 and coral-2 that were subsequently embedded in epoxy resin. On each subsample two scans were performed as shown in the right of Figure 6.9, where the arrows indicate the scan direction. Each scan covered the same growth period but a different length on the coral. Therefore, normalized scan distances are used. The measurement parameters were as listed in Table 6.1 except for the repetition rate of 150 Hz and the scan velocity, which was varied between

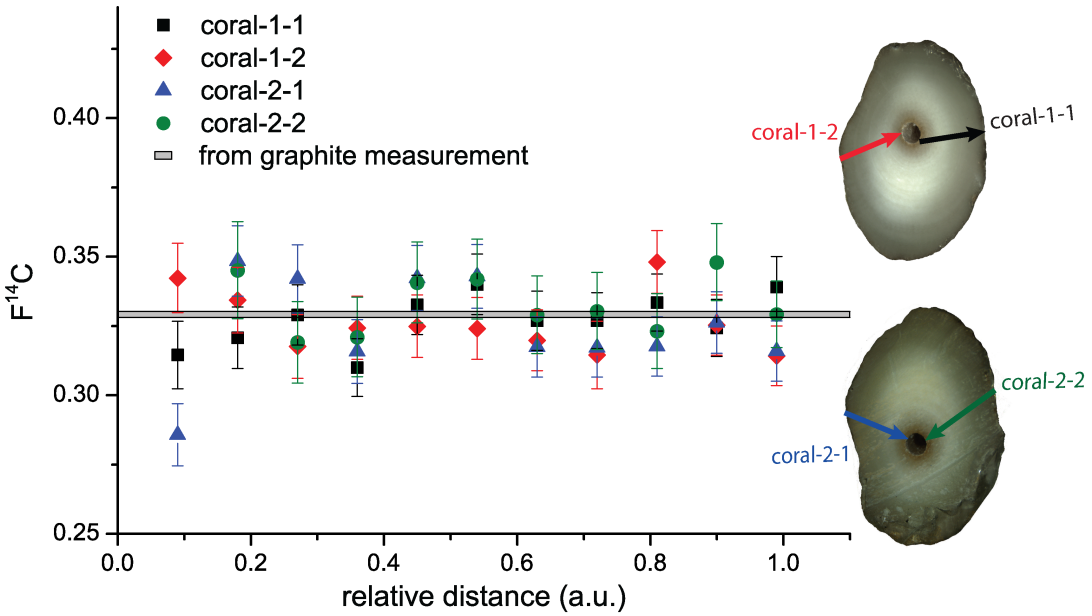

Figure 6.9: Comparison of four scans on two sections of a bamboo coral with the mean $F^{14}C$ value across the growth axis from conventional graphite measurements (grey band). The arrows indicate where the scans were performed and the arrow heads point into the direction of scan.

8 and 12 μm/s to ensure measurement times on the order of 10 minutes corresponding to the typical lifetime of the sputter targets at the day of the measurement. The spatial resolution of the different scans ranges from 450 - 650 μm and the uncertainty of each subsample corresponding to the counting statistics is on the order of 2 %. A reduced χ^2-test was performed with all scans confirming that the means of the different scans are not significantly different (95 % conf. limit). The mean $F^{14}C$ value of all four scans is 0.326 $\pm$ 0.002, which is in very good agreement with the value of 0.330 $\pm$ 0.001 derived from conventional graphite measurement.

Bamboo coral 36252

Two precision scans in opposite direction were performed on coral 36252. The growth of the layers is concentric as shown in Figure 6.10 (a), where the black mark represents the center of the coral. For the scan directed towards the center, the vertical displacement was set to 4 mm at the outer region of the coral (red box in Figure 6.10 (a)) in order to increase the measurement precision, while scanning towards the center (solid blue box in Figure 6.10 (a)) it was reduced to 2 mm to minimize scanning across different growth layers within one zig-zag step. On the backward scan, the vertical displacement covered

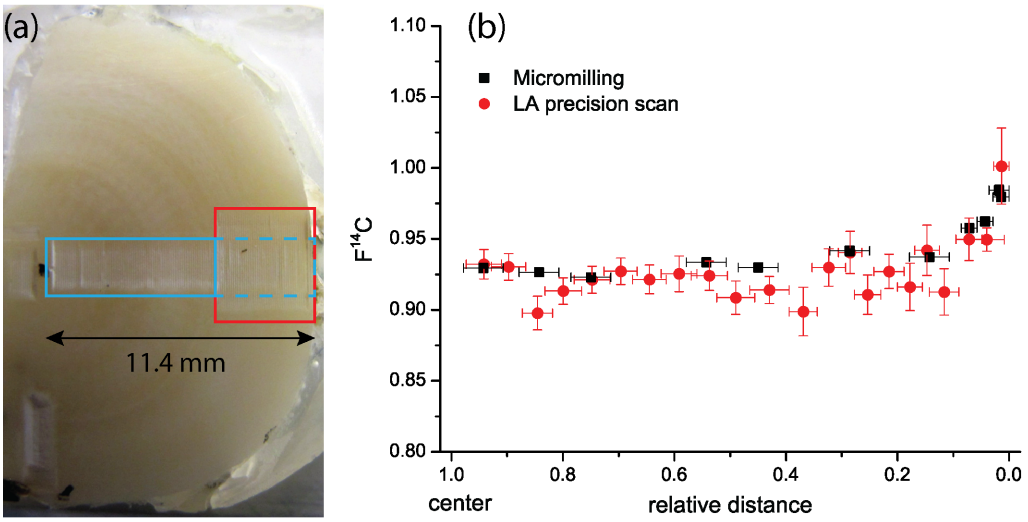

Figure 6.10: (a) Laser tracks produced from LA-AMS measurements on a cross-section of a bamboo coral (36252). The center of sample is marked with a black dot. At the outer region where the growth layers have a larger radius, the vertical displacement covered 4 mm (red box) in order to increase counting statistics. Towards the center, the vertical displacement was reduced to 2 mm (solid blue box) to minimize mixing of different growth layers within one zig-zag step. On the back scan (from center to the edge) the entire scan had a vertical displacement of 2 mm (solid and dashed blue box). (b) Comparison of the LA-AMS derived $F^{14}C$values with the conventional graphite measurements. The two methods were performed on two sections of the coral of different width and, therefore, the scanning distance is expressed as a relative distance with zero being the outer edge and 1 the center.

2 mm along the entire track (solid and dashed blue box in Figure 6.10 (a)). The precision scan parameters were ($\Delta x = 11.4$ mm, $\Delta y = 4(2)$ mm, $\delta x = 100\,\mu$m). For the scan in the red box the scan velocity was 280 μm/s and for the blue one 150 μm/s. The ^{14}Cresults are shown in Figure 6.10 (b), where the red circles represent the LA-AMS data and correspond to integration times between 3 and 5 minutes resulting in an overall measurement time of approximately 2 hours. The integration time was chosen rather long in order to achieve a measurement precision of 1 - 2 %, which is necessary to resolve the weakly pronounced bomb peak in this sample. Only the topmost sample has a precision of 3 % caused by low ion currents when starting the scan towards the center and due to a lower integration time. The spatial resolution is on the order of 500 - 700 μm except for the topmost sample with 300 μm. Conventional ^{14}C data (black squares) stems from a different section and, therefore, scan distances are expressed as a fraction of the total distance and referred to as 'relative distance'. The bomb peak revealed by conventional analysis was reproduced by the LA-AMS data showing a $F^{14}C$increase of 0.06. The distinct advantage of the LA-AMS analysis in this case is analysis time: analyzing one conventional sample with a spatial resolution of 500 μm takes approximately 10 times longer than the time that is required for the measurement of one LA-AMS derived data point at the same spatial resolution.

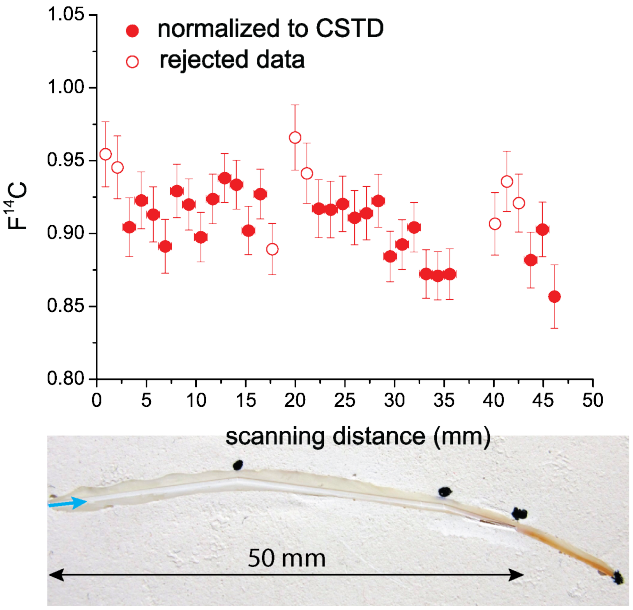

Figure 6.11: Results obtained for the Arctica islandica specimen with LA-AMS. The scan was performed from the youngest part (scanning distance = 0 mm) towards the older part (scanning distance = 45 mm). The laser track indicated by the blue arrow corresponds to the survey scan on the Arctica islandica. The sample was embedded in gypsum.

6.2.2 Other marine carbonates

A fish ear (otolith) and two shell samples were analyzed by LA-AMS. All three samples are expected to exhibit the bomb signal, however, no conventional data for comparison is available. Both shell samples yielded ion currents on the order of 18 μA and for the otolith ion currents of 13 μA were achieved.

Arctica islandica (shell)

A survey scan covering 4.5 cm was performed on the shell with a scan velocity of 20 μm/s and an overall analysis time of 40 minutes. In Figure 6.11 the results are depicted: the top 30 mm exhibit a $F^{14}C$of 0.92 $\pm$ 0.01, while the average value of the older part is lower with a $F^{14}C$of 0.88 $\pm$ 0.02. Since no modern $F^{14}C$is found in this sample, it is concluded that the Arctica islandica stopped growing before the onset of the bomb testing period. The age of the sample can be estimated when calibrating the $F^{14}C$values estimated using

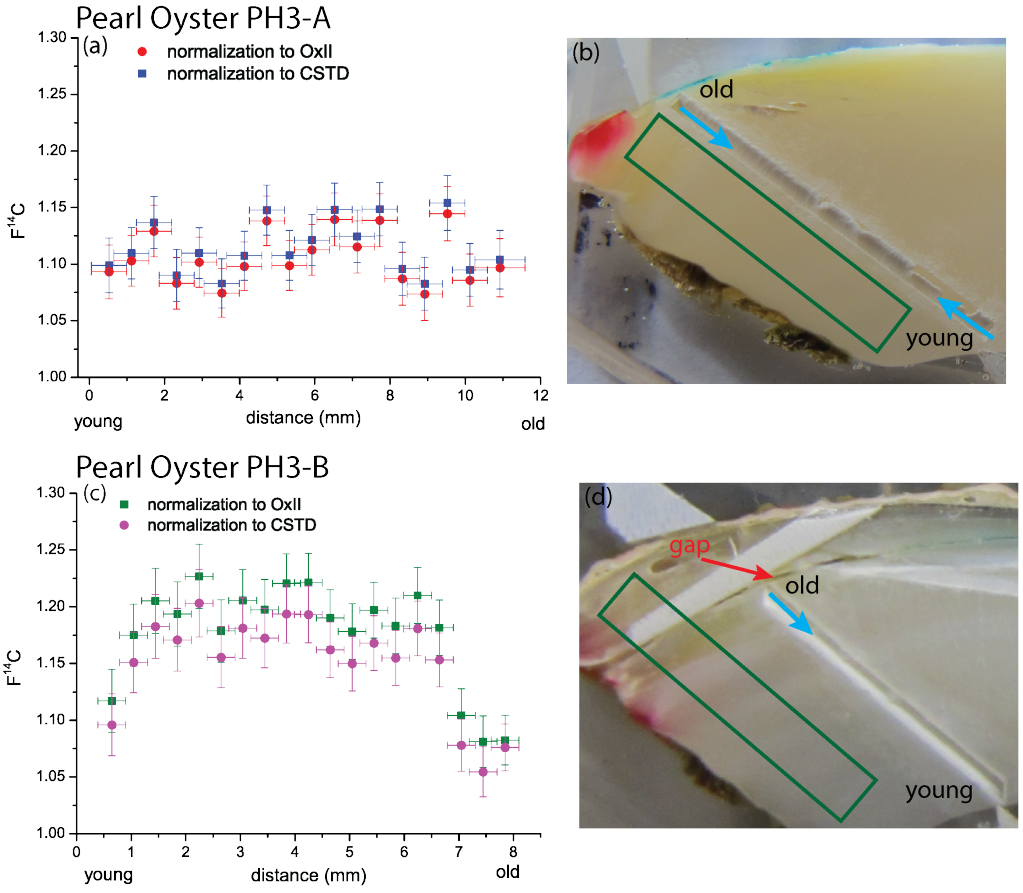

Figure 6.12: (a) $F^{14}C$ signal derived from LA-AMS analysis of an oyster sample (PH3-A). On the x-axis the scanning distance from young to old is shown. (b) Picture of the laser track across oyster PH3-A. (c) $F^{14}C$ signal for oyster section PH-3B and (d) the corresponding laser tracks.

the marine radiocarbon reservoir correction established by Butler et al. (2009). This yields an age of approximately 200 to 500 years for the youngest part and 500 to 900 years for the old part. Due to these large uncertainties, the lifetime of the specimen maybe as high as 700 years. Butler et al. (2013) had shown that ages of 300 years have frequently been observed for this species. The oldest Arctica islandica dated so far had a lifetime of 507 years. Since the specimen was found in a very good condition at the beach, it is suspected that the shell remained at the site were it had lived for several hundred years, until it was detached and washed up to the beach, shortly before it was found.

Investigating the normalization procedure for LA-AMS using a pearl oyster

Two sections of the pearl oyster (PH3-A and PH3-B) were analyzed by LA-AMS. Two stacked survey scans performed in opposite directions on PH3-A covered a distance of 11.2 mm with a scan velocity of 20 μm/s yielding a measurement time of approximately 20 minutes. The integration time is 30 s, the spatial resolution is approximately 0.9 mm yielding a measurement precision of 2 %. The results were normalized to the Ox-II gas standard, which is the standard procedure for LA-AMS measurements and has been confirmed to work well in most cases (see samples described above and Section 5.2.3). In addition, the LA-AMS-CSTD standard (pressed carbonate powder; see Section 4.2) was measured and used for normalization. The results of the two scans normalized to either standard are depicted in Figure 6.12 (a). The relative difference between the two data sets is 0.8 %, confirming that within the measurement uncertainties both standards can be used for normalization of the data. The laser tracks are shown in Figure 6.12 (b), where the blue arrows indicate the scan direction.
One survey scan was performed on the oyster section PH3-B. The scan velocity was 10 μm/s, the distance covered 8.2 mm and the total measurement time 15 minutes. A measurement precision between 2 and 2.5 % and a spatial resolution of 500 μm were reached, using an integration time of 40 s. Again the data was normalized using the Ox-II and the CSTD and the two data sets are shown in Figure 6.12 (c). The relative difference between the two data sets is 2 %, which is more than twice the difference found for the analysis of the PH3-A. From the comparison of the PH3-B data with Kure Atoll $F^{14}C$ record (A. H. Andrews, NOAA Fisheries, personal communication) it can be concluded, that the data normalized with the CSTD ia a better match. So far, it is not clear what causes this difference. Possibly, measurement conditions in the ion source changed during the LA-AMS analysis of the CSTD standard and the PH3-A sample in comparison to the Ox-II measured from the GIS-box (see Section 3.3). Further studies investigating the normalization procedure using the LA-AMS standard versus normalization using the gas standard are necessary to constrain the conditions under which each standard should be used. The laser track (blue arrow) is depicted in Figure 6.12 (d) and it can be seen that the PH3-B section was of lower quality than PH3-A due to a gap (red arrow) at approximately 8 mm from the youngest part, which was most likely also filled with epoxy resin during the embedding procedure, making the LA-AMS analysis at this location difficult. Therefore, the first test measurement on this specimen covered only 8 mm.
Within the limited precision, no clear bomb peak can be seen in the record for PH3-A (Figure 6.12 (a)) and the average $F^{14}C$of the data set of 1.11 $\pm$ 0.02. In the case of PH3-B a drop from a $F^{14}C$ of 1.17 $\pm$ 0.02 to 1.07 $\pm$ 0.01 suggests that the bomb peak is reached at a distance of approximately 6.5 mm (Figure 6.12 (c)). Since this drop is close to the gap it cannot be excluded that a contamination with epoxy is the reason for this depletion. At the youngest part of the sample a drop to a $F^{14}C$ of 1.10 is observed. This could be caused by a contamination with epoxy or it is part of the bomb peak. Further precision scans are

planned on the optimum section of each specimen (green rectangles in Figure 6.12 (b) and (d)). Furthermore, five samples for conventional graphite AMS analysis have been taken (A.H. Andrews, NOAA Fisheries, personal communication) at PH3-B in order to clarify, whether the observed signal represents the bomb peak or an epoxy-contamination.

Applying LA-AMS to an otolith

Two survey scans on top of each other facing in opposite direction were performed on the otolith sample. The lateral velocity was set to 20 μm/s and both scans covered a distance of 5.6 mm. The laser tracks are depicted in 6.13 (a) marked by the blue rectangle. The data was normalized using the CSTD. Both scans exhibit an abrupt increase in the $F^{14}C$, assigned to the onset of the bomb peak. The onset of the two scans exhibit a spatial shift of approximately 5 s most likely caused by cross contamination (compare Figure 6.13 (b)): for the scan from young to old, the onset is found at 2.4 mm and for the reversed scan at 2.2 mm. After correcting for this, the two scans were averaged and the results are shown in Figure 6.13 (c). The integration time is 20 s corresponding to a material uptake of 40 μg per data point. The total measurement time is 10 minutes and the overall material consumption is 1.1 mg. The spatial resolution is on the order of 340 μm and the measurement precision ranges from 3 - 5 %. The younger part has a modern $F^{14}C$ with a mean of 1.11 $\pm$ 0.04 and the pre-bomb region starting at a distance of about 2 mm has a mean $F^{14}C$ of 0.97 $\pm$ 0.04. It is desirable to obtain higher measurement precisions in order to better resolve the bomb peak in this sample. Currently, this is limited by the amount of sample material available, which inhibits to perform a precision scan on the sample. However, additional survey scans are planned, which in combination with the present data, could increase the measurement precision.

6.3 Summary

The LA-AMS method has been applied to several carbonate samples exhibiting different ^{14}C signatures, such as the bomb peak with different attenuation or a growth stop. The applicability to various materials and its potential with regard to spatial resolution and measurement precision were investigated. A spatial resolution down to 100 μm and a precision of better than 1 % can be obtained. Ion currents for aragonite and calcite samples were on the same order of magnitude and comparable to those obtained for the GIS setup.

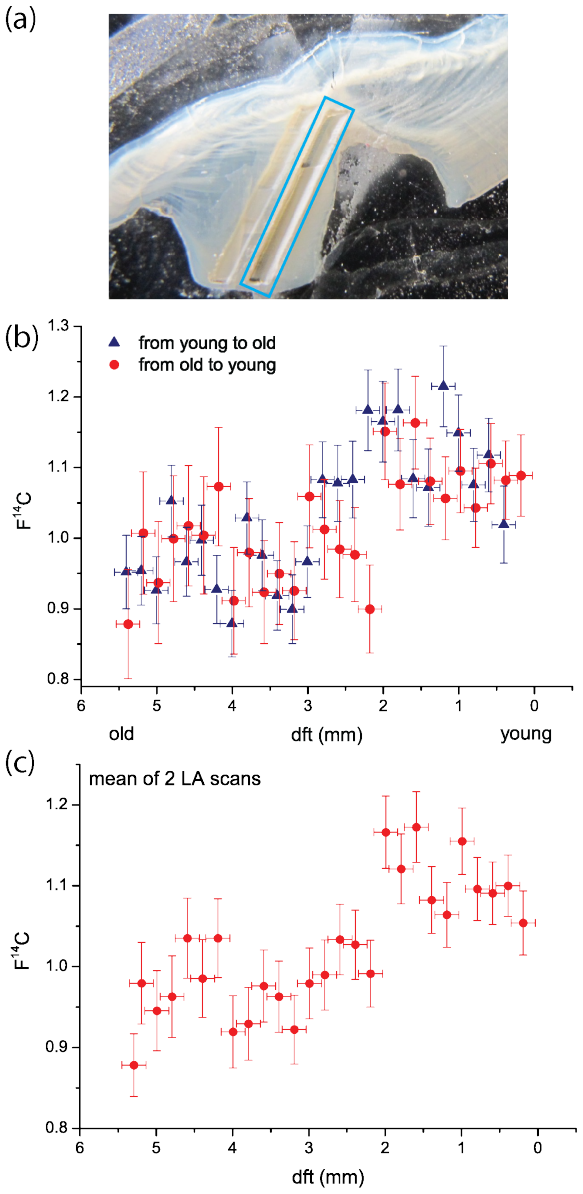

Figure 6.13: (a) Laser tracks produced by LA-AMS analysis of an otolith sample are indicated by the blue rectangle. The length of the scan is 5.6 mm. (b) ^{14}C signal corresponding to the two LA-AMS scans performed on the otolith RS-04. The two scans appear to be shifted as observed previously. (c) ^{14}C signal found in an otolith by LA-AMS analysis. The youngest part of the otolith is located at a scanning distance of 0. At approximately 2 mm the onset of the bomb peak can be seen.

Table 6.3: Overview of the different samples and sample materials as well as their expected and LA-AMS derived $F^{14}C$

Sample label	Sample type	known $F^{14}C$ (conventional)	Measured $F^{14}C$ (LA-AMS)
ER-77	stalagmite (calcite)	0.88 - 1.19 [1]	0.81 - 1.30 [a]
BU-4	stalagmite (calcite)	0.88 - 1.00 [2]	0.82 - 1.04 [a]
SOP-20	stalagmite (calcite)	—	0.74 - 0.02 [a]
SPA-127	stalagmite (calcite)	—	0.58 - 0.26 [a]
coral-DR241300	bamboo coral (calcite)	0.330 ± 0.001	0.326 ± 0.002 [a]
coral-36252	bamboo coral (calcite)	0.92 - 0.98	0.90 - 1.00 [a]
Arctica islandica	shell (aragonite)	—	0.88 - 0.92 [a]
PH3-A/B	pearl oyster (calcite)	—	1.05 - 1.20 [b]
RS-07	otolith (aragonite)	—	0.88 - 1.17 [b]

[1] Fohlmeister et al. (2011)
[2] Fohlmeister et al. (2012)
[a] normalized to OxII
[b] normalized to CSTD

Two stalagmite and coral samples with known ^{14}C content were analyzed and the conventional data was reproduced within the uncertainties. When comparing the ^{14}C range from conventional measurements with the range obtained by LA-AMS (Table 6.3) it can be seen, that LA-AMS measurements in all cases yielded a larger range. Due to the higher spatial resolution achieved with LA-AMS, more detailed insight in the ^{14}C content within the carbonate record can be gained. The expected ^{14}C trend of a stalagmite from the Holocene, suggested by U/Th-dating, was confirmed by LA-AMS measurements: a continuous drop in the upper section and a hiatus in the lower section were revealed. A sample with a 'perfect' ^{14}C step can be used to model carry-over and help to establish a deconvolution procedure. LA-AMS analysis of a stalagmite with remarkably large $\delta^{13}C$-variations from a high-alpine cave was found to exhibit exceptionally large variations in its ^{14}C signature. Three marine samples with unknown ^{14}C content were analyzed: in a fish ear sample the bomb peak could be resolved. An Arctica islandica specimen did not exhibit the bomb peak, but pre-bomb ^{14}C levels. This suggests that the shell was older than initially assumed. Two sections of an oyster sample were analyzed and revealed a modern $F^{14}C$ with a few ^{14}C-depleted data points towards the older part of the samples. Whether this is the rise of the bomb peak or a contamination with epoxy needs to be clarified by precision LA measurements and conventional AMS analysis. The analysis of the oyster section PH3-B revealed that the Ox-II standard is not always the best choice for the normalization of samples analyzed with LA-AMS. So far, it is not understood what caused this and it is suggested to carry out further studies on the optimum normalization procedure for LA-AMS analysis. Generally, analysis toward the edges of samples showed to be less reliable. So far it is not understood, whether this is caused by surface contamination - for example from epoxy - or if other effects, i.e. different gas flow dynamics are responsible for this behavior.

7 Conclusion and Outlook

Conventional AMS ^{14}C analysis of carbonate samples by AMS requires time-consuming sampling and potentially contamination-prone chemical treatment. LA as a sampling technique for gas ion source AMS can overcome these drawbacks. A novel setup combining LA with AMS for the rapid online detection of ^{14}C was designed, and parameters for optimum operation were determined. Highest CO_2 conversion efficiencies were obtained using an ArF excimer laser making it the most suitable laser source for the coupling of LA with AMS. An LA-cell that allows the precise positioning of large samples relative to the laser beam and a gas-handling system that enables controlled gas flow into the ion source were designed and built. Typically, (8.1 ± 0.9) ng of $CaCO_3$ are ablated per laser pulse (equal to $(97 \pm 5)\,\mu$g $CaCO_3$ /min @ 200 Hz, 1 - 2.5 J/cm^2, 680 x 110 μm^2), and ion currents of up to 20 μA were achieved, corresponding to an overall efficiency of 5 ‰. Blank levels appeared to be independent of C^- current and slightly higher than observed during conventional gas measurements. Nominal values of certified and in-house standards were reproduced within errors.

LA-AMS was successfully applied to the ^{14}C analysis of carbonate records including stalagmites, corals, shells and fish ears. All sample materials tested yielded sufficiently high ion currents for ^{14}C measurement for both calcite and aragonite carbonates. Different scanning modes were compared with regard to measurement precision, spatial resolution, analysis time and material consumption. LA-AMS subsamples require between 0.1 - 1.5 mg of $CaCO_3$ with analysis times ranging from 20 seconds to 10 minutes, yielding a precision of 1 - 5 % and a spatial resolution between 100 μm and 1000 μm. The different scanning modes complement each other and can be combined in order to yield optimum results: a survey scan can be used to quickly identify regions of interest in a carbonate record, e.g. a growth stop or the bomb peak, and a subsequent precision scan can be applied to generate a ^{14}C record of higher precision. Performing continuous scans provides a great flexibility with regard to measurement precision and spatial resolution. In the case of weakly pronounced ^{14}C signals, as for 'bamboo coral 36252', more data can be averaged in order to increase the measurement precision, while consequently the spatial resolution is lowered. Especially the analysis of samples where only little material is available, as in the case of the otolith sample, benefit from this new technique as considerably less material is consumed. For all samples where conventional ^{14}C data were available (stalagmite ER-77, BU-4, coral-1, coral-2(36252)), the LA-AMS-derived results were in good agreement with exisiting ^{14}C records. In the case of stalagmite SOP-20, the known history obtained from other geochemical tracers was reflected in the LA-AMS data. In stalagmite SPA-127

comprising unusually strong variations in the stable C record, exceptionally fast and large ^{14}C fluctuations were revealed by survey scans. A major advantage of LA-AMS is the exceptional sample throughput that allows to quickly assess the ^{14}C content of a large number of samples. Nevertheless, it is desirable to further increase the measurement precision in order to better resolve less pronounced ^{14}C signals.

Future developments should focus on modifications that aim for

(i) a higher signal intensities in order to achieve a higher measurement precision,

(ii) a reduction of cross-talk and

(iii) an improvement of the data handling and data reduction.

(i) Higher signal intensities of the LA-AMS setup can be implemented by (1) increasing the gas transport efficiency from the ablation site to the ion source, (2) a higher absolute CO_2 production and (3) an optimization of the sputter target geometry. (1) The prototype LA-cell used in this work was optimized for a minimal gas volume in the sampling area to ensure short washout times, a rapid dynamic response and minimized carry-over of previously ablated material to avoid a loss of resolution. Even though high signal intensities have been achieved with the prototype ablation cell, there is a clear indication that a significant fraction of the CO_2 generated is lost before reaching the gas ion source due to diffusion out of the cell head. Two solutions are proposed to overcome this problem: (a) The construction of a very simple LA-cell that is moved by an external stage relative to the laser beam, comprising one compartment accepting smaller samples, to investigate its effect on transport efficiencies. Routine operation showed, that for a large fraction of the samples analyzed so far, a much smaller sample box is sufficient. At the same time, when considering the current integration times (several minutes), a slower response by doubling the ablation cell volume may be tolerable to still achieve high spatial resolution. Such a basic setup would permit to investigate the potential and the limits of LA-AMS regarding signal intensities, which could not be explored with the current setup. (b) A modified design of the present LA-cell, comprising a better sealing between the ablation volume and the sample holder, may improve the transport efficiency and therefore increase sensitivity. This should lead to a better measurement precision, reduced analysis times, and eventually a higher spatial resolution. A more powerful positioning system would allow to further reduce the gap between the sample and the insert, hence, increasing the flow resistance to LA-produced CO_2. Alternatively, LA-cell insets with different geometries and materials could be studied. (2) Higher laser fluences can be achieved with the current setup by reducing the travel distance of the beam in air or by focusing the laser on a smaller spot.

An increased laser fluence on the sample surface will result in a higher CO_2 production, but at the same time increases the fluence at the cell window. A re-design of the LA-cell and the focusing optics is necessary in order to reduce damages on the window. This could be achieved by enlarging the distance between the sample surface and the cell window. A lens with a shorter focal length would lower the fluence on the window requiring a larger entrance area and at the same time this would improve the sample observation. The absolute amount of CO_2 produced by the laser source can be increased by operating at higher fluences than the currently applied 1 - 2 J/cm^2. (3) Gas flow rates for LA-AMS measurements are more than a factor of 10 higher than for conventional gas analyses. Improving the target geometry for high gas flows and a reduction of memory effects on the same target will allow to increase the efficiency, accuracy and reliability of the present LA-AMS measurements.
(ii) Cross-contamination observed between the LA-AMS analysis of samples with different ^{14}C content is assumed to be caused by (1) re-ablation of displaced deposits from previously ablated samples and (2) gas exchange reactions of freshly produced CO_2 and CO_2 adsorbed to cell and capillary walls as well as deposits. These aspects can be addressed by (1) designing a cell with a larger ablation volume. Material that is deposited during ablation will less likely accumulate in the optical path of the laser beam and thus reduce cross contamination. Alternatively, deposits could be removed by compressed air fed to the ablation spot via an on-off valve and (2) heating of the LA-cell would allow to remove adsorbed CO_2 from the system.
(iv) LA-AMS is capable of providing a quasi-continuous stream of ^{14}C data, while the sample is being ablated. The existing data acquisition system is not designed to handle quasi-continuous data from the continuous scan mode. Here, a new design of data acquisition routines is necessary, which will allow to record a quasi-continuous data stream and to decide later (offline), which integration time is optimal in order to achieve the desired precision and spatial resolution. A deconvolution procedure has to be implemented that will allow to account for cross-talk.
So far the LA-AMS setup is optimized for samples with parallel growth layers. For corals, that grow in concentric layers and towards the edge of stalagmites the positioning of precision scans and single measurements becomes more difficult, which is especially pronounced toward the center of the specimen and for small samples. A square or circular laser spot and a scanning pattern along curved tracks could be implemented into the LA-AMS software, which will further improve the spatial resolution. User-friendliness of the software can be increased by integrating the laser control, employing a hand-scanner for mapping of the samples in the holder and selecting scan coordinates directly in the scanned image.

While significant room for future improvement has been identified, the novel LA-AMS setup is ready for use. Accurate and precise ^{14}C analysis of carbonate records can be performed at an exceptional sample throughput reaching unprecedented spatial resolution.

Appendices

Appendix A LA-AMS Software

The LA-system is equipped with a designated software combining the control of the pressure gauges, the x-y-positioning system as well as the read out of the camera and valve-switching of the gas handling system. The program is based on LabVIEW 2011 (National Instruments, Austin, Texas, USA). The front panel consists of a tab-control with four tabs. The first tab is shown in Figure A.1. On the right upper side a schematic overview of the capillaries for helium and vacuum are indicated (dark and light purple lines) and the position of the on-off valves are depicted (purple buttons). Furthermore, up to two pressure sensors can be read (white boxes), one directly mounted to the LA-cell, the other one, which has so far not been used, can be placed upstream of the four-way-valve. The cell is represented by the purple box and the sample holder by the inner rectangle. The position of the rectangle within the box indicates the position of the sample holder within the cell.

On the upper left side the image taken by the camera is shown. The camera read out is done by the National Instrument Vision Acquisition Software (VAS). Settings of the camera, i.e. gain or exposure time, can be changed in the "'National Instrument Measurement & Automation Explorer"'. The white area corresponds to the section of the sample visible to the camera through the cell head and the black triangle is a mark on the sample. Right under the camera-image the coordinates of the positioners are readout (Actual X, Actual Y) and the aimed positions are indicated (Aimed X, Aimed Y). The coordinates are given in μm. Furthermore, buttons for calibrating, referencing and homing of the positioners are implemented ("'Home"', "'Calibrate"', "'Reference X/Y"'). The positioners can be moved by either entering the coordinates ("'Go To (absolute)"') or by entering the x and y distance ("'Go To (relative)"'). The velocity is set in the "'Velocity"' field. In the middle of the front panel a field with an coordinate plane representing the sample holder is placed. By using the folder-button next to the plane, a scanned image of the sample holder can be loaded into the coordinate system. An orange point indicates the position of the laser on the sample and when the computer mouse is moved over the coordinate system the coordinates are readout and shown in the fields to the right ("'Cursor X"', "'Cursor Y"').

Furthermore, the positioners can be moved in a zig-zag sequence, which is especially useful for a scanning procedure. For this a table is found at the lower part of the tab

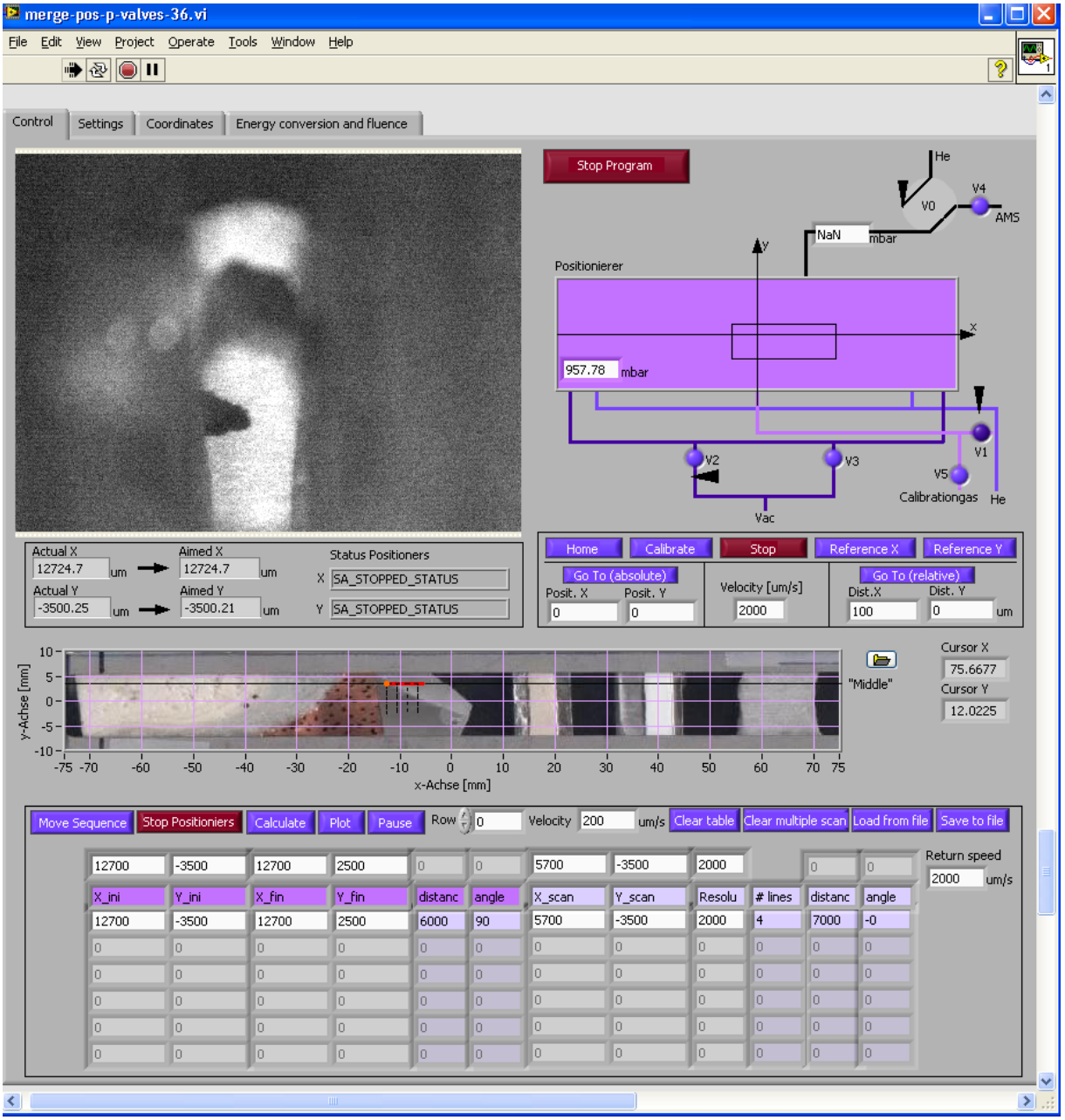

Figure A.1: Overview of the LabVIEW software control panel for LA-AMS measurements.

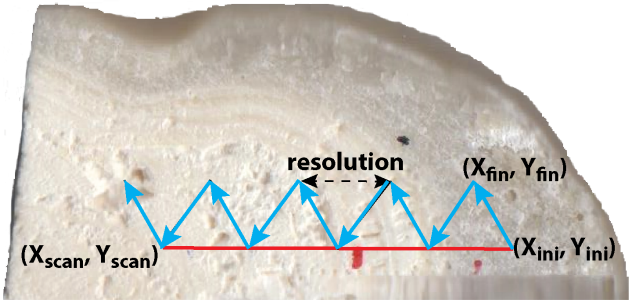

Figure A.2: Three coordinate pairs have to be selected for the precision scan. Furthermore, the resolution needs to be defined. The blue arrows indicate the scanning pattern.

control. There are three coordinate pairs: (X_{ini}, Y_{ini}), (X_{fin}, Y_{fin}) and (X_{scan}, Y_{scan}). Between "'ini"' and "'fin"' the first scan is performed as indicated in Figure A.2. The ini and scan coordinates define a line along which the next scans parallel to the blue line will be performed (red line). The "'resolution"' needs to be entered and defines the distance between two parallel scans and hence the amount of scans that will be performed. Coordinates can be written to the table either by typing them in the first line and then double clicking into the field they are supposed to be in, or by selecting the coordinate from the coordinate system above with a right click. Lines in the matrix can be added or deleted by right clicking on the table. Six scan-sequences can be performed subsequently. Once, all the coordinates are entered the "'calculate"' button will fill in the empty fields of the table, i.e. the distance, the angle and the number of lines. By pushing the button "'plot"' the scanning lines will be depicted in the coordinate system which is also shown in Figure A.1 (solid red and dashed black lines). The table can be saved to a text-file using the "'Save to file"' button. Furthermore, an external table with the coordinates can be loaded from a text-file by using the "'Load from file"' button. The button "'Clear table"' will clear the complete table, whereas "'Clear multiple scan"' will only clear the right half of the table. When the program is started, first an initialization of all hardware components is performed. All boolean buttons are set to false and values are assigned to the variables, e.g. the comport numbers of the pressure sensors and other hardware components. This is followed by an automatic calibration of the x- and y-positioner and referencing them. Furthermore, the readout of the pressure sensors and the camera is started.
Settings and parameters can be found on the second and third tab of the tab control. The

second tab "‘Settings"’ contains all the settings of the positioners on the left and of the pressure sensors on the right. Here the comport number, baud rate, address etc. of the hardware can be selected. For the positioners a tolerance range for the coordinates is defined and set to a default value of 5 μm. This tolerance is an abort criterion for loops to ensure further execution of further commands only, when the positioners have reached the aimed coordinates within the tolerance. Furthermore, information about the Diolan which controls the valves can be found and error messages of all devices can be found. In the third tab "‘coordinates"’ all inter-coordinates of the scan-sequence are listed. Options on the last tab "‘Energy conversion and fluence"’ allow to quickly calculate the fluence in dependence of the aperture which defines the spot size and the energy on the sample surface. During LA-AMS measurements, direct measurement of the laser energy at the spot of the sample is not possible. Therefore, a calibration between the energy measured after the second mirror of the setup and the energy on the sample has been set up. This conversion can also be performed on this tab.

The LA-AMS software can be stopped by the "‘stop program"’ button on the upper right which causes all loops to terminate and ensures a proper release of the hardware components.

References

Adkins J.F., Cheng H., Boyle E.A., Druffel E.R.M. and Edwards R.L. (**1998**). Deep-sea coral evidence for rapid change in ventilation of the deep North Atlantic 15,400 years ago. *Science*, 280(5364): 725–728.

Adkins J.F., Henderson G.M., Wang S.L., O'Shea S. and Mokadem F. (**2004**). Growth rates of the deep-sea scleractinia Desmophyllum cristagalli and Enallopsammia rostrata. *Earth and Planetary Science Letters*, 227(3-4): 481–490.

Alkass K., Buchholz B.A., Ohtani S., Yamamoto T., Druid H. and Spalding K.L. (**2010**). Age Estimation in Forensic Sciences APPLICATION OF COMBINED ASPARTIC ACID RACEMIZATION AND RADIOCARBON ANALYSIS. *Molecular & Cellular Proteomics*, 9(5): 1022–1030. 9th International Symposium on Mass Spectrometry in the Health and Life Sciences, San Francisco, CA, AUG 23-27, 2009.

Amoruso S., Sambri A. and Wang X. (**2006**). Propagation dynamics of a LaMnO3 laser ablation plume in an oxygen atmosphere. *Journal of Applied Physics*, 100: 013302–1 – 013302–11.

Anderson R. and Parrish J. (**1983**). Selective Photothemolysis - Precise Microsurgery by Selective Absorption of Pulsed Radiation. *Science*, 220(4596): 524–527.

Andrews A.H., Stone R.P., Lundstrom C.C. and DeVogelaere A.P. (**2009**). Growth rate and age determination of bamboo corals from the northeastern Pacific Ocean using refined Pb-210 dating. *Marine Ecology Progress Series*, 397: 173–185.

Arnold J.R. (**1954**). Scintillation counting of natural radiocarbon.1. The counting method. *Science*, 119(3083): 155–157.

Baker S. and Wilson C. (**2001**). Use of bomb radiocarbon to validate otolith section ages of red snapper Lutjanus campechanus from the northern Gulf of Mexico. *Limnology and Oceanography*, 46: 1819–1824.

Baldini J.U.L., McDermott F., Hoffmann D.L., Richards D.A. and Clipson N. (**2008**). Very high-frequency and seasonal cave atmosphere P-CO_2 variability: Implications for stalagmite growth and oxygen isotope-based paleoclimate records. *Earth and Planetary Science Letters*, 272(1-2): 118–129.

Bard E. (**1998**). Geochemical and geophysical implications of the radiocarbon calibration. *Geochimica et Cosmochimica Acta*, 62 (12): 2025–2038.

Bard E., Raisbeck G., Yiou F. and Jouzel J. (**2000**). Solar irradiance during the last 1200 years based on cosmogenic nuclides. *Tellus B: Chemical and Physical Meteorology.*, 52 (3): 985–992.

Basting D. and Marowsky G. (**2005**). *Excimer Laser Technology*, Springer-Verlag Berlin Heidelberg.

Beck J.W., Richards D.A., Edwards R.L., Silverman B.W., Smart P.L., Donahue D.J., Hererra-Osterheld S., Burr G.S., Calsoyas L., Jull A.J.T. and Biddulph D. (**2001**). Extremely large variations of atmospheric C-14 concentration during the last glacial period. *Science*, 292: 2453–2458.

Beer J., Muscheler R., Wagner G., Laj C., Kissel C., Kubik P.W. and Synal H.A. (**2002**). Cosmogenic nuclides during Isotope Stages 2 and 3. *Quaternary Science Reviews*, 21 (10): 1129–1139.

Bennett C.L., Beukens R.P., Clover M.R., Gove H.E., Liebert R.B., Litherland A.E., Purser K.H. and Sondheim W.E. (**1977**). Radiocarbon dating using electrostatic accelerators - netgative-ions provide key. *Science*, 198: 508–510.

Bleiner D., Belloni F., Doria D., Lorusso A. and Nassisi V. (**2005**). Overcoming pulse mixing and signal tailing in laser ablation inductively coupled plasma mass spectrometry depth profiling. *Journal of Analytical Atomic Spectrometry*, 20: 1337–1343.

Bleiner D. and Bogaerts A. (**2007**). Computer simulations of sample chambers for laser ablation-inductively coupled plasma spectrometry. *Spectrochimica Acta Part B: Atomic Spectroscopy*, 62(2): 155–168.

Bleiner D. and Günther D. (**2001**). Theoretical description and experimental observation of aerosol transport processes in laser ablation inductively coupled plasma mass spectrometry. *Journal of Analytical Atomic Spectrometry*, 16: 449–456.

Bonani G., Ivy S., Hajdas I., Niklaus T. and Suter M. (**1994**). AMS ^{14}C age determinations of tisue, bone and gras samples from the Ötztal Ice Man. *Radiocarbon*, 36: 247–250.

Brannon H.R., Taggart M.S. and Williams M. (**1955**). Proportional counting of carbon dioxide for radiocarbon dating. *Review of Scientific Instruments*, 26(3): 269–273.

Broecker W., Olson E. and Orr P. (**1960**). Radiocarbon Measurements and Annual Rings in Cave Formations. *Nature*, 185(4706): 93–94.

Broecker W., Tucek C. and Olson E. (**1959**). Radiocarbon analysis of oceanic CO_2. *International Journal for Applied Radiation and Isotopes*, 7(1): 1–10.

Bronk Ramsey C. and Hedges R. (**1997**). Hybrid ion sources: Radiocarbon measurements from microgram to milligram. *Nuclear Instruments & Methods in Physics Research Section B: Beam Interactions with Materials and Atoms*, 123: 539–545.

Buchholz B.A. and Spalding K.L. (**2010**). Year of birth determination using radiocarbon dating of dental enamel. *Surface and Interface Analysis*, 42: 398–401.

Bäuerle D. (**2000**). *Laser Processing and Chemistry*, Springer, Heidelberg.

Burke A., Robinson L.F., McNichol A.P., Jenkins W.J., Scanlon K.M. and Gerlach D.S. (**2010**). Reconnaissance dating A new radiocarbon method applied to assessing the temporal distribution of Southern Ocean deep-sea corals. *Deep Sea Research Part I: Oceanographic Research Papers*, 57: 1510–1520.

Butler P.G., Scourse J.D., Richardson C., Wanamaker Jr. A.D., Bryant C.L. and Bennell J.D. (**2009**). Continuous marine radiocarbon reservoir calibration and the C-13 Suess effect in the Irish Sea: Results from the first multi-centennial shell-based marine master chronology. *Earth and Planetary Science Letters*, 279: 230–241.

Butler P.G., Wanamaker Jr. A.D., Scourse J.D., Richardson C.A. and Reynolds D.J. (**2013**). Variability of marine climate on the North Icelandic Shelf in a 1357-year proxy archive based on growth increments in the bivalve Arctica islandica. *Palaeogeography Palaeoclimatology Palaeoecology*, 373: 141–151.

Cerling T. and Sharp Z. (**1996**). Stable carbon and oxygen isotope analysis of fossil tooth enamel using laser ablation. *Palaeogeography, Paleoclimatology Paleoecology*, 126: 173–186.

Chapman K. (**1972**). *Proceedings of the Symposium of North East Accelerator Personnel*, Tallahassee.

Chichkov B., Momma C., Nolte S., von Alvensleben F. and Tünnermann A. (**1996**). Femtosecond, picosecond and nanosecond laser ablation of solids. *Applied Physics A: Materials Science & Processing*, 63: 109–115.

Christl M., Vockenhuber C., Kubik P.W., Wacker L., Lachner J., Alfimov V. and Synal H.A. (**2013**). The ETH Zurich AMS facilities: Performance parameters and reference materials. *Nuclear Instruments & Methods in Physics Research Section B: Beam Interactions with Materials and Atoms*, 294: 29–38.

Craig H. (**1957**). Isotopic standards for carbon and oxygen and correction factors for massspectrometric analysis of carbon dioxide. *Geochimica et Cosmochimica Acta*, 12(1): 133.

Cristoforetti G., Legnaioli S., Palleschi V., Salvetti A. and Tognoni E. (**2004**). Influence of ambient gas pressure on laser-induced breakdown spectroscopy technique in the parallel double-pulse configuration. *Spectrochimica Acta B - Atomic Spectroscopy*, 59(12): 1907–1917.

Crutzen P. (**1997**). *Lectures in Chemistry 1991-1995*, chap. My life with O_3, NO_x and other YZO_ss, World Scientific Publishing Company, Singapore, 189–242.

Darke S., Long S., Pickford C. and Tyson J. (**1989**). Laser Ablation System for Solid Sample Analysis by Inductively Coupled Plasma Atomic Emission-Spectrometry. *Journal of Analytical Atomic Spectrometry*, 4(8): 715–719.

Demtröder W. (**2007**). *Laserspektroskopie Grundlagen und Techniken*, Springer, Berlin Heidelberg.

Dreybrodt W. (**1980**). Deposition of calcite from thin films of natural calcareous solutions and the growth of speleothems. *Chemical Geology*, 29(1): 89 – 105.

Dreyfus R. (**1991**). CU^0, CU^+, AND CU_2 from ecimer-ablated copper. *Journal of Applied Physics*, 69(3): 1721–1729.

Drosg R., Kutschera W., Scholz K., Steier P., Wagenbach D. and Wild E.M. (**2007**). Treatment of small samples of particulate organic carbon (POC) for radiocarbon dating of ice. *Nuclear Instruments & Methods in Physics Research Section B: Beam Interactions with Materials and Atoms*, 259(1): 340–344.

Druffel E.R., Griffin M., Beaupre S. and Dunbar R. (**2007**). Oceanic climate and circulation changes during the past four centuries from radiocarbon in corals. *Geophysical Research Letters*, 34: L09601.

Edwards R.L., Gallup C.D. and Cheng H. (**2003**). Uranium-series dating of marine and lacustrine carbonates. *Uranium-Series Geochemistry*, 52: 363–405.

Elmore D. and Phillips F. (**1987**). Accelerator Mass Spectrometry for measurement of long-lived radioisotopes. *Science*, 236(4801): 543–550.

Fahrni S., Wacker L., H.-A. S. and Szidat S. (**2013**). Improving a gas ion source for ^{14}C AMS. *Nuclear Instruments & Methods in Physics Research Section B: Beam Interactions with Materials and Atoms*, 294: 320–327.

Fairbanks R., Mortlock R., Chiu T., Cao L., Kaplan A., Guilderson T., Fairbanks T., Bloom A., Grootes P. and Nadeau M. (**2005**). Radiocarbon calibration curve spanning 0 to 50,000 years BP based on paired Th-230/U-234/U-238 and C-14 dates on pristine corals. *Quaternary Science Reviews*, 24(16-17): 1781–1796.

Fairchild I.J. and Treble P.C. (**2009**). Trace elements in speleothems as recorders of environmental change. *Quaternary Science Reviews*, 28: 449–468.

Farmer J.R., Hoenisch B., Robinson L.F. and Hill T.M. (**2015**). Effects of seawater-pH and biomineralization on the boron isotopic composition of deep-sea bamboo corals. *Geochimica et Cosmochimica Acta*, 155: 86–106.

Fergusson G.J. (**1955**). Radiocarbon dating system. *Nucleonics*, 13(1): 18–2323.

Finkel R. and Suter M. (**1993**). *AMS in the Earth Sciences*, Jai Press Inc.

Fleitmann D., Burns S.J., Mudelsee M., Neff U., Kramers J., Mangini A. and Matter A. (**2003**). Holocene forcing of the Indian monsoon recorded in a stalagmite from Southern Oman. *Science*, 300: 1737–1739.

Fohlmeister J., Kromer B. and Mangini A. (**2011**). The influence of soil organic matter age spectrum on the reconstruction of atmospheric C-14 levels via stalagmites. *Radiocarbon*, 53: 99–115.

Fohlmeister J., Schroeder-Ritzrau A., Scholz D., Spoetl C., Riechelmann D.F.C., Mudelsee M., Wackerbarth A., Gerdes A., Riechelmann S., Immenhauser A., Richter D.K. and Mangini A. (**2012**). Bunker Cave stalagmites: an archive for central European Holocene climate variability. *Climate of the Past*, 8(5): 1751–1764.

Fohlmeister J., Schroeder-Ritzrau A., Spoetl C., Frisia S., Miorandi R., Kromer B. and Mangini A. (**2010**). The influences of hydrology on the radiovenic and stable carbon isotope composition of cave drip water, Grotta die Ernesto (Italy). *Radiocarbon*, 52(4): 1529–1544.

Fohlmeister J., Vollweiler N., Spoetl C. and Mangini A. (**2013**). COMNISPA II: Update of a mid-European isotope climate record, 11 ka to present. *Holocene*, 23(5): 749–754.

Frank N., Paterne M., Ayliffe L., van Weering T., Henriet J.P. and Blamart D. (**2004**). Eastern North Atlantic deep-sea corals: tracing upper intermediate water Delta C-14 during the Holocene. *Earth Planet. Sci. Lett.*, 219(3-4): 297–309.

Freiwald A. (**2002**). *Reef-forming cold-water corals.* Ocean margin systems., Springer, Heidelberg.

Frick D.A. and Guenther D. (**2012**). Fundamental studies on the ablation behaviour of carbon in LA-ICP-MS with respect to the suitability as internal standard. *Journal of Analytical Atomic Spectrometry*, 27(8): 1294–1303.

Fricker M.B., Kutscher D.and Aeschlimann B., Frommer J., Dietiker R., Bettmer J. and Guenther D. (**2011**). High spatial resolution trace element analysis by LA-ICP-MS using a novel ablation cell for multiple or large samples. *International Journal of Mass Spectrometry*, 307: 39–45.

Friedrich W., Kromer B., Friedrich M., Heinemeier J., Pfeiffer T. and Talamo S. (**2006**). Santorini eruption radiocarbon dated to 1627 –1600 BC. *Science*, 312: 548.

Frisia S., Borsato A., Preto N. and McDermott F. (**2003**). Late Holocene annual growth in three Alpine stalagmites records the influence of solar activity and the North Atlantic Oscillation on winter climate. *Earth and Planetary Science Letters*, 216(3): 411–424.

Galli I., Bartalini S., Borri S., Cancio P., Mazzotti D., De Natale P. and Giusfredi G. (**2011**). Molecular Gas Sensing Below Parts Per Trillion: Radiocarbon-Dioxide Optical Detection. *Physical Review Letters*, 107(27): 270802.

Galtsoff P. (**1933**). Pearl and Hermes Reef. *Hawaii hydrological and biological observations*, 107: 49.

Gao P., Xu X., Zhou L., Pack M.A., Griffin S., Santos G.M., Southon J.R. and Liu K. (**2014**). Rapid sample preparation of dissolved inorganic carbon in natural waters using a headspace-extraction approach for radiocarbon analysis by accelerator mass spectrometry. *Limnology and Oceanography - Methods*, 12: 174–190.

Genty D., Baker A., Massault M., Proctor C., Gilmour M., Pons-Branchu E. and Hamelin B. (**2001**). Dead carbon in stalagmites: Carbonate bedrock paleodissolution vs. ageing of soil organic matter. Implications for 13C variations in speleotherms. *Geochimica et Cosmochimica Acta*, 65(20): 3443–3457.

Genty D., Blamart D., Ouahdi R., Gilmour M., Baker A., Jouzel J. and Van-Exter S. (**2003**). Precise dating of Dansgaard-Oeschger climate oscillations in western Europe from stalagmite data. *Nature*, 421(6925): 833–837.

Genty D. and Massault M. (**1999**). Carbon transfer dynamics from bomb-C-14 and delta C-13 time series of a laminated stalagmite from SW France - Modelling and comparison with other stalagmite records. *Geochimica et Cosmochimica Acta*, 63(10): 1537–1548.

Genty D., Vokal B., Obelic B. and Massault M. (**1998**). Bomb ^{14}C time history recorded in two modern stalagmites: importance for soil organic matter dynamics and bomb ^{14}C distribution over continents. *Earth and Planetary Science Letters*, 160: 795–809.

Günther D., Audetat A., Frischknecht R. and Heinrich C. (**1998**). Quantitative analysis of major, minor and trace elements in fluid inclusions using laser ablation inductively coupled plasma mass spectrometry. *Journal of Analytical Atomic Spectrometry*, 13(4): 263–270.

Günther D., Frischknecht R., Heinrich C. and Kahlert (**1997**). Capabilities of an argon fluoride 193 nm excimer laser for laser ablation inductively coupled mass spectrometry. *Journal of Analytical Atomic Spectrometry*, 12: 939–944.

Günther D. and Hattendorf B. (**2005**). Solid sample analysis using laser ablation inductively coupled plasma mass spectrometry. *Trac-Trends in Analytical Chemistry*, 24(3): 255–265.

Günther D. and Heinrich C. (**1999**). Comparison of the ablation behaviour of 266 nm Nd : YAG and 193 nm ArF excimer lasers for LA-ICP-MS analysis. *Journal of Analytical Atomic Spectrometry*, 14(9): 1369–1374.

Günther D., Horn I. and Hattendorf B. (**2000**). Recent trends and developments in laser ablation-ICP-mass spectrometry. *Fresenius' Journal of Analytical Chemistry.*, 368(1): 4–14.

Gonzalez J., Dundas S.H., Liu C.Y., Mao X. and Russo R.E. (**2006**). UV-femtosecond and nanosecond laser ablation-ICP-MS: internal and external repeatability. *Journal of Analytical Atomic Spectrometry*, 21(8): 778–784.

Gray A.L. (**1985**). Solid sample introduction by laser ablation for inductively coupled plasma source-mass spectrometry. *Analyst*, 110(5): 551–556.

Griffiths M., Fohlmeister J., Drysdale R., Hua Q., Johnson K., Hellstrom J., Gagan M. and x. Zhao J. (**2012**). Hydrological control of the dead carbon fraction in a Holocene tropical speleothem. *Quaternary Geochronology*, 14(0): 81 – 93.

Guillong M. and Günther D. (**2002**). Effect of particle size distribution on ICP-induced elemental fractionation in laser ablation-inductively coupled plasma-mass spectrometry. *Journal of Analytical Atomic Spectrometry*, 17(8): 831–837.

Guillong M., Kuhn H. and Günther D. (**2003**). Application of a particle separation device to reduce inductively coupled plasma-enhanced elemental fractionation in laser ablation-inductively coupled plasma-mass spectrometry. *Spectrochim. Acta B - Atom. Spectros.*, 58(2-3): 211–220.

Gurevich E.L. and Hergenroeder R. (**2007**). A simple laser ICP-MS ablation cell with wash-out time less than 100 ms. *Journal of Analytical Atomic Spectrometry*, 22(9): 1043–1050.

Hattendorf B. (**2002**). Ion Molecule Reactions for the Suppression of Spectral Interferences in Elemental Analysis by Inductively Coupled Plasma Mass Spectrometry. Ph.D. thesis, ETH Zurich.

Hattendorf B., Latkoczy C. and Günther D. (**2003**). Laser ablation-ICPMS. *Analytical Chemistry*, 75(15): 341A–347A.

Haught A. and Polk D. (**1970**). Formation and Heating of Laser Irradiated Solid Particle Plasmas. *Physics of Fluids*, 13(11): 2825.

Heinemeier J. and Andersen H.H. (**1983**). Production of C- directly from CO_2 using the ANIS sputter source. *Radiocarbon*, 25(2): 761–769.

Henderson G.M. (**2006**). Climate - Caving in to new chronologies. *Science*, 313(5787): 620–622.

Hendy C. (**1970**). *The Use of ^{14}C the study of cave processes*, Wiley interscience division, New York.

Hergenröder R., Samek O. and Hommes V. (**2006**). Femtosecond laser ablation elemental mass spectrometry. *Mass Spectrometry Reviews*, 25(4): 551–572.

Hirata T. and Miyazaki Z. (**2007**). High-speed camera imaging for laser ablation process: For further reliable elemental analysis using inductively coupled plasma-mass spectrometry. *Analytical Chemistry*, 79(1): 147–152.

Hodge E., McDonald J., Fischer M., Redwood D., Hua Q., Levchenko V., Drysdale R., Waring C. and Fink D. (**2011**). Using the C-14 bomb pulse to date young speleothems. *Radiocarbon*, 53(2): 345–357.

Holzkamper S., Spotl C. and Mangini A. (**2005**). High-precision constraints on timing of Alpine warm periods during the middle to late Pleistocene using speleothem growth periods. *Earth and Planetary Science Letters*, 236(3-4): 751–764.

Honig R.E. and Woolston J.R. (**1963**). Laser-induced emission of electrons, ions, and neutral atoms from solid surfaces. *Applied Physics Letters*, 2(7): 138–139.

Horn I. and Günther D. (**2003**). The influence of ablation carrier gasses Ar, He and Ne on the particle size distribution and transport efficiencies of laser ablation-induced aerosols: implications for LA-ICP-MS. *Applied Surface Science*, 207(1-4): 144–157.

Hua Q. and Barbetti M. (**2004**). Review of tropospheric bomb C-14 data for carbon cycle modeling and age calibration purposes. *Radiocarbon*, 46(3): 1273–1298.

Hua Q., McDonald J., Redwood D., Drysdale R., Lee S., Fallon S. and Hellstrom J. (**2012**). Robust chronological reconstruction for young speleothems using radiocarbon. *Quaternary Geochronology*, 14: 67–80.

Hughen K., Baillie M., Bard E., Beck J., Bertrand C., Blackwell P., Buck C., Burr G., Cutler K., Damon P., Edwards R., Fairbanks R., Friedrich M., Guilderson T., Kromer B., McCormac G., Manning S., Ramsey C., Reimer P., Reimer R., Remmele S., Southon J., Stuiver M., Talamo S., Taylor F., van der Plicht J. and Weyhenmeyer C. (**2004**). Marine04 marine radiocarbon age calibration, 0-26 cal kyr BP. *Radiocarbon*, 46(3): 1059–1086.

Hughes T. (**1975**). *Plasmas and Laser Light*, Adam Hilger Ltd., Bristol, UK.

Iida Y. (**1990**). Effects of Atmosphere on Laser Vaporization and Excitation Processes of Solid Samples. *Spectrochimica Acta B - Atomic Spectroscopy*, 45(12): 1353–1367.

Inam A., Hegde M., Wu X., Venkatesan T., England P., P.F. M., Chase E., Chang C., Tarascon J. and Wachtmann J. (**1988**). As-Desposited High-T_c and J_c superconducting thin-films made at low-temperatures. *Applied Physics Letters*, 53(10): 908–909.

Ishikawa J. (**2004**). *Negative ion sources*, chap. 14, Wiley-VCH, 285–310.

Jackson S. (**2001**). *The application of ND:YAG Lasers in LA-ICP-MS*, chap. 3, St John's, Newfoundland: Mineralogical Association of Canada, 29–45.

Jacob S. (**2001**). Beschleunigermassenspektrometrie (AMS) von ^{14}C bei tiefen Energien. Ph.D. thesis, ETH Zürich, Zurich, Switzerland.

Jaworski R., Hoffmann E. and Stephanowitz H. (**2002**). Collection and separation of particles by size from laser ablated material. *International Journal of Mass Spectrometry*, 219: 373–379.

Jeffries T., Jackson S. and Longerich H. (**1998**). Application of a frequency quintupled Nd : YAG source (lambda = 213 nm) for laser ablation inductively coupled plasma mass spectrometric analysis of minerals. *Journal of Analytical Atomic Spectrometry*, 13(9): 935–940.

Jenk T.M., Szidat S., Schwikowski M., Gaeggeler H.W., Wacker L., Synal H.A. and Saurer M. (**2007**). Microgram level radiocarbon ^{14}C determination on carbonaceous particles in ice. *Nuclear Instruments & Methods in Physics Research Section B: Beam Interactions with Materials and Atoms*, 259(1): 518–525.

Karas M., Bahr U. and Giessmann U. (**1991**). Matrix-Assisted Laser Desorption Ionization Mass-Spectrometry. *Mass Spectrometry Reviews*, 10(5): 335–357.

Karney G.B., Butler P., Speller S., Scourse J.D., Richardson C.A., Schroeder M., Hughes G.M., Czernuszka J.T. and Grovenor C.R.M. (**2012**). Characterizing the microstructure of Arctica islandica shells using NanoSIMS and EBSD. *Geochemistry Geophysics Geosystems*, 13.

Keenan E., Brainard R. and Basch L. (**2006**). Historical and present status of the pearl oyster, Pinctada margaritifera, at Pearl and Hermes Atoll, Northwestern Hawaiian Islands. *Atoll Research Bulletin*, 543: 333–344.

Keith M. and Weber J. (**1964**). Carbon and oxygen isotopic composition of selected limestones and fossils. *Geochimica et Cosmochimica Acta*, 28: 1787 – 1816.

Koch J., Feldmann I., Hattendorf B., Gunther D., Engel U., Jakubowski N., Bolshov M., Niemax K. and Hergenroder R. (**2002**). Trace element analysis of synthetic mono- and polycrystalline CaF2 by ultraviolet laser ablation inductively coupled plasma mass spectrometry at 266 and 193 nm. *Spectrochimica Acta B - Atomic Spectroscopy*, 57(6): 1057–1070.

Koch J. and Günther D. (**2011**). Review of the State-of-the-Art of Laser Ablation Inductively Coupled Plasma Mass Spectrometry. *Applied Spectroscopy*, 65(5): 155A–162A.

Koch J., von Bohlen A., Hergenroder R. and Niemax K. (**2004**). Particle size distributions and compositions of aerosols produced by near-IR femto- and nanosecond laser ablation of brass. *Journal of Analytical Atomic Spectrometry*, 19(2): 267–272.

Kovacs R., Nishiguchi K., Utani K. and Günther D. (**2010**). Development of direct atmospheric sampling for laser ablation-inductively coupled plasma-mass spectrometry. *Journal of Analytical Atomic Spectrometry*, 25(2): 142–147.

Kroslakova I. and Günther D. (**2007**). Elemental fractionation in laser ablation-inductively coupled plasma-mass spectrometry: evidence for mass load induced matrix effects in the ICP during ablation of a silicate glass. *Journal of Analytical Atomic Spectrometry*, 22(1): 51–62.

Kuhn H. and Günther D. (**2003**). Elemental fractionation studies in laser ablation inductively coupled plasma mass spectrometry on laser-induced brass aerosols. *Analytical Chemistry*, 75(4): 747–753.

Kutschera W. (**2005**). Progress in isotope analysis at ultra-trace level by AMS. *International Journal of Mass Spectrometry*, 242(2-3): 145–160.

Kutschera W. (**2013**). Applications of accelerator mass spectrometry. *International Journal of Mass Spectrometry*, 349(SI): 203–218.

Lachner J., Christl M., Vockenhuber C. and Synal H.A. (**2013**). Detection of UH3+ and ThH3+ molecules and U-236 background studies with low-energy AMS. *Nuclear Instruments & Methods in Physics Research Section B: Beam Interactions with Materials and Atoms*, 294: 364–368.

Lal D. and Peters B. (**1967**). *Cosmic ray produced radioactivity on the Earth*, Springer-Verlag, Berlin, 551–612.

Le Harzic R., Huot N., Audouard E., Jonin C., Laporte P., Valette S., Fraczkiewicz A. and Fortunier R. (**2002**). Comparison of heat-affected zones due to nanosecond and femtosecond laser pulses using transmission electronic microscopy. *Applied Physics Letters*, 80(21): 3886–3888.

Leach A. and Hieftje G. (**2002**). Factors affecting the production of fast transient signals in single shot laser ablation inductively coupled plasma mass spectrometry. *Applied Spectroscopy*, 56(1): 62–69.

Lee H., Galindo-Uribarri A., Chang K., Kilius L. and Litherland A. (**1984**). The $^{12}CH_2{}^{2+}$ molecule and radiocarbon dating by accelerator mass spectrometry. *Nuclear Instruments and Methods in Physics Research Section B: Beam Interactions with Materials and Atoms* , 5(2): 208 – 210.

Lerman J., Mook W. and Vogel W. (**1970**). *Radiocarbon variations and absolute chronology, 12th Nobel symposium*, chap. ^{14}C in tree rings from different localities, Almqvist & Wiksell-Gebers Forlag, Stockholm, 257–299.

Levin I. and Hesshaimer V. (**2000**). Radiocarbon - A unique tracer of global carbon cycle dynamics. *Radiocarbon*, 42(1): 69–80.

Libby W. (**1946**). Atmospheric Helium three and Radiocarbon from Cosmic Radiation. *Physical Review*, 69 (11): 671.

Libby W. (**1952**). *Radiocarbon Dating*, University of Chicago Press, Chicago.

Libby W. (**1955**). *Radiocarbon Dating*, Univ. Chicago Press, second edition edn.

Libby W., Anderson E. and Arnold J. (**1949**). Age Determination by Radiocarbon Content - World-Wide Assay of Natural Radiocarbon. *Science*, 109: 227–228.

Liu H., Borisov O., Mao X., Shuttleworth S. and Russo R. (**2000**). Pb/U fractionation during Nd : YAG 213 nm and 266 nm laser ablation sampling with inductively coupled plasma mass spectrometry. *Applied Spectroscopy*, 54(10): 1435–1442.

Liu X., Gao S., Yuan H., Hattendorf B., Günther D., Chen L. and Hu S. (**2002**). Analysis of 42 major and trace elements in glass standard reference materials by 193nm LA-ICPMS. *Acta Petrolei Sinica*, 18(3): 408–418.

Maiman I.H. (**1960**). Stimulated optical radiation in ruby. *Nature*, 187: 493 – 494.

Mangini A., Lomitschka M., Eichstadter R., Frank N., Vogler S., Bonani G., Hajdas I. and Patzold J. (**1998**). Coral provides way to age deep water. *Nature*, 392(6674): 347–348.

Mao S. (**2005**). Laser Ablation - Fundamentals and Applications, https://www.jlab.org/FEL/LPC/05lpc-mao.pdf (28.09.2015).

Mao X., Russo R., Liu H. and Ho J. (**1990**). As-Deposited Sb-Doped Bi-Pb-Sr-Ca-Cu-O Thin-Films Prepared by Pulsed Laser Deposition. *Applied Physics Letters*, 57(24): 2591–2593.

Masarik J. and Beer J. (**1999**). Simulation of particle fluxes and cosmogenic nuclide production in the Earth's atmosphere. *Journal of Geophysical Research: Atmospheres*, 104 (D10): 12099–12111.

Masarik J. and Beer J. (**2009**). An updated simulation of particle fluxes and cosmogenic nuclide production in the Earth's atmosphere. *Journal of Geophysical Research*, 114: D11103.

McDermott F. (**2004**). Palaeo-climate reconstruction from stable isotope variations in speleothems: a review. *Quaternary Science Reviews*, 23(7-8): 901–918.

McDermott F., Mattey D.P. and Hawkesworth C. (**2001**). Centennial-scale holocene climate variability revealed by a high-resolution speleothem delta O-18 record from SW Ireland. *Science*, 294(5545): 1328–1331.

McNichol A.P. and Aluwihare L.I. (**2007**). The power of radiocarbon in biogeochemical studies of the marine carbon cycle: Insights from studies of dissolved and particulate organic carbon (DOC and POC). *Chemical Reviews*, 107(2): 443–466.

Middleton R. (**1978**). Some remarks on negative ion sources and ^{14}C dating. In "First Conference on Radiocarbon Dating with Accelerators," .

Middleton R. (**1984**). A versatile high-intensity negative-ion source. *Nuclear Instruments & Methods in Physics Research Section B: Beam Interactions with Materials and Atoms*, 220(1): 105–106.

Miotello A. and Kelly R. (**1999**). Laser-induced phase explosion: new physical problems when a condensed phase approaches the thermodynamic critical temperature. *Applied Physics A: Materials Science & Processing*, 69(S): 67–73.

Miziolek A. (**2006**). *Laser-induced Breakdown Spectroscopy (LIBS) Fundamentals and Applications*, Cambridge University Press, Cambridge.

Moffitt R. (**1994**). Pearl oysters in Hawaii. *Hawaiian Shell News*, 42: 3–4.

Motelica-Heino M., Le Coustumer P. and Donard O. (**2001**). Micro- and macro-scale investigation of fractionation and matrix effects in LA-ICP-MS at 1064 nm and 266 nm on glassy materials. *Journal of Analytical Atomic Spectrometry*, 16(6): 542–550.

Mueller A., Doebeli M., Seiler M. and H.A. S. (**2015**). A simple Bragg detector design for AMS and IBA applications. *Nuclear Instruments & Methods in Physics Research Section B: Beam Interactions with Materials and Atoms*, 356: 81–87.

Mueller A.M., Christl M., Doebeli M., Kubik P.W., Suter M. and Synal H.A. (**2008**). (10)Be AMS measurements at low energies (E $<$ 1 MeV). *Nuclear Instruments & Methods in Physics Research Section B: Beam Interactions with Materials and Atoms*, 266(10): 2207–2212.

Muller R.A. (**1977**). Radioisotope dating with a cyclotron. *Science*, 196(4289): 489–494.

Nelson D.E., Korteling R.G. and Stott W.R. (**1977**). C-14 - direct detection at natural concentrations. *Science*, 198(4316): 507–508.

Nishiguchi K., Utani K. and Fujimori E. (**2008**). Real-time multielement monitoring of airborne particulate matter using ICP-MS instrument equipped with gas converter apparatus. *Journal of Analytical Atomic Spectrometry*, 23(8): 1125–1129.

Noe S.U. and Dullo W.C. (**2006**). Skeletal morphogenesis and growth mode of modern and fossil deep-water isidid gorgonians (Octocorallia) in the West Pacific (New Zealand and Sea of Okhotsk). *Coral Reefs*, 25(3): 303–320.

Oeschger H. (**1963**). *Low level counting methods*, chap. 13, IAEA, Vienna.

Oeschger H., Siegenthaler U., Schotterer U. and Gugelmann A. (**1975**). Box diffusion-model to study carbon-dioxide exchange in nature. *Tellus*, 27(2): 168–192.

Ognibene T., Thomas A., Daley P., Bench G. and Turteltaub K. (**2015**). An interface for the direct coupling of small liquid samples to AMS. *Nuclear Instruments & Methods in Physics Research Section B: Beam Interactions with Materials and Atoms*, In Press.

Olsson I. (**1957**). A C14 dating station using the CO_2 proportional counting method. *Arkiv för Fysik*, 13(1): 37–60.

Olsson I. (**1968**). Modern aspects of radiocarbon datings. *Earth-Science Reviews*, 4(3): 203–218.

Pandow M., Mackay C. and Wolfgang R. (**1960**). The reaction of atomic carbon with oxygen: significance for the natural radio-carbon cycle. *Journal of Inorganic and Nuclear Chemistry*, 14: 153 – 158.

Perron N., Szidat S., Fahrni S., Ruff M., Wacker L., Prevot A.S.H. and Baltensperger U. (**2010**). Towards on-line C-14 analysis of carbonaceous aerosol fractions. *Radiocarbon*, 52(2): 761–768.

Phipps C. and Dreyfus R. (**1993**). *Laser Ionization Mass Analysis in: Chemical Analysis Series Vol. 124*, Wiley, New York, 369–431.

Pisonero J., Fliegel D. and Guenther D. (**2006**a). High efficiency aerosol dispersion cell for laser ablation-ICP-MS. *Journal of Analytical Atomic Spectrometry*, 21(9): 922–931.

Pisonero J., Fliegel D. and Guenther D. (**2006**b). High efficiency aerosol dispersion cell for laser ablation-ICP-MS. *Journal of Analytical Atomic Spectrometry*, 21(9): 922–931.

Plotnikov A., Vogt C. and Wetzig K. (**2002**). An approach to the reconstruction of true concentration profile from transient signal in spatially resolved analysis by means of laser ablation ICP MS. *Journal of Analytical Atomic Spectrometry*, 17: 1114–1120.

Poitrasson F., Mao X., Mao S., Freydier R. and Russo R. (**2003**). Comparison of ultraviolet femtosecond and nanosecond laser ablation inductively coupled plasma mass spectrometry analysis in glass, monazite, and zircon. *Analytical Chemistry*, 75(22): 6184–6190.

Povinec P.P., Litherland A.E. and von Reden K.F. (**2009**). Developments in radiocarbon technologies: from the Libby counter to compound-specific AMS analysis. *Radiocarbon*, 51(1): 45–78.

Puell H. (**1970**). Heating of Laser Produced Plasmas Generated at Plane Solid Targets. *Zeitung für Naturforschung*, 25 a(12): 1807–1815.

Purser K.H., Liebert R.B., Litherland A.E., Beukens R.P., Gove H.E., Bennett C.L., Clover M.R. and Sondheim W.E. (**1977**). Attempt to detect stable N-ions from a sputter ion-source and some implications of results for design of tandems for ultra-sensitive carbon analysis. *Revue de Physique Appliquée*, 12(10): 1487–1492.

Raisbeck G., Yiou F., Bourles D., Lestringuez J. and Deboffle D. (**1984**). Measurement of ^{10}Be with a Tandetron accelerator operating at 2 MV. *Nuclear Instruments & Methods in Physics Research Section B: Beam Interactions with Materials and Atoms*, 233: 175–178.

Raisbeck G., Yiou F., Klein J. and Middelton R. (**1983**). Accelerator Mass-Spectrometry measurement of cosmogenic AL-26 in terrestrial and extraterrestrial matter. *Nature*, 301(5902): 690–692.

Reimer P., Baillie M., Bard E., Bayliss A., Beck W., Bertrand C., Blackwell P., Buck C., Burr G., Cutler K., Damon P., Edwards R., Fairbanks R., Friedrich M., Guilderson T., Hogg A., Hughen K., Kromer B., McCormac G., Manning S., Ramsey C., Reimer R., Remmele S., Southon J., Stuiver M., Talamo S., Taylor F., van der Plicht J. and Weyhenmeyer C. (**2004**). IntCal04 terrestrial radiocarbon age calibration, 0–26 cal kyr BP. *Radiocarbon*, 46: 1029–1058.

Reimer P.J., Baillie M.G.L., Bard E., Bayliss A., Beck J.W., Blackwell P.G., Ramsey C.B., Buck C.E., Burr G.S., Edwards R.L., Friedrich M., Grootes P.M., Guilderson T.P., Hajdas I., Heaton T.J., Hogg A.G., Hughen K.A., Kaiser K.F., Kromer B., McCormac F.G., Manning S.W., Reimer R.W., Richards D.A., Southon J.R., Talamo S., Turney C.S.M., van der Plicht J. and Weyhenmeye C.E. (**2009**). IntCal09 and marine09 radiocarbon age calibration curves 0-50,000 years cal BP. *Radiocarbon*, 51(4): 1111–1150.

Reimer P.J., Bard E., Bayliss A., Beck J.W., Blackwell P.G., Ramsey C.B., Buck C.E., Cheng H., Edwards R.L., Friedrich M., Grootes P.M., Guilderson T.P., Haflidason H., Hajdas I., Hatte C., Heaton T.J., Hoffmann D.L., Hogg A.G., Hughen K.A., Kaiser K.F., Kromer B., Manning S.W., Niu M., Reimer R.W., Richards D.A., Scott E.M., Southon J.R., Staff R.A., Turney C.S.M. and van der Plicht J. (**2013**). IntCal13 and marine13 radiocarbon age calibration curves 0-50,000 years cal BP. *Radiocarbon*, 55(4, SI): 1869–1887.

Rethfeld B., Sokolowski-Tinten K., von der Linde D. and Anisimov S. (**2004**). Timescales in the response of materials to femtosecond laser excitation. *Applied Physics A: Materials Science & Processing*, 79(4-6): 767–769.

Reynolds G.T., Harrison F.B. and Salvini G. (**1950**). Liquid scintillation counters. *Physical Review*, 78(4): 488.

Richards D.A. and Dorale J.A. (**2003**). Uranium-series chronology and environmental applications of speleothems. *Reviews in Mineralogy and Geochemistry*, 52: 407–460.

Richter D., Markewitz D., Trumbore S. and Wells C. (**1999**). Rapid accumulation and turnover of soil carbon in a re-establishing forest. *Nature*, 400(6739): 56–58.

Roark E.B., Guilderson T.P., Dunbar R.B., Fallon S.J. and Mucciarone D.A. (**2009**). Extreme longevity in proteinaceous deep-sea corals. *Proceedings of the National Academy of Sciences of the United States of America*, 106(13): 5204–5208.

Robinson L.F., Adkins J., Keigwin L., Southon J., Fernandez D., Wang S. and Scheirer D. (**2005**). Radiocarbon variability in the western North Atlantic during the last deglaciation. *Science*, 310(5753): 1469–1473.

Rosenheim B.E., Thorrold S.R. and Roberts M.L. (**2008**). Accelerator mass spectrometry C-14 determination in CO_2 produced from laser decomposition of aragonite. *Rapid Communications in Mass Spectrometry*, 22(21): 3443–3449.

Rozanski K., Stichler W., Gonfiantini R., Scott E., Beukens R., Kromer B. and van der Plicht J. (**1992**). The IAEA ^{14}C intercomparison exercise 1990. *Radiocarbon*, 34: 506–519.

Rudzka-Phillips D., McDermott F., Jackson A. and Fleitmann D. (**2013**). Inverse modelling of the C-14 bomb pulse in stalagmites to constrain the dynamics of soil carbon cycling at selected European cave sites. *Geochimica et Cosmochimica Acta*, 112: 32–51.

Ruff M. (**2008**). Radiocarbon Measurement of Micro-Scale Samples - A carbon dioxide inlet system for AMS. Ph.D. thesis, Philosophisch-naturwissenschaftliche Fakultät der Universität Bern.

Ruff M., Fahrni S., Gaeggeler H.W., Hajdas I., Suter M., Synal H.A., Szidat S. and Wacker L. (**2010**a). On-line radiocarbon measurements of small samples using elemental analyzer and MICADAS gas ion source. *Radiocarbon*, 52(4): 1645–1656.

Ruff M., Szidat S., Gaeggeler H.W., Suter M., Synal H.A. and Wacker L. (**2010**b). Gaseous radiocarbon measurements of small samples. *Nucl. Instr. and Meth. B*, 268(7-8): 790–794.

Ruff M., Wacker L., Gaeggeler H.W., Suter M., Synal H.A. and Szidat S. (**2007**). A gas ion source for radiocarbon measurements at 200 kV. *Radiocarbon*, 49(2): 307–314.

Russo R., Mao X., Gonzalez J.J. and Yoo J. (**2013**). Femtosecond versus Nanosecond Laser Pulse Duration for Laser Ablation Chemical Analysis. *Spectroscopy*, 28: 24.

Russo R., Mao X., Liu C. and Gonzalez J. (**2004**). Laser assisted plasma spectrochemistry: laser ablation. *Journal of Analytical Atomic Spectrometry*, 19(9): 1084–1089.

Russo R., Mao X., Liu H., Gonzalez J. and Mao S. (**2002**). Laser ablation in analytical chemistry - a review. *Talanta*, 57(3): 425–451.

Santos G.M., Southon J.R., Griffin S., Beaupre S.R. and Druffel E.R.M. (**2007**). Ultra small-mass AMS C-14 sample preparation and analyses at KCCAMS/UCI Facility. *Nuclear Instruments & Methods in Physics Research Section B: Beam Interactions with Materials and Atoms*, 259(1): 293–302.

Schleicher M., Grootes P.M., Nadeau M.J. and Schoon A. (**1998**). The carbonate C-14 background and its components at the Leibniz AMS facility. *Radiocarbon*, 40(1): 85–93.

Scholz D. and Hoffmann D. (**2008**). 230Th/U-dating of fossil reef corals and speleothems. *Quaternary Science Journal*, 57(1-2): 52–76.

Schou J., Amoruso S. and Lunney J. (**2007**). *Laser Ablation and Its Applications, Springer Series in Optical Sciences*, chap. Chapter 4: Plume Dynamics, Springer, New York, 69–98.

Schröder-Ritzrau A., Mangini A. and Lomitschka M. (**2003**). Deep-sea corals evidence periodic reduced ventilation in the North Atlantic during the LGM/Holocene transition. *Earth and Planetary Science Letters*, 216(3): 399–410.

Schulze-König T., Dueker S.R., Giacomo J., Suter M., Vogel J.S. and Synal H.A. (**2010**a). BioMICADAS: Compact next generation AMS system for pharmaceutical science. *Nuclear Instruments & Methods in Physics Research Section B: Beam Interactions with Materials and Atoms*, 268(7-8): 891–894.

Schulze-König T., Wacker L. and H.-A. S. (**2010**b). Direct radiocarbon analysis of exhaled air. *Journal of Analytical Atomic Spectrometry*, 26: 287–292.

Sharp Z. (**1992**). In-Situ Laser Microprobe Techniques for Stable Isotope Analysis. *Chemical Geology*, 101(1-2): 3–19.

Silfvast W. (**1995**). *Lasers*, chap. 11, McGraw-Hill, New York, 11.1–11.39.

Southon J. and Santos G.M. (**2007**). Life with MC-SNICS. Part II: Further ion source development at the Keck carbon cycle AMS facility. *Nuclear Instruments & Methods in Physics Research Section B: Beam Interactions with Materials and Atoms*, 259(1): 88–93.

Spötl C. and Mattey D. (**2006**). Stable isotope microsampling of speleothems for palaeoenvironmental studies: A comparison of microdrill, micromill and laser ablation techniques. *Chemical Geology*, 235(1-2): 48–58.

Steier P., Golser R., Kutschera W., Priller A., Vockenhuber C. and Winkler S. (**2004**). VERA, an AMS facility for "all" isotopes. *Nuclear Instruments & Methods in Physics Research Section B: Beam Interactions with Materials and Atoms*, 223: 67–71.

Stocker M., Döbeli M., Grajcar M., Suter M., H.-A. S. and Wacker L. (**2005**). A universal and competitive compact AMS facility. *Nuclear Instruments & Methods in Physics Research Section B: Beam Interactions with Materials and Atoms*, 240: 483–489.

Stuiver M. (**1983**). International agreements and the use of the new oxalic-acid standard. *Radiocarbon*, 25(2): 793–795.

Stuiver M. and Polach H.A. (**1977**). Reporting of C-14 data - discussion. *Radiocarbon*, 19(3): 355–363.

Stuiver M. and Robinson S.W. (**1974**). University of Washington Geosecs North Atlantic carbon-14 results. *Earth and Planetary Science Letters*, 23: 87–90.

Suess H.E. (**1965**). Secular variations of cosmic-ray-produced carbon 14 in atmosphere and their interpretations. *Journal of Geophysical Research*, 70(23): 5937.

Sundqvist H.S., Holmgren K., Fohlmeister J., Zhang Q., Bar Matthews M., Spotl C. and Kornich H. (**2013**). Evidence of a large cooling between 1690 and 1740 AD in southern Africa. *Scientific Reports*, 3: 1767.

Suter M., Dobeli M., Grajcar M., Muller A., Stocker M., Sun G., Synal H.A. and Wacker L. (**2007**). Advances in particle identification in AMS at low energies. *Nuclear Instruments & Methods in Physics Research Section B: Beam Interactions with Materials and Atoms*, 259(1): 165–172.

Suter M., Jacob S. and Synal H.A. (**1997**). AMS of C-14 at low energies. *Nucl. Instr. and Meth. B*, 123(1-4): 148–152.

Synal H.A., Döbeli M., Jacob S., Stocker M. and Suter M. (**2004**). Radiocarbon AMS towards its low-energy limits. *Nuclear Instruments & Methods in Physics Research Section B: Beam Interactions with Materials and Atoms*, 223-224(0): 339–345.

Synal H.A., Schulze-König T., Seiler M., Suter M. and Wacker L. (**2013**). Mass spectrometric detection of radiocarbon for dating applications. *Nucl. Instr. and Meth. B*, 294: 349–352.

Synal H.A., Stocker M. and Suter M. (**2007**). MICADAS: A new compact radiocarbon AMS system. *Nucl. Instr. and Meth. B*, 259: 7–13.

Synal H.A. and Wacker L. (**2010**). AMS measurement technique after 30 years: Possibilities and limitations of low energy systems. *Nuclear Instruments and Methods in Physics Research Section B: Beam Interactions with Materials and Atoms*, 268: 701 – 707.

Tanner M. and Günther D. (**2006**). In torch laser ablation sampling for inductively coupled plasma time of flight mass spectrometry. *Journal of Analytical Atomic Spectrometry*, 21(9): 941–947.

Tans P., de Jong A., Mook W. and Hut G. (**1982**). High accuracy carbon-14 counting and the application to the radiocarbon calibration curve. . In **P. Povinec**, ed., "2nd International Conference on Low-Level Counting," vol. Volume 1, Veda Publishers.

Thompson M., Goulter J. and Sieper F. (**1981**). Laser Ablation for the Introduction of Solid Samples into an Inductively Coupled Plasma for Atomic-Emission Spectrometry. *Analyst*, 106(1258): 32–39.

Trumbore S. (**2009**). Radiocarbon and Soil Carbon Dynamics. *Annual Review of Earth and Planetary Sciences*, 37: 47–66.

Uhl T., Kretschmer W., Luppold W. and Scharf A. (**2004**). Direct coupling of an elemental analyzer and a hybrid ion source for AMS measurements. *Radiocarbon*, 46(1): 65–75.

Usoskin I.G., Horiuchi K., Solanki S., Kovaltsov G.A. and Bard E. (**2009**). On the common solar signal in different cosmogenic isotope data sets. *Journal of Geophysical Research*, 114: A03112.

Vaks A., Gutareva O.S., Breitenbach S.F.M., Avirmed E., Mason A.J., Thomas A.L., Osinzev A.V., Kononov A.M. and Henderson G.M. (**2013**). Speleothems Reveal 500,000-Year History of Siberian Permafrost. *Science*, 340(6129): 183–186.

Van Malderen S.J.M., van Elteren J.T. and Vanhaecke F. (**2015**). Development of a fast laser ablation-inductively coupled plasma-mass spectrometry cell for sub-μm scanning of layered materials. *Journal of Analytical Atomic Spectrometry*, 30: 119–125.

Vockenhuber C., Ahmad I., Golser R., Kutschera W., Liechtenstein V., Priller A., Steier P. and Winkler S. (**2003**). Accelerator mass spectrometry of heavy long-lived radionuclides. *International Journal of Mass Spectrometry*, 223(1-3): 713–732.

Vollweiler N. (**2010**). COMNISPA - ein präzise datiertes Klima-Archiv aus holozänen alpinen Stalagmiten. Ph.D. thesis, Ruprech-Karls-Universität Heidelberg.

Vollweiler N., Scholz D., Muehlinghaus C., Mangini A. and Spoetl C. (**2006**). A precisely dated climate record for the last 9 kyr from three high alpine stalagmites, Spannagel Cave, Austria. *Geophysical Research Letters*, 33(20): L20703.

von Bergmann H., Rebhan U. and Stamm U. (**2005**). *Excimer Laser Technology*, chap. Design and technology of excimer lasers (Chap. 4), Springer, Berlin, Heidelberg.

Wacker L., Bonani G., Friedrich M., Hajdas I., Kromer B., Nemec M., Ruff' M., Suter M., Synal H.A. and Vockenhuber C. (**2010**). MICADAS: Routine and high-precision radiocarbon dating. *Radiocarbon*, 52(2, 1): 252–262.

Wacker L., Münsterer C., Hattendorf B., Christl M., Günther D. and Synal H.A. (**2013**). Direct coupling of a laser ablation cell to an AMS. *Nuclear Instruments & Methods in Physics Research Section B: Beam Interactions with Materials and Atoms*, 294: 287 – 290.

Wacker L., Nemec M. and Bourquin J. (**2010**). A revolutionary graphitisation system: Fully automated, compact and simple. *Nuclear Instruments & Methods in Physics Research Section B: Beam Interactions with Materials and Atoms*, 268(7-8): 931–934.

Wang H.A.O., Grolimund D., Giesen C., Borca C.N., Shaw-Stewart J.R.H., Bodenmiller B. and Guenther D. (**2013**). Fast Chemical Imaging at High Spatial Resolution by Laser Ablation Inductively Coupled Plasma Mass Spectrometry. *Analyitcal Chemistry*, 85(21): 10107–10116.

Wang Z., Hattendorf B. and Günther D. (**2006**). Analyte response in laser ablation inductively coupled plasma mass spectrometry. *Journal of the American Society for Mass Spectrometry*, 17(5): 641–651.

Watling L., France S., Pante E. and Simpson A. (**2011**). Chapter Two - Biology of Deep-Water Octocorals. In **M. Lesser**, ed., "Advances in Marine Biology," vol. 60 of *Advances in Marine Biology*, Academic Press, 41 – 122.

Welte C., Wacker L., Hattendorf B., M. C., Koch J., H.-A. S. and Günther D. (**submitted**). Novel Laser Ablation Sampling Device for the Rapid Radiocarbon Analysis of Carbonate Samples by Accelerator Mass Sepctrometry. Submitted to Radiocarbon.

Wigley T.M.L. (**1975**). C-14 Dating of groundwater from closed and open systems. *Water Resources Research*, 11(2): 324–328.

Witanachchi S., Patel S., Shaw D. and Kwok H. (**1989**). Effect of Buffer Layers on Low-Temperature Growth of Mirror-Like Superconducting Thin-Films on Sapphire. *Applied Physics Letters*, 55(3): 295–297.

Witbaard R., Duineveld G. and Wilde P.d. (**1999**). Geographical differences in grwoth rates of Arctica islandica (Mollusca: Bivalvia) from the North Sea and adjacent waters. *Journal of the Marine Biological Association of the United Kingdom*, 79: 907–915.

Witbaard R., Franken R. and Visser B. (**1997**). Growth of juvenile Arctica islandica under experimental conditions. *Helgoländer Meerersuntersuchungen*, 51: 417–431.

Zoppi U., Skopec Z., Skopec J., Jones G., Fink D., Hua Q., Jacobsen G., Tuniz C. and Williams A. (**2004**). Forensic applications of C-14 bomb-pulse dating. *Nuclear Instruments & Methods in Physics Research Section B: Beam Interactions with Materials and Atoms*, 223: 770–775.

Danke

Ein grosses Dankeschön geht an Hans-Arno Synal und Detlef Günther für die Möglichkeit, dieses spannende Projekt im Labor für Ionenstrahlphysik und im Labor für anorganische Chemie durchführen zu dürfen. Die Teilnahme an (inter-)nationalen Konferenzen wurde immer grosszügig bewilligt und beide Gruppen sind mir nach der Geburt meiner Tochter sehr entgegen gekommen. Ich möchte auch der ETH für die Finanzierung unseres 'High-Risk Projects' danken. Danke an Werner Aeschbach, der das Korreferat übernommen und diese Arbeit begutachtet hat.
Meinen Betreuern Lukas Wacker und Bodo Hattendorf möchte ich ein riesiges Dankeschön aussprechen - für die Unterstützung im Labor, beim Schreiben und überhaupt! In den letzten vier Jahren habe ich wirklich sehr viel gelernt (z.B. wie man Schrauben aus der Ionenquelle mit Staubsaugern holt). Vielen Dank an Marcus Christl - ohne den ich wohl nie im LIP gelandet wäre - für die hilfreichen Diskussionen, die guten Ideen, das Gegenlesen von so manchem Schriftstück und das Schwelgen in Erinnerungen an Heidelberger Zeiten. Während der Mittagessen mit euch dreien, in der Woka sind die besten Ideen entstanden.
Ein wesentlicher Teil dieser Arbeit fand in der Werkstatt statt. Ich bedanke mich für die technische Unterstützung, vor allem durch Philippe Trüssel, der alle noch so umständlichen Ideen in anfassbare Gegenstände verwandelt hat. Danke auch an Pascal Amrein, Heinz Benz, René Gruber, Andreas Herrmann, Thomas Mettler und Balaram Ramaligam für das Löten, Leimen, Fräsen und Sägen.
Allen H. Andrews, Sebastian Breitenbach, Jesse Farmer, Jens Fohlmeister, André Freiwald und Laura Robinson haben mir exzellentes Probenmaterial zum ausprobieren unseres neuen Aufbaus zur Verfügung gestellt. Vielen Dank für die gute Zusammenarbeit!

Conny Aurelio, Nicole Bachmann, Judith Eberle und Leo Noll sei gedankt, dass sie immer ein offenes Ohr für jegliche Probleme administrativer Art hatten und in dieser Hinsicht ein Rundum-Sorglos-Paket geboten haben.
An meinen leidensgenossen Christian Wirsig richte ich ein besonderes Dankeschön - die mühsame Schreibzeit wäre viel schlimmer ohne Dich gewesen! Danke an Steffen Allner, Núria Casacuberta, Max Döbeli, Simon Fahrni, Matthias George, Joachim Koch, Sascha Maxeiner, Cameron McIntyre, Noldi Müller und Hao Wang für die vielen guten Ideen und das Korrekturlesen der Arbeit. Überhaupt möchte ich den Kolleginnen und Kollegen des LIP - Georges Bonani, Joel Bourquin, Simon Bühlmann, Peter Eberhart, Boris Fehst,

Dominik Güttler, Irka Hajdas, Kristina Hippe, Susan Ivy-Ochs, Peter Kubik, Johannes Lachner, Mantana Maurer, Rudolf Pfenninger, Maria Roldan, Simon Roost, Anita Schlatter, Martina Schulte-Borchers, Martin Seiler, Marius Simon, Adam Sookdeo, Martin Suter, Christof Vockenhuber, sowie den Gäste Giulia Guidobaldi und Stefano Casale - für spannende Diskussionen, Kuchenwettbewerbe, gemeinsame Mittagessen gefolgt von Kafi im Kontrollraum, Töggeli-Sessions, Sola-Teilnahmen und so manches Bier im Bistro danken. Das regelmässige Joggen und die Mittagessen mit Steffen Allner, Nataliya Fedotova, Sabrina Gschwind und Kathrin Lange waren eine willkommene Abwechslung zum Laboralltag. Auch bei Beni Aeschlimann, Olga Borovinskaya, Robert Brogioli, Marcel Burger, Rolf Dietiker, Ladina Dorta, Tatiana Egorova, Luca Flamigni, Daniel Frick, Giovanni Giallongo, Reto Glaus, Alexander Gundlach-Graham, Kevin Guex, Kathrin Hametner, Debora Käser, Giovanni Lotito, Thomas Nauser, Masaki Ohata, Abi Saurab, Gunnar Schwarz, Daniel Tabersky, Mohamed Tarik, Peter Velicsanyi, Melinda Vontobel und Ceren Yilmaz bedanke ich für die Zusammenarbeit während meiner Zeit in der Chemie.
Johanna - Danke für deine Hilfe beim Gestalten des Covers! Das Foto auf dem Cover wurde von Silviu Constantin zur Verfügung gestellt.

Zuletzt danke an meine Freunde und meine Familie: die SängerInnen vom Contrapunto haben mich herzliche aufgenommen und ich habe das gemeinsame Singen und die Konzerte sehr genossen. Heidi, Marta und Otto danke ich für die Geduld, die sie mit mir beim Jassen hatten; die Doppelkopfabende mit Maren und Chris sind unvergesslich. Abi & Mahayla, Andrés, Bettina, Johanna, Nora, Sabine - danke für die schönen Unternehmungen in und um Zürich. Mit Ingrid, Martina und Susanne konnte ich neue Kraft in den Finnlandurläuben tanken. Danke an Annika, Corinna, Jochen, Juli, Katja und Madeline für die wunderbaren und erholsamen Treffen in Ravensburg. Anabelle, Carmen, Marion, Sandra, meine Ettaler Oma, Elinor und die Vronis haben mich bei vielen Telefonaten und Besuchen aufgemuntert und zum Lachen gebracht. Mein Vater Paul hat immer an mich geglaubt. Und dann sind da noch Charlotte und Daniel: Danke!